UNIVERSITY OF OKLAHOMA

GRADUATE COLLEGE

MODELING AND CONTROL OF PCM-BASED THERMAL ENERGY STORAGE INTEGRATED IN AIR DISTRIBUTION SYSTEMS

A DISSERTATION

SUBMITTED TO THE GRADUATE FACULTY

in partial fulfillment of the requirements for the

Degree of

DOCTOR OF PHILOSOPHY

By

PHILANI GIFT HLANZE
Norman, Oklahoma
2025

Downloaded from SHAREOK. Persistent Handle URL: https://hdl.handle.net/11244/341793

MODELING AND CONTROL OF PCM-BASED THERMAL ENERGY STORAGE INTEGRATED IN AIR DISTRIBUTION SYSTEMS

A DISSERTATION APPROVED FOR THE

SCHOOL OF AEROSPACE AND MECHANICAL ENGINEERING

BY THE COMMITTEE CONSISTING OF

Dr. Li Song, Chair

Dr. Jie Cai, Co-Chair

Dr. Hamidreza Shabgard

Dr. Wilson Merchán-Merchán

Dr. Choon Yik Tang

©Copyright by PHILANI GIFT HLANZE 2025
All Rights Reserved.

Acknowledgements

I would like to thank my advisor, Dr. Jie Cai, who accepted me into his research group as an undergraduate student and mentored me through my Master's and PhD degree programs. Your patience, support and encouragement have been vital to my academic journey and personal growth. I will always be grateful for the opportunity that you have given me. I would like to thank Dr. Li Song, who agreed to serve as my committee chair after Dr. Cai's departure from the University of Oklahoma. It has been a pleasure to take your classes and also contribute to your research projects during my OU journey. I would like to thank Dr. Hamidreza Shabgard, who introduced me to the topic of Phase Change Materials as an undergraduate student through his collaboration with Dr. Cai. I have also had the pleasure of taking your classes and serving as your Graduate Teaching Assistant. I would like to thank Dr. Choon Yik Tang for serving on my committee and contributing your feedback to my research endeavors. I would like to thank Dr. Wilson Merchán-Merchán for agreeing to join my committee at a later stage. It was a pleasure to work with you during my PhD journey as a Graduate Teaching Assistant.

I would like to thank my former lab mates: Zhimin Jiang, Haopeng Liu, Aly Elhefny, Chibuoke Eneh and Jerson Sanchez. It was a pleasure to collaborate with you on various projects and to build lifelong connections with you.

I would like to thank Dr. Ramkumar Parthasarathy for his continued support during my PhD studies. I would also like to thank Greg Williams and Billy Mays, who were always enthusiastic to provide any support in my research endeavors.

I would like to thank my family who supported me throughout this journey. To my mother Ntombifuthi Hlanze and late father Sithembiso Hlanze, you are the foundation from which I have grown and succeeded throughout my life. It is through your sacrifices that I received the best education in Eswatini and had the opportunity to pursue my higher education in the United States. I will forever be grateful for your love and support.

Most importantly, I would like to thank my wife, Norlia. Your unwavering support throughout my OU journey has given me the strength to persevere through this challenging undertaking. This achievement is as much yours as it is mine. I want to continue to grow to be a better partner for you and am excited for whatever life has in store for us.

Table of Contents

Acknowledgements iv
List of Tables vii
List of Figures viii
Abstract x
1. Introduction 1
1.1 Literature Review 2
1.2 Research Objectives and Questions 9
1.3 Research Contributions 9
2. In-Duct Phase Change Material-Based Energy Storage to Enhance Building Demand Flexibility 13
2.1 Co-Simulation Platform with EnergyPlus and Simulink 14
2.2 EnergyPlus Envelope Model for the DOE Medium Office Building Prototype 16
2.3 PCM Model 16
2.4 Variable Speed Air-Conditioning System Model 27
2.5 Other Simulation Settings 28
2.6 Co-Simulation Results and Discussion 29
2.7 Concluding Remarks 51
3. Full Scale PCM TES Prototype Development 53
3.1 In-Duct PCM Storage Module Prototype 53
3.2 Experimental Evaluation 54
3.3 Comparison of Wall Mounted and PCM in Rack TES solutions 59
3.4 Concluding Remarks 60
4. Model-Based Predictive Control of Multi-Stage Air-Source Heat Pumps Integrated with Phase Change Material-Embedded Ceilings 61
4.1 Integrated Air-Source Heat Pump System Description 61
4.2 Simulation Test Bed 64
4.3 Control Strategies 75
4.4 Case Study Results 83
4.5 Concluding Remarks 101
5. Summary and Future Work 103
5.1 Summary 103
5.2 Future Work 104
References 106

List of Tables

Table 1: PCM module fin dimensions 24

Table 2**:** PCM thermal properties 24

Table 3: Summary of on-peak thermal loads and electric energy consumption for the representative days 34

Table 4: Summer energy and demand rates for the five locations 45

Table 5: Cooling season total energy consumption and electricity cost 47

Table 6: Economic analysis results for the proposed PCM solution in the candidate cities 50

Table 7: Static pressure rise across the PCM TES at different airflow rates 59

Table 8: QCurve coefficients for compressor stage 1 and 2 72

Table 9: PCM charging runtime fraction schedule 76

Table 10: Summer TOU electricity rates 84

Table 11: Summary of 3-day simulation results for four control cases 100

List of Figures

Figure 1: Proposed PCM storage location 14
Figure 2**:** Schematic diagram of the EnergyPlus- Simulink co-simulation platform..... 16
Figure 3**:** PCM model node arrangement..... 19
Figure 4: PCM panel prototype. (a) Thermocouple placement inside the panel. (b) Experimental setup inside a supply duct with a controlled SAT..... 23
Figure 5: Fin Geometry..... 24
Figure 6: Comparison of PCM temperature variations from experimental data (red), original PCM model (blue) and modified PCM model (black) 26
Figure **7:** PCM dynamics for each floor during a hot and humid day (Miami) a) Post-PCM air temperature b) Air-to-PCM charge/discharge rate, and c) PCM liquid volume fraction. 31
Figure 8**:** Total HVAC sensible cooling load profile for a a) hot-humid day (Miami) and b) hot-dry day (Phoenix)..... 35
Figure 9: Total HVAC latent load profile for a a) hot-humid day (Miami) and b) hot-dry day (Phoenix)..... 35
Figure 10: Zone relative humidity profile for a a) hot-humid day (Miami) and b) hot-dry day (Phoenix)..... 36
Figure 11: Total HVAC load profile for a a) hot-humid day (Miami) and b) hot-dry day (Phoenix) 36
Figure 12**:** Total compressor and condenser fan electric power profile for a a) hot-humid day (Miami) and b) hot-dry day (Phoenix)..... 37
Figure 13: Cycle COP profile for a a) hot-humid day (Miami) and b) hot-dry day (Phoenix) 38
Figure 14**:**Total fan electric power profile for a a) hot-humid day (Miami) and b) hot-dry day (Phoenix)..... 39
Figure 15: Total HVAC electric power profile for a a) hot-humid day (Miami) and b) hot-dry day (Phoenix)..... 40
Figure 16: System COP profile for a a) hot-humid day (Miami) and b) hot-dry day (Phoenix).. 40
Figure 17: Zone temperature profile for a a) hot-humid day (Miami) and b) hot-dry day (Phoenix) 42
Figure 18**:** Seasonal a) on-peak electricity consumed by HVAC system and b) energy cost for the baseline and PCM-equipped cases in various cities 46
Figure 19: a) Nominal cooling capacity determined by EnergyPlus and b) total PCM mass in various cities 51
Figure 20: PCM TES prototype 54
Figure 21: Experimental test rig consisting of a) outdoor unit in a psychrometric chamber and b) indoor environment test loop 55
Figure 22: Progression of PCM freezing at various stage - a) initial state, b) ~1 hour, c) ~2.5 hours and d) end of freeze period (~3 hours)..... 57
Figure 23: Progression of PCM melting at various stages - a) ~1 hour, b) ~2 hours, c) ~2.5 hours and d) end of melt period (~3 hours) 58
Figure 24: ASIHP schematic diagram and the prototype unit in the laboratory—a) SC mode and b) PCM charging mode..... 63
Figure 25: Schematic diagram of the EnergyPlus-Python co-simulation platform 66
Figure 26: PCM finite control volume schematic..... 67
Figure 27: Building RC thermal network diagram 70

Figure 28: Thermal network model validation results for cooling load prediction 71
Figure 29: ASIHP model validation results for the PCM charging (top) and space cooling (bottom) modes 74
Figure 30: PCM temperature-enthalpy curve 79
Figure 31: OAT and ZAT profile for the 3-day simulation of BC, RBC, MPC and MPC-PCM cases 85
Figure 32: Zone sensible cooling rate profile for the 3-day simulation of BC and RBC cases.... 89
Figure 33: Zone total cooling rate profile for the 3-day simulation of BC and RBC cases..... 89
Figure 34: Total HVAC power profile for the 3-day simulation of BC and RBC cases 90
Figure 35: Compressor speed level profile for the 3-day simulation of BC and RBC cases..... 90
Figure 36: COP profile for the 3-day simulation of BC and RBC cases 91
Figure 37: Zone sensible cooling rate profile for the 3-day simulation of BC and MPC cases ... 92
Figure 38: Zone total cooling rate profile for the 3-day simulation of BC and MPC cases 93
Figure 39: Total HVAC power profile for the 3-day simulation of BC and MPC cases..... 93
Figure 40: Compressor speed level profile for the 3-day simulation of BC and MPC cases 94
Figure 41: Zone sensible cooling rate profile for the 3-day simulation of BC and MPC-PCM cases 97
Figure 42: Zone total cooling rate profile for the 3-day simulation of BC and MPC-PCM cases 97
Figure 43: Total HVAC power profile for the 3-day simulation of BC and MPC-PCM cases.... 98
Figure 44: Compressor speed level profile for the 3-day simulation of BC and MPC-PCM cases 98
Figure 45: COP profile for the 3-day simulation of BC and MPC-PCM cases..... 99
Figure 46: LVF profile for the 3-day simulation of RBC and MPC-PCM cases 99

Abstract

The global transition from fossil-based to renewable energy sources has introduced significant variability in electricity supply, particularly due to the intermittent nature of solar energy. This variability has led to increased reliance on fossil fuel power plants during peak demand periods, exacerbating grid instability and carbon emissions. Buildings, which account for approximately 73% of total electricity consumption in the United States—with HVAC systems alone responsible for 27% and 30% of commercial and residential usage, respectively—present a critical opportunity for demand-side flexibility. Thermal energy storage (TES) systems, particularly those utilizing phase change materials (PCMs), offer a promising solution to mitigate the mismatch between energy supply and demand. This dissertation presents two studies that demonstrate the potential of PCM TES to improve the demand-side flexibility of HVAC systems.

Firstly, a novel energy storage solution is proposed by incorporating phase change material (PCM) panels in supply ducts to increase a building's thermal storage capacity and demand flexibility. During off-peak hours, the system runs at a supply air temperature (SAT) below the PCM solidification point to charge the storage unit with "cooling" energy. During on-peak hours, a higher SAT is utilized so that the stored "cooling" energy can be discharged into the supply-air as a means to reduce the peak air-conditioning power usage. To evaluate the potentials of peak demand reduction and utility cost savings, a numerical model for a PCM panel prototype and its heat exchange with the air flow in the duct was developed and calibrated using experimental data. Whole building energy simulations were conducted in a co-simulation environment that has integrated the developed PCM model, EnergyPlus Department of Energy (DOE) prototypical model for a medium office building and a calibrated model for variable-speed direct-expansion cooling systems. The simulations covered five cities in different U.S. climate zones over a three-

month cooling season and used actual time-of-use (TOU) rate schedules offered by the local electric utility companies. The simulation results have shown the PCM storage could reduce the on-peak energy consumption by 23-32% and the seasonal cooling electricity cost by up to 16%, with a simple rule-based control strategy. A simple payback analysis resulted in payback periods from 7.5 to 27 cooling months.

Secondly, a model-based predictive control strategy is developed to optimize the operations of phase change material (PCM) ceiling panels coupled with a multi-stage air-source heat pump. A three-stage prototype heat pump unit has been built and tested in the laboratory, with the low and medium stages designed for space heating/cooling and the high compression stage dedicated to charging of the PCM energy storage. To facilitate optimal control of the integrated heat pump system, a mixed-integer linear programming formulation is derived through linearization of the heat pump model and a mixed-integer reformulation of the PCM dynamic governing equations. A predictive control strategy is synthesized based on the resultant control formulation and implemented in a receding horizon scheme that optimizes the PCM charging and the zone temperature schedules simultaneously to leverage both the passive (associated with building construction materials) and active (PCM) storage capacities of a building. The control strategy has been tested along with three benchmarking control scenarios using a co-simulation platform for a prototypical detached house in Atlanta, GA. Test results showed that application of the proposed control strategy to the PCM-integrated heat pump could provide 27.1% electricity cost savings while a fine tuned rule-based control strategy could achieve cost savings of 20.4%, compared to a baseline case without PCM storage, under a time-of-use rate tariff.

1. Introduction

While the increasing migration of energy sources from non-renewable to renewable has provided an alternative to fossil fuels with much reduced greenhouse gas emissions, their limited window of availability (particularly solar energy) has resulted in the rapid ramping of fossil fuel power plants to make up for the energy shortfall during the evening hours [1]. The misalignment of supply and demand is increasing the pressure on the electric grid to maintain reliable and efficient operations. One of the most cost-effective solutions in mitigating the supply and demand balancing issue is to shift the load of the grid from peak periods to off-peak hours. In the U.S., commercial and residential buildings together account for about 73% of the total electricity consumption; Heating, Ventilation and Air-Conditioning (HVAC) systems account for 27% and 30% of the electricity in commercial and residential buildings, respectively [2] [3]. Furthermore, the square footage of commercial and residential buildings increased by 78% and 73% between 1978 and 2008, respectively [4]. This trend indicates that buildings and their HVAC systems will continue to be a significant contributor to the U.S. electricity consumption, which makes buildings an attractive area to implement energy savings and peak load reduction strategies. Thermal energy storage (TES) can be implemented in buildings using sensible or latent heat to alleviate the electrical power supply and demand imbalance issues on the electric grid [5] [6] [7] [8] [9]. Sensible heat storage involves using a building's thermal mass as a virtual battery by increasing or decreasing the temperature of the building envelope while latent heat storage makes use of the heat of fusion of a phase change material (PCM) to input/release energy into/from the material during the phase change process.

1.1 Literature Review

The use of PCM as latent heat storage in buildings has been investigated in many studies. Iten *et al.* [5] conducted a review of free cooling TES and PCM incorporated in building envelopes to increase building thermal mass. For this design, charging and discharging of the energy storage is driven by variation of the outdoor or indoor temperature. Saffari *et al.* [10] investigated the energy savings and comfort improvement potentials for PCM-embedded walls. The PCM performed as a thermal barrier between the hot ambient air and the conditioned indoor space, which decreased the interior wall surface temperature and allowed for the occupant's comfort to be maintained with a higher indoor air temperature. This resulted in a maximum annual energy savings of 11-15% in Madrid, Spain. Neeper [11] investigated the thermal dynamics of a wallboard impregnated with PCM. The study found that the maximum diurnal energy storage occurs at a value of the PCM melt temperature close to the average room temperature in most circumstances. The diurnal storage that can be achieved in practice may be limited to a range of 300–400 kJ/m^2, even if the wallboard has a greater latent capacity. However, the investigation used a pre-determined hourly room temperature profile, and the effect of the PCM on the room temperature was not considered. Sleiti and Naimaster [12] investigated the performance of organic (fatty acid based) PCM products in ceiling construction for a simulated quick service restaurant located in Atlanta, GA. The study found that the PCM storage considered was not able to achieve any significant HVAC energy savings, because the energy stored in the PCM during the day was released back to the indoor space at night. However, there is potential for energy cost savings if this is conducted with time-of-use (TOU) rate schedules. In a combined experimental and numerical study, Athienitis *et al.* [13] investigated the potential of a PCM-impregnated gypsum board to alleviate the overheating of a passive solar heated test room with south facing windows during a winter day. The PCM was

able to absorb the excess heat and reduced the maximum indoor air temperature by 4 °C and maximum indoor wall surface temperature by 6 °C, which improved thermal comfort. Lin *et al.* [14] studied the inclusion of a PCM layer between electrical heating elements (below the PCM) and air plenum (above the PCM) in an under-floor air distribution system. The electrical heating was energized during the nighttime hours to melt the PCM and store heat and turned off during the peak daytime hours while the supply fans blew circulation air over the PCM layer to carry the released heat to the indoor space. PCM has also been incorporated in window panes and shutters to minimize solar heat gains through the window [15] [16]. One of the limitations for the above-mentioned passive systems is that the air-to-PCM heat transfer is low due to the reliance on natural convection, and the small temperature difference limits the effectiveness and heat penetration depth in the PCM.

Harvesting free "cooling energy" using a TES is a promising technique that involves using cold nighttime air to cool the indoor space during the day [17]. At night, cold outdoor air is circulated through the PCM storage unit, which solidifies the PCM and stores "cooling" energy in it. During the day, hot air from the room is circulated through the PCM storage unit, which melts the PCM and delivers cooled air to the indoor space. Zalba *et al.* [18] designed an experimental installation to study a PCM free cooling system using an air-to-PCM heat exchanger. They developed a characteristic model to estimate the melting and solidification time using the thickness of the PCM encapsulation, the inlet temperature of the air, and the air flow rate. Mosaffa *et al.* [19] performed a numerical investigation on the performance enhancement of a free cooling system using TES units with multiple PCMs in series to maintain a constant air-PCM temperature difference in the airflow direction. They modeled the PCM melting and solidification processes using the heat capacity method and the model was used for optimization of design parameters, e.g., PCM slab

length and thickness, and the air passage width, to achieve the maximum storage COP (defined as the ratio between total heat absorbed by PCM and the cumulative fan energy consumption). Anisur *et al.* [20] investigated analytically and experimentally a shell-tube latent heat storage system using heptadecane with a melting point of 22.33°C. The study found that a higher inlet temperature led to a higher storage COP. Osterman *et al.* [21] studied the performance of a latent heat storage unit experimentally and numerically using Fluent. In the summer, free "cooling" energy was stored in the PCM using cold night air, and in winter months, free heat was stored in the PCM during the day using a solar air collector and released to the indoor space at night. The study found that the largest winter savings occurred in March because of the highest availability of solar heat, and the largest cooling storage occurred in July and August because of the larger diurnal temperature fluctuations. Takeda *et al.* [22] investigated the reduction of the ventilation load during summer in various Japanese cities by installing a packed bed of PCM granules in the supply-air ventilation duct. When the outdoor temperature is lower than the room temperature, two separate streams of outdoor air flow into the room and through the PCM bed to simultaneously charge the PCM and cool the indoor space; the airflow leaving the PCM section is ducted to the ambient. When outdoor air temperature is higher than room air, the induced outdoor air is cooled by the PCM bed first before entering the room. The maximum ventilation load reduction was shown to be up to 62.8% in Kyoto. Yanbing *et al.* [23] analyzed the thermal behavior of a Night Ventilation with PCM Packed Bed Storage (NVP) and determined convective heat transfer coefficients of 12 to 19 $W/m^2 \cdot °C$ and flow pressure drop across the PCM of less than 20 Pa.

A variant of the PCM-assisted nighttime free "cooling" solution is to utilize PCM storage to shift loads to periods with cheaper, instead of completely free, "cooling" resources. The reduced cost stems from higher cooling efficiency and/or lower electricity price. Hong *et al.* [24] performed an

experimental study on the load shifting capabilities of PCM integrated in the supply duct. The variation of the zone temperature of an office space was recorded for two cases when the chiller circuit was turned off during the afternoon hours; in the PCM-equipped case, the supply fan blew air through the PCM section and into the room, and in the baseline case, both the chiller circuit and the fan were turned off. They found that the room air temperature rose by 3°C within an hour for the baseline case and 0.8°C within 2.5 hours for the PCM-equipped case. Subsequently, Hong *et. al* [25] performed a simulation study of the same system, which optimized the charging and discharging schedule to reduce the daily electricity cost. Bypass ducts were employed to prevent the unnecessary loss of energy to the room and through the building envelope when cooling is not required. They found that the optimal schedule reduced the cooling electricity cost by 15.6%. Application of TES to harvest free or low-cost "cooling" energy holds good promise to reduce building energy consumption and cost. However, the requirement of a bypass duct/dampers to achieve active control of charging/discharging significantly increases the upfront cost and required space, limiting widespread deployment of the technology.

PCM TES has also been implemented in solar cooling systems to provide cooling when solar energy is unavailable [17]. For example, Helm *et al.* [26] studied the benefits of a solar-driven absorption cooling system that uses a dry air cooler and a PCM storage unit in series instead of a conventional wet cooling tower in the condensing water loop. They found that energy consumed by the heat rejection can be shifted to night-time or off-peak hours with lower ambient temperatures. Helm *et al.* [27] performed a subsequent study of a similar solar-driven absorption cooling system that consisted of four pilot installations between 7 kW and 90 kW nominal cooling capacity and latent heat storage capacity between 80 kWh and 240 kWh. Annual in situ measurement data demonstrated an increase of the seasonal energy efficiency ratio (SEER) from

8.6 to 11.4, and simulations under different climatic conditions indicated a rise in efficiency of up to 64% compared to a system with solely dry air cooling. Belmonte *et al.* [28] performed a feasibility study for the integration of a dry air cooler and PCM TES in the heat rejection circuit of absorption solar cooling systems for the residential sector in Spain. They found that the dry air cooler and PCM storage could improve the chiller's COP in humid climate regions where the wet cooling tower has limited heat rejection capabilities but deteriorate the COP in hot climate regions where the PCM cannot be effectively charged during nighttime hours.

Dedicated ice storage is a mature latent heat storage solution with validated field deployments [29] [30]. Ice can be stored in tanks and employed to shift the energy demand from on-peak to off-peak hours [31]. Yau and Lee [32] conducted a simulation study using TRNSYS and Typical Meteorological Year (TMY) weather data for Kuala Lumpur. They employed an ice-slurry cooling storage system in a library building, which increased the cumulative energy consumption by 20% compared to the existing system. However, the shifting of the chiller load to the off-peak period led to energy cost savings of about 24%. Morgan and Krarti [33] investigated the peak cooling shifting capability of ice thermal storage in a Colorado elementary school. A 50-ton scroll compressor charges three ice tanks during the night, and the stored cooling is used during the day while the chiller is kept in assist mode to handle unexpected cooling loads. They found that the ice storage system could achieve annual energy cost savings of around 47% for a flat rate tariff of \$0.0164/kWh with a demand charge of \$11.24/kW. Despite the cost savings potential of ice storage systems, their applications are limited to large commercial installations due to the complicated design, high capital investment and maintenance costs.

Previous studies have been conducted leveraging the passive and active thermal storage capabilities of PCM ceiling panels. In most designs, chilled-water (or other heat transfer fluid)

pipes are embedded in PCM-filled panel tiles as part of chilled beams to improve the energy charge rate and thermal penetration. Bogatu *et al.* [34] investigated experimentally the cooling load shifting capability of a macro-encapsulated PCM ceiling panel with embedded water circulation pipes compared to conventional radiant cooling panel and micro-encapsulated PCM gypsum panel in a small office. The PCM charging was controlled using pre-defined schedules and a feedback control logic—the water circulation loop was available from 6 PM to 8 AM and its operation was controlled to maintain an operative temperature setpoint of 22°C. The proposed system successfully shifted the cooling load from on-peak to off-peak periods and achieved a cooling effect during melting between 5.3 W/m^2 and 27.7 W/m^2, which was higher than the PCM gypsum panel but lower than the radiant cooling panel. Skovasja *et al.* [35] investigated the feasibility and performance of a PCM integrated ceiling cooling system through simulation and experimental tests. A layer of PCM was installed between chilled water beams and the room air. The study found that the PCM ceiling cooling system was able to suppress the temperature rebound after the chilled water was shut down, due to increased building thermal inertial. Weinläder *et al.* [36] investigated experimentally the passive cooling performance of two different PCM ceiling prototypes: type 1 with PCM on top of chilled water pipes and type 2 with PCM below chilled water pipes. The PCM TES consisted of three operation modes—passive cooling mode, which discharges the PCM with the chilled water loop deactivated; active cooling mode, which runs the chilled water through the chilled beam and is activated only when the passive cooling mode is not able to regulate the room temperature; and active regeneration mode, which occurs at night and runs the chilled water loop to charge the PCM. They observed that the passive cooling rate of the two designs was similar when measured as a function of the room temperature: cooling effects of 10–15 W/m^2 were measured for a room temperature of 26°C.

Various control strategies have been investigated for operations of PCM energy storage in buildings [37]. For example, de Garcia et al. [38] provided a binary scheduling formulation of optimal charge/discharge control of a PCM TES unit placed in a ventilated façade and implemented a reinforcement learning-based controller. In reference [39], a hierarchical control strategy was introduced for an integrated photovoltaic thermal and PCM storage system used in a residential dwelling. The PCM storage was installed in the air duct with multiple fans/dampers in place to alter the airflow path to switch between the charge, discharge and bypass modes of the PCM TES. A lumped system approach was assumed for the PCM control model, which could lead to suboptimal control performance due to overestimation of the charge/discharge rates. Serale et al. [40] investigated model predictive control (MPC) strategies for a PCM-integrated solar thermal system used for space heating, based on a mixed logical dynamical system-based formulation. The developed controller made use of the piecewise linearity of the PCM storage in determining the optimal pumping speed and storage temperature to minimize energy consumption and indoor discomfort. Up to 32% energy savings were obtained compared to a baseline heuristic controller. Gholamibozanjani et al. devised a similar control strategy that explicitly considers the PCM heat transfer dynamics associated with pure-solid, pure-liquid and two phases for optimal operation of a PCM-filled heat exchanger [41]. Touretzky and Baldea [42] proposed a bi-level operation strategy for a PCM storage tank used in buildings. The top level controller was designed to optimize the operation of the PCM storage unit while the lower-layer controller handled fast disturbance rejection. The scheduling algorithm was reliant on a sequential nonlinear program solver and significant cost savings were reported.

1.2 Research Objectives and Questions

This dissertation investigates two novel PCM-based TES configurations designed to enhance building energy flexibility: (i) PCM panels integrated into HVAC supply ducts, dynamically charged and discharged via supply air temperature (SAT) modulation, and (ii) PCM-embedded ceiling panels coupled with a multi-stage air-source heat pump, optimized through model predictive control (MPC). These systems are evaluated for their potential to reduce peak electricity demand, improve energy efficiency, and enhance economic performance under time-of-use (TOU) tariffs.

To unify the two studies into a cohesive dissertation narrative, the following research questions are proposed:

1. How does the location of PCM integration (duct vs. ceiling) affect thermal charge/discharge efficiency and load shifting potential under varying climate conditions?

2. What are the comparative economic benefits of rule-based vs. model predictive control strategies for PCM TES systems in residential and commercial buildings?

3. How do PCM TES systems impact indoor comfort metrics under dynamic control strategies, and what mitigation strategies are needed?

By synthesizing insights from both studies, this work aims to develop scalable, controllable, and cost-effective TES solutions for residential and commercial buildings.

1.3 Research Contributions

Chapter 2 presents a PCM energy storage solution integrated in the supply duct of HVAC systems, which can be dynamically charged or discharged by adjusting the supply air temperature (SAT) setpoint. Compared to the previously reported PCM energy storage designs, the proposed solution

has a major novelty in its high flexibility and controllability for energy charge and discharge, achieved through dynamic SAT reset, with much reduced installation/retrofit costs (no bypass duct loop required) and minimum comfort impact. Specifically, the unique advantages of the proposed solution include:

- *Low cost*: the storage unit is easy to install and requires little to no retrofits;
- *No disturbance to comfort delivery*: charging/discharging occurs without affecting the indoor temperature;
- *Easy control implementation*: SAT schedules can be easily programmed in building automation systems to enable charging/discharging of the storage;
- *Effective storage utilization*: high heat exchange rate between the storage unit and supply air can be achieved due to forced convection, large heat exchange area and greater temperature difference;
- *Controllable charge/discharge rate*: charge/discharge rate can be dynamically controlled through SAT reset to provide on-demand energy storage.

A comprehensive assessment of the proposed solution in terms of energy cost savings and peak electric demand reduction is presented with the aid of a co-simulation platform that integrates through the functional mock-up interface (FMI) (i) a dynamic model for a PCM storage prototype developed and calibrated with experimental data, (ii) a calibrated variable-speed cooling system model that captures cooling efficiency variation under different SAT settings and load conditions, and (iii) the EnergyPlus prototypical model for medium office buildings. Parametric simulations were carried out for five different climate locations along with representative TOU rate schedules offered by the local utilities. Key simulation results, including energy consumption, electricity

costs, peak electrical demand, payback periods and indoor comfort impact, are reported and discussed in this chapter.

Although a few of the aforementioned studies considered the piecewise linearity of the PCM dynamics during control decision making, no or loose couplings with the heating, ventilation and air-conditioning (HVAC) systems were assumed in exchange for numerical tractability. The high nonlinearity of the HVAC and PCM systems and their strong couplings represent a major challenge for practical control implementations. This paper fills the void by presenting a novel model predictive control approach for PCM ceiling energy storage integrated with an air-source integrated heat pump (ASIHP). The proposed control strategy relies on a mixed-integer linear reformulation of the original nonlinear (nonconvex) control problem and enables simultaneous scheduling of the HVAC and PCM TES operations. Note that although application of mixed-integer programming in building control synthesis is not new (e,g., HVAC optimal scheduling [43], aging-aware building demand response [44], solar-battery asset control in buildings [45], in-duct PCM TES control [46], on-site generation and storage scheduling [47]), this study represents the first attempt to leverage mixed-integer techniques for predictive control of PCM-integrated multi-function heat pumps. Compared to previous studies, the system design amalgamates the following benefits: (i) the active PCM charging using a chilled water loop and water-to-PCM heat exchanger improves the heat penetration depth, (ii) the parallel air and radiant cooling system offers better control flexibility with superb energy performance and (iii) the integrated system offers multiple functions in one unit including space cooling/heating, water heating and energy storage (the water heating function is not considered in this study though). The proposed MPC approach facilitates the realization of the solution package's full potential through optimized system operations to maximize the energy efficiency, demand flexibility and economic benefits.

A comprehensive assessment of the control strategy and the PCM-integrated heat pump was performed with the aid of a co-simulation platform that incorporates through the functional mock-up interface (FMI) (i) a numerical model of the PCM-embedded ceiling, (ii) the ASIHP system model, and (iii) the EnergyPlus prototypical single family detached house model. Key performance assessment results are reported in comparison with three baseline control approaches.

2. In-Duct Phase Change Material-Based Energy Storage to Enhance Building Demand Flexibility[1]

The proposed in-duct PCM latent energy storage solution is displayed in Figure 1. The PCM is located in the supply duct to take advantage of the forced convection heat transfer provided by the circulating air, which improves the heat transfer rates to/from the PCM compared to PCM embedded in the building envelope. The SAT will be lowered to initiate the PCM solidification (PCM charging) and store "cooling" energy in the PCM during periods with low electricity prices and/or low ambient temperatures. During on-peak hours, the SAT is increased to initiate the PCM melting process (PCM discharging) as a means to reduce electrical energy usage and peak demand. The proposed solution can significantly increase the power flexibility of a building and effectively reduce building electricity costs when TOU electricity rates are present. The economic benefit can be even greater for participation in power ancillary service markets [48]. The PCM charging and discharging control can be achieved by pre-programming a SAT schedule within a building management system (BMS) according to the subscribed TOU rate tariff. Although this study focuses on performance assessment of installations in commercial buildings, the solution can also be deployed in residential buildings through appropriate control over supply fan cycling.

[1] The contents of this chapter have been previously published in Hlanze *et al.* [80]

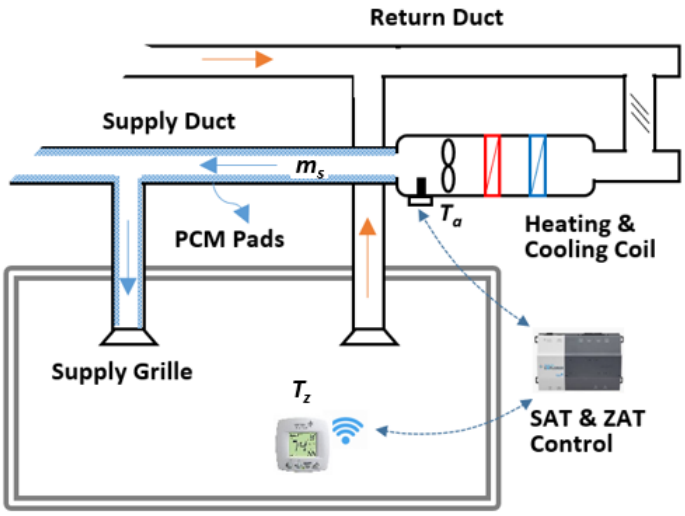


Figure 1: Proposed PCM storage location

2.1 Co-Simulation Platform with EnergyPlus and Simulink

To facilitate performance assessment, a simulation test bed has been constructed based on co-simulation of (i) a numerical model of the proposed PCM storage that was calibrated using experimental data collected for a prototype PCM module, (ii) a variable-speed direct-expansion (DX) cooling system model that has been previously validated with both experimental and manufacturer performance data [49], and (iii) the U.S. Department of Energy (DOE) prototypical medium office building models for five different climate locations [50]. The PCM and DX cooling system models were implemented in MATLAB while the DOE prototypical model is available in EnergyPlus. The overall simulation test bed packages these disparate component models, and co-simulation is achieved through the FMI [51].

An EnergyPlus Functional Mock-up Unit (FMU) has been created for the DOE medium office prototypical building model and is linked to the PCM model and the variable-speed DX system model with the interfacing variables shown in Figure 2. An FMI master program was implemented

in MATLAB Simulink, which manages the progression of simulation time and communications across the component models. In the co-simulation, the interface variables are updated at each time step (10 minutes) in a ping-pong scheme. The variable-speed DX model accepts the return and outdoor air conditions generated by the EnergyPlus FMU and outputs the SAT and relative humidity, which are then fed to the PCM model. Compressor speed is an input variable of the original DX system model. In the test bed, a wrapper was implemented for the DX system model which includes a Newton-type numerical routine to iteratively find the compressor speed to meet the SAT setpoint. In cases of compressor speed saturation, the SAT at the maximum compressor speed is returned by the DX model. The DX system model also outputs the compressor and fan power required to condition the air. The PCM model takes the circulating airflow and SAT and calculates the outlet temperature of the PCM section. The PCM outlet temperature and relative humidity are used as setpoints of the air being distributed to the different variable-air-volume boxes in EnergyPlus. In the EnergyPlus FMU, these setpoints are satisfied using three fictitious coils, namely a dehumidification coil, a sensible cooling coil and a heating coil whose power consumption is not considered in the analysis.

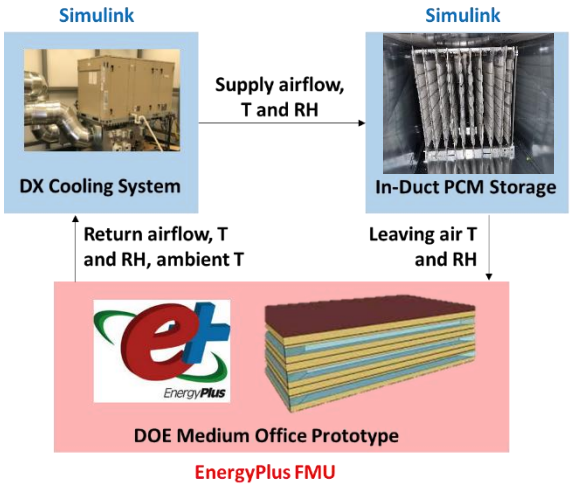


Figure 2**:** Schematic diagram of the EnergyPlus- Simulink co-simulation platform

2.2 EnergyPlus Envelope Model for the DOE Medium Office Building Prototype

The simulation test bed has integrated the envelope model for the DOE prototypical medium office building, which has three floors and 15 conditioned zones (3 core zones and 12 perimeter zones) [52]. Each floor has a dedicated air-handling unit (AHU) and a DX cooling system. Therefore, the overall system model includes three variable-speed DX models with one serving each floor. The three DX models have identical performance but different cooling capacities, which are determined through the auto-sizing engine of EnergyPlus. Each zone has a variable-air-volume terminal box with electric reheat. The test bed includes envelope models for five different climate zones: Miami, FL (1A); Phoenix, AZ (2B); El Paso, TX (3B); New York, NY (4A) and Buffalo, NY (5A). Parametric simulations were conducted for these different cities to understand how the performance of the proposed PCM storage varies with the climate location and the locally available utility rate schedule.

2.3 PCM Model

For the proposed solution, the PCM is encapsulated in an aluminum box that is mounted on the interior surface of the supply duct wall. The physical dimensions of the PCM storage are dependent

on the sizing of the duct and PCM storage, which is described in Section 2.5. The basic PCM model is presented firstly and then a model calibration procedure is described to capture the actual heat transfer characteristics of a PCM panel prototype. Note that the PCM model described in this section is flexible to accommodate other PCMs and encapsulation materials than those used in the prototype panel.

2.3.1 PCM Panel Model

Heat is transferred between the air and PCM through the casing of the PCM panel. The duct wall is externally insulated to minimize heat loss to the surrounding air. The PCM model used in the whole building simulation is adapted from the Enthalpy method [53]. The heat transfer in the PCM is modeled as a one-dimensional conduction-controlled, two-region melting problem in a finite-depth slab. The density of the solid and liquid phases is assumed to be equal ($\rho_s = \rho_l = \rho$) for simplicity. The one-dimensional transient energy equation can be written as:

$$\rho \frac{\partial h}{\partial t} = \frac{\partial}{\partial x}\left(k \frac{\partial T}{\partial x}\right) \tag{1}$$

where h is the PCM enthalpy, t is time, x is distance, k is the PCM thermal conductivity and T is temperature. Enthalpy is defined as a function of the temperature using the following equation:

$$h(T) = \begin{cases} c_{ps}(T - T_m) & T < T_m \\ c_{pl}(T - T_m) + h_{sl} & T > T_m \end{cases} \tag{2}$$

where h_{sl} is the latent heat of fusion of the PCM, T_m is the PCM melting temperature, and c_{pl} and c_{ps} are the liquid and solid specific heat of the PCM, respectively. The PCM enthalpy is assumed to be 0 when the material is fully solidified and its temperature is at the melting point; the enthalpy is negative when the material is in solid phase with temperature below the melting point; the

enthalpy is between 0 and h_{sl} during melting/solidification; and in liquid phase, the material enthalpy is greater than h_{sl}. The PCM thermal conductivity is assigned according to the phase:

$$k(T) = \begin{cases} k_s & T < T_m \\ k_l & T > T_m \end{cases} \tag{3}$$

where k_s and k_l are the solid and liquid thermal conductivities, respectively. Equation (1) is discretized using a forward difference in time and central difference in space, and the enthalpy at the $(n+1)^{th}$ time step is determined as follows:

$$h_j^{n+1} = \frac{\Delta t}{\rho(\Delta x_{PCM})^2}\left(k_{j+\frac{1}{2}}T_{j+1}^n + k_{j-\frac{1}{2}}T_{j-1}^n - \left(k_{j+\frac{1}{2}} + k_{j-\frac{1}{2}}\right)T_j^n\right) + h_j^n \tag{4}$$

where Δt is the time step, Δx_{PCM} is the PCM nodal thickness, and the location and time are represented by j and n, respectively. Figure 3 displays how the nodes in the PCM are arranged. The PCM is divided into N nodes. Two dedicated nodes are used to capture the dynamics of the PCM casing, that separates the supply air stream and PCM, and the supply duct wall, respectively. The thermal conductivities at the half-grid, $k_{j+½}$ and $k_{j-½}$, are calculated using the harmonic mean:

$$k_{j+\frac{1}{2}} = \frac{2k_j k_{j+1}}{k_j + k_{j+1}} \tag{5}$$

$$k_{j-\frac{1}{2}} = \frac{2k_j k_{j-1}}{k_j + k_{j-1}} \tag{6}$$

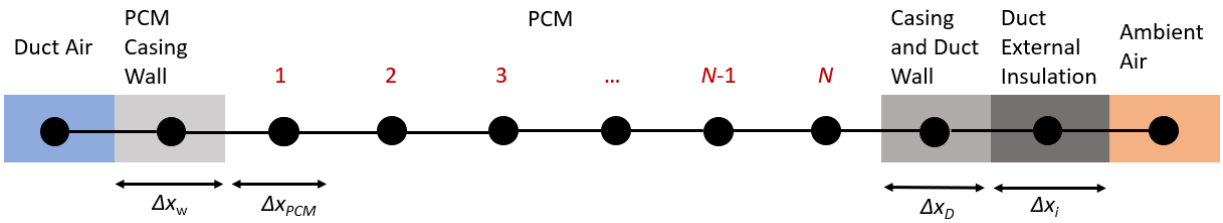


Figure 3: PCM model node arrangement

The enthalpy of the first PCM node is calculated using

$$h_1^{n+1} = \frac{\Delta t}{\rho(\Delta x_{PCM})}\left(\dot{Q}_{out} - \frac{k_{1+\frac{1}{2}}(T_1^n - T_2^n)}{\Delta x_{PCM}}\right) + h_1^n \tag{7}$$

and

$$\dot{Q}_{out} = \frac{T_w^n - T_1^n}{\frac{\Delta x_w/2}{k_w} + \frac{\Delta x_{PCM}/2}{k_1}} \tag{8}$$

where T_w is the temperature of the PCM casing wall, T_1 is the temperature of the PCM node adjacent to the wall, and k_w is the casing wall thermal conductivity. The enthalpy at PCM node N, which is adjacent to the duct wall, is calculated using

$$h_N^{n+1} = \frac{\Delta t}{\rho(\Delta x_{PCM})}\left(\frac{k_{N-\frac{1}{2}}(T_{N-1}^n - T_N^n)}{\Delta x_{PCM}} - \frac{T_N^n - T_D^n}{\frac{\Delta x_D/2}{k_D} + \frac{\Delta x_{PCM}/2}{k_N}}\right) + h_N^n \tag{9}$$

where T_D is the average temperature of the combined PCM casing and duct wall, Δx_D is the sum of the casing and duct wall thicknesses, and k_D is the effective thermal conductivity of the casing and duct that are connected in series. Once the enthalpy at each node is determined, the temperature of the PCM in the new time step is found using

$$T_j^{n+1} = \begin{cases} T_m + \dfrac{h_j^{n+1}}{c_{ps}} & h_j^{n+1} \le 0 \quad (solid) \\ T_m & 0 < h_j^{n+1} < h_{sl} \quad (interface) \\ T_m + \dfrac{h_j^{n+1} - h_{sl}}{c_{pl}} & h_j^{n+1} \ge h_{sl} \quad (liquid) \end{cases} \tag{10}$$

The heat transfer into the lumped casing and duct wall is calculated as

$$m_D c_D \frac{T_D^{n+1} - T_D^n}{\Delta t} = \frac{T_N^n - T_D^n}{\frac{\Delta x_D/2}{k_D A} + \frac{\Delta x_{PCM}/2}{k_{PCM} A}} - \frac{T_D^n - T_{amb}^n}{\frac{\Delta x_D/2}{k_D A} + \frac{\Delta x_i}{k_i A} + \left(\frac{U_{amb,s} A}{2} + \frac{U_{amb,t} A}{4} + \frac{U_{amb,b} A}{4}\right)^{-1}} \tag{11}$$

where m_D is the mass of duct wall, c_D is the duct wall specific heat, T_{amb} is the temperature of the air surrounding the duct (can be either outdoor or indoor air temperature depending on where the storage is installed), Δx_i is the insulation thickness, k_i is the insulation thermal conductivity, and A is the cross-sectional area of a PCM panel perpendicular to the air flow. Rectangular ducts are assumed with two side walls, one top wall and one bottom wall for the PCM panel installations. The side, top and bottom external convective heat transfer coefficients ($U_{amb,s}$, $U_{amb,t}$ and $U_{amb,b}$) between the exterior surface of the external insulation and the surrounding air are calculated as

$$U_{amb} = \frac{\overline{Nu}_L k_a}{L} \tag{12}$$

where $\overline{Nu}_L$ is the average Nusselt number, k_a is the thermal conductivity of the air and L is the characteristic length of the duct. These coefficients capture the different natural convection heat exchanges that result from the warmer ambient air being cooled by the top, side and bottom

external duct surfaces, and are combined in Equation (11) to determine the overall thermal resistance due to external natural convection. The average Nusselt number for a specific orientation is calculated as

$$\overline{Nu}_{L,s} = \left\{0.825 + \frac{0.387Ra_L^{1/6}}{[1+(0.492/Pr)^{9/16}]^{8/27}}\right\}^2 \tag{13}$$

$$\overline{Nu}_{L,t} = 0.52Ra_L^{1/5} \tag{14}$$

$$\overline{Nu}_{L,b} = 0.54Ra_L^{1/4} \tag{15}$$

where Ra_L is the Rayleigh number and Pr is the Prandtl number [54]. The correlations used in Equations (13), (14) and (15) were developed by Churchill and Chu [55], Birkebak and Abdulkadir [56], and Lloyd and Moran [57], respectively.

The temperature of the PCM casing wall is updated using

$$m_w c_w \frac{T_w^{n+1} - T_w^n}{\Delta t} = \frac{T_{air}^n - T_w^n}{\frac{1}{U_{sa}A} + \frac{\Delta x_w/2}{k_w A}} - \frac{T_w^n - T_1^n}{\frac{\Delta x_w/2}{k_w A} + \frac{\Delta x_{PCM}/2}{k_{PCM} A}} \tag{16}$$

where m_w is the mass of the PCM casing wall, c_w is the specific heat of the PCM casing wall, T_{air} is the temperature of the overflowing air, Δx_w is the casing wall thickness. The air-to-casing wall heat transfer is modeled using the Dittus-Boelter correlation [54] for internal turbulent flow:

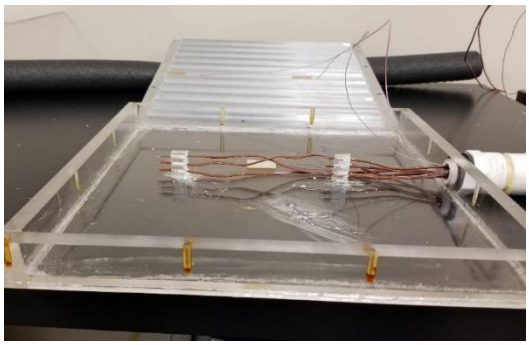
$$U_{sa} = 0.023Re_D^{4/5}Pr^b\frac{k_a}{D_h} \tag{17}$$

where Re_D is the Reynolds number, D_h is the hydraulic diameter, and b is 0.4 for PCM cooling and 0.3 for PCM heating.

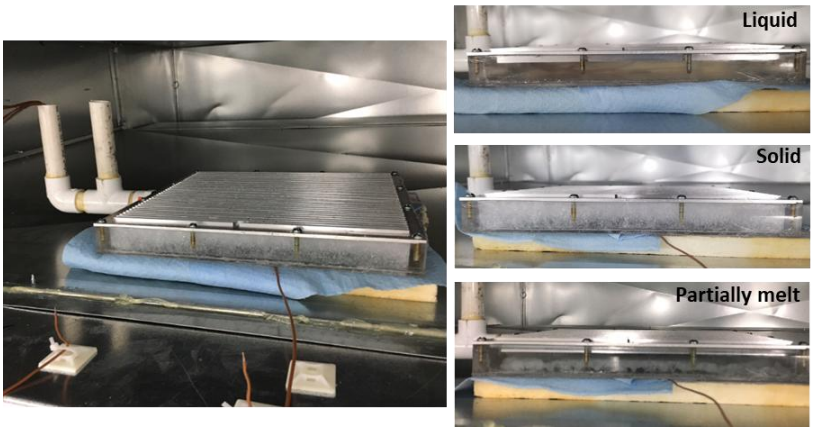
2.3.2 PCM Panel Model Calibration

Figure 4 displays a PCM panel prototype with added aluminum fins to enhance the heat transfer between the overflowing air and PCM. The panel prototype is made with a 1" deep acrylic tray that is filled with PCM and covered by a finned aluminum sheet. The fin geometry is displayed in Figure 5 and Table 1. There are 38 fins with a length of 11" along the air flow direction in the duct. Acrylic walls are used to allow visualization of the solidification/melting processes. A total of 5 thermocouples are placed in the tray at 0.25" depth intervals. The PCM used in the experiment was PureTemp 15, which is a biobased PCM with a nominal melting point of 15˚C [58]. However, experiments in the lab showed an actual fusion temperature of 13.5 °C, which was used in the PCM model. Thermal properties of the material, such as density, specific heat and thermal conductivities, were obtained from the manufacturer performance data and are reported in Table 2. The effects of the heat transfer enhancement due to the fins and natural convection within the liquid PCM is accounted for in the model by introducing three enhancement factors applied to the air-side convective heat transfer coefficient, and the solid and liquid PCM thermal conductivities:

$$\begin{aligned} U_{sa,enhanced} &= U_{sa} \times z_1 \\ k_{s,enhanced} &= k_s \times z_2 \\ k_{l,enhanced} &= k_l \times z_3 \end{aligned} \tag{18}$$



(a)



(b)

Figure 4: PCM panel prototype. (a) Thermocouple placement inside the panel. (b) Experimental setup inside a supply duct with a controlled SAT.

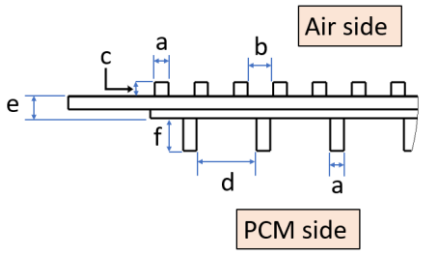


Figure 5: Fin Geometry

Table 1: PCM module fin dimensions

Dimension	a	b	c	d	e	f
Value (in.)	0.100	0.188	0.100	0.406	0.163	0.238

Table 2**:** PCM thermal properties

Thermal Property	T_m (°C)	h_{sl} (kJ/kg)	ρ (kg/m^3)	c_{pl} (J/kg·K)	c_{ps} (J/kg·K)	k_l (W/m·K)	k_s (W/m·K)
Value	13.5	182	905	2560	2250	0.15	0.25

Laboratory tests were performed on the panel prototype to determine the values of the enhancement factors. The experiment was conducted in two stages: the first stage consisted of solidifying the PCM that was initially in the liquid phase, and the second stage consisted of melting the PCM directly after the first stage. The first stage lasted 5.6 hours and the second stage lasted 4.5 hours. During the first stage, the SAT was set to 9 °C, and the airflow rate was set to 700 CFM.

During the second stage, the SAT was raised to 19 °C, and the airflow rate was set to 1475 CFM to achieve a similar heat transfer rate to the first stage.

The enhancement factors z_1, z_2 and z_3 were estimated to be 10.5, 5.3 and 8.7, respectively, using a Levenberg-Marquardt nonlinear regression routine (which is the algorithm used by MATLAB's *nlinfit* function [59]). Figure 6 displays the comparison of the experimentally measured PCM temperatures at various depths with simulation results obtained from models without and with the enhancement factors. The original PCM model was unable to reflect the rate at which the PCM melted/solidified during the experiment. According to the original model, the top temperature was the only one that reached the fusion temperature during the first stage, and it only experienced a rapid decrease (which signifies a complete phase change at that point) after 5 hours. The rest of the PCM remained above the melting temperature for the entire duration of stage 1, which does not match the experimental data. After incorporation of the enhancement factors, the PCM model results are in much better agreement with the experimental data. The potential sources of mismatch include non-ideal phase change due to PCM subcooling, contact resistances and multi-dimensional effects. Besides, the fin depth is lower than the PCM thickness, which causes a non-uniform conductivity enhancement in the PCM. For the temperature at a depth of 0.5", the modified PCM model undergoes rapid solidification and melting at the beginning of the first and second stages. This trend is similar for the other temperature nodes. The durations of the melting and solidification processes are similar but there is a small difference in the final temperature when the phase change is complete. However, for this latent energy storage solution, the latent heat transfer associated with phase change is more important than the sensible storage effect. In the whole building simulations, the enhanced PCM heat transfer model was used.

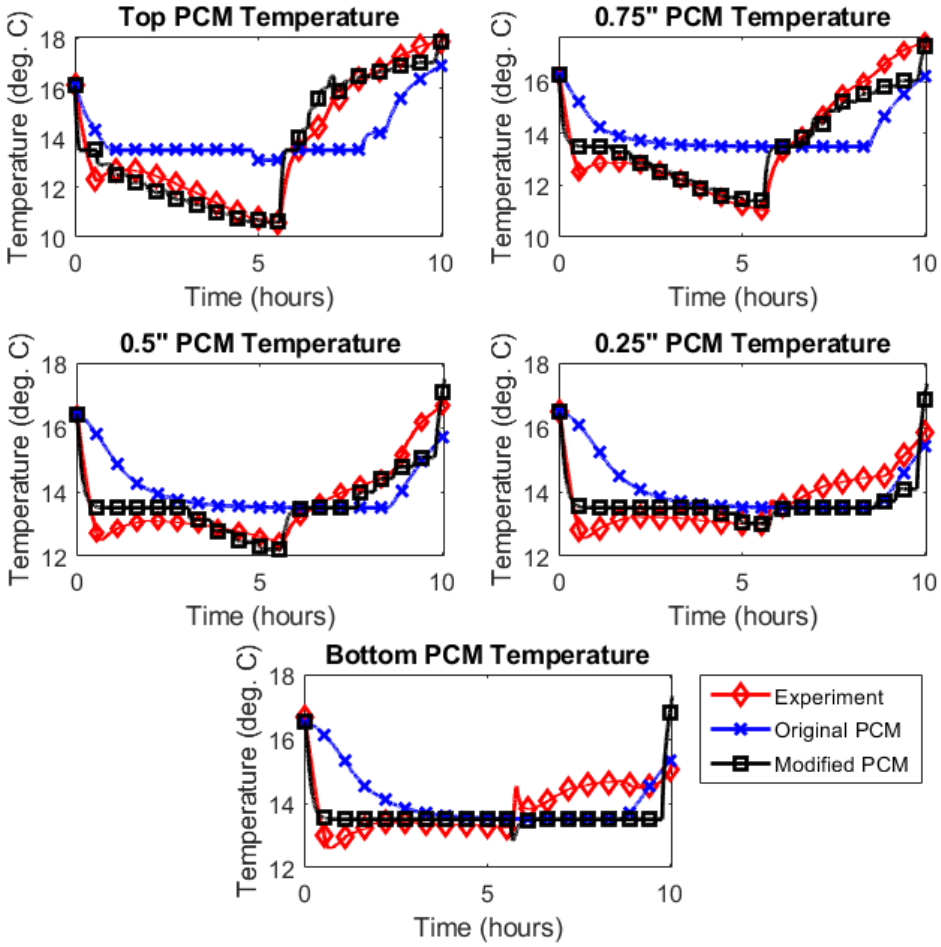


Figure 6: Comparison of PCM temperature variations from experimental data (red), original PCM model (blue) and modified PCM model (black)

2.3.3 Model for PCM Energy Storage Unit

The PCM energy storage is modular in its original design so that multiple panels are required for a specific installation. The length of the duct, covered by the PCM panels, is divided into several segments. The heat transfer between the air and PCM panel in each segment is analyzed using the model described in the previous section. Neighboring segments are thermally coupled through the airflow in the duct: the outlet air of the previous segment is the inlet air to the next segment. The temperature change of the air across a segment is determined using

$$T_{out} = T_{in} - \frac{\dot{Q}_{in}}{\dot{m}_a c_{pa}} \tag{19}$$

where $\dot{m}_a$ is the air mass flow rate and $\dot{Q}_{in}$ is the air-to-PCM panel heat exchange rate in accordance with Equation (16), and the thermal capacitance of the adjacent air is negligible:

$$\dot{Q}_{in} = \frac{T_{air}^n - T_w^n}{\frac{1}{U_{sa}A} + \frac{\Delta x_w/2}{k_w A}} \tag{20}$$

2.4 Variable Speed Air-Conditioning System Model

This study assumes a variable-speed air-conditioning system, the compressor speed of which can be continuously modulated to maintain the SAT setpoint. A previously developed variable-speed DX system model was adopted and integrated in the simulation test bed [49]. The model was extended from the ASHRAE Toolkit model by including additional correlations with respect to the compressor speed for characterization of the system steady-state performance. The final model predicts the total cooling capacity and compressor power based on explicit correlations with the ambient temperature, evaporator inlet wet-bulb temperature, supply airflow rate and compressor speed. The bypass factor method is utilized for the sensible heat ratio calculation. For dry coil scenarios, an iterative procedure is undertaken to identify a fictitious evaporator inlet wet-bulb temperature at which the coil transitions from dry to wet. The model was calibrated with both manufacturer and laboratory-collected performance data for a 5-ton variable-speed rooftop unit. The modeling details and calibration results can be found in [49] .

The simulation study assumes a fixed outdoor air fraction of 15%, i.e., the air-side economizer is absent, and the positions of the outdoor/return air dampers are fixed. This simplification eliminates the complicating factor associated with air-side economizing actions in the assessment of the

demand flexibility enhancement potential of the proposed PCM storage solution. Because of this assumption, the reported utility cost savings potential may be conservative.

2.5 Other Simulation Settings

Baseline cases, which assume normal HVAC operation without the in-duct PCM storage and with a fixed SAT setpoint of 12.7 °C, were considered to quantify potential performance gains that can be brought by the proposed solution. The PCM-equipped case assumes a rule-based PCM charging/discharging control strategy that involves lowering the SAT setpoint to 9.2 °C for six hours (charging period) directly preceding the on-peak period and raising the SAT setpoint to 15.2 °C for the first three hours and to 15.7 °C from the fourth to sixth hour of the on-peak period to discharge the PCM. The PCM charging and discharging periods are both assumed to be six hours long for all considered locations, but the activation time can be different depending on the local rate schedule. For the rest of the day, the SAT setpoint assumes 12.7 °C when mechanical cooling is requested. The simulations were conducted for a 3-month cooling season from the beginning of June to the end of August. The time step in the EnergyPlus simulation was set to ten minutes. To ensure that convergence requirements for the enthalpy method are met, a time step of 0.5 s was used for the PCM model, which is executed inside the MATLAB function block in Simulink 1200 times per EnergyPlus time step. Since the PCM heat transfer model is nonlinear, there is no analytical expression for the maximum stable time step. The 0.5 s time step was identified using trial and error. Note that this small time step requirement is partially attributed to the piece-wise heat transfer characteristics, which introduce significant numerical chattering when larger time steps are used.

The baseline case was simulated for the 3-month cooling season and the day with the highest on-peak total HVAC sensible cooling energy (Q_s) was used in sizing of the PCM storage. For each

floor of the medium office building, the PCM storage was sized with latent heat equal to one tenth of the on-peak HVAC sensible cooling energy use of the peak-demand day:

$$m_{PCM} = \frac{Q_{s,max\ on-peak}}{10\ h_{sl}} \tag{21}$$

This sizing strategy provides a significant load shifting capability during the peak-demand day while ensuring that the PCM storage capacity is still adequately used during days with a lower cooling load. The section of duct leaving the AHU, in which the PCM storage unit is installed, was sized according to the maximum design airflow rate ($\dot{\forall}_{max}$) determined by EnergyPlus. The square duct width (W_d) was determined as

$$W_d = \sqrt{\frac{\dot{\forall}_{max}}{V_{max}}} \tag{22}$$

where V_{max} is the maximum recommended air velocity in a duct (1200 fpm, based on consultation with domain experts). The PCM panel thickness assumed 2.54 cm (1 inch) and total length of the PCM duct section was calculated using the estimated PCM mass and duct width. The PCM length in the airflow direction was divided into 20 subsections for model implementation.

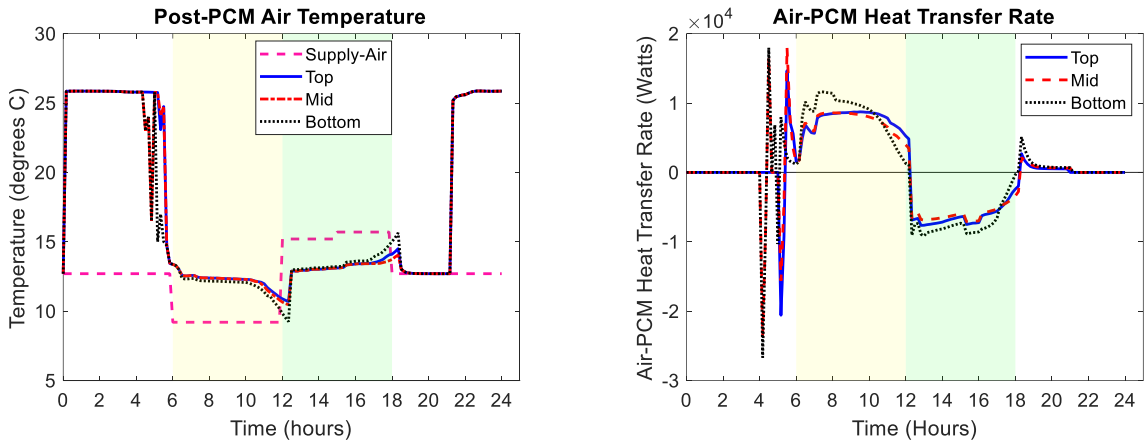
2.6 Co-Simulation Results and Discussion

This section presents the results of the parametric whole-building simulations. First, representative results for a hot-dry day in Phoenix and a hot-humid day in Miami are presented and analyzed. These two days were chosen because they have weather conditions resulting in quite different sensible heat ratio, which can provide insights into how the sensible and latent loads are shifted and their effect on peak demand reduction. Then, the 3-month cooling season loads and energy

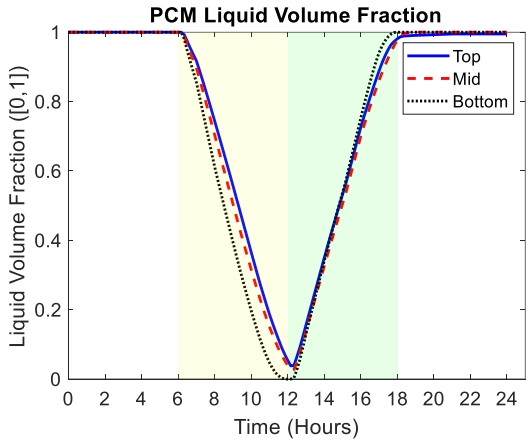
costs are presented for each location to study the seasonal performance. Lastly, the simple payback period for each location is analyzed.

2.6.1 Representative Day Results

The representative day results were obtained for a hot-dry day in Phoenix and a hot-humid day in Miami. The hot-dry and hot-humid days had average outdoor air temperatures and humidity ratios of 35.8°C and 0.0101 kg/kg, and 28.8°C and 0.0183 kg/kg, respectively. Figure 7 presents the simulation results for each floor of the selected hot-humid day in Miami. Figure 7a displays the SAT and post-PCM air temperature. The yellow shaded area represents the PCM charging period, and the green shaded area indicates the PCM discharging period. During the charging process, the air temperature at the PCM section outlet is higher than the SAT, which is due to the heat released to the air by the PCM. During the discharging process, the air temperature at the PCM section outlet is lower than the SAT, which is due to cooling energy discharge from the PCM. Figure 7b depicts the air-to-PCM heat transfer rate profiles, which is the rate that the PCM loses (positive) and gains (negative) thermal energy in the charging and discharging periods, respectively. Figure 7c displays the liquid volume fraction (LVF), which is determined by averaging the nodal ratio of the PCM enthalpy to h_{sl} across all nodes—the nodal ratio is 1 when the nodal enthalpy is greater than h_{sl} and 0 when the nodal enthalpy is less than 0. It signifies how much of the PCM has melted or solidified and how much of the PCM latent heat capacity is utilized during the charging and discharging processes. When LVF is 1, the entire PCM is in liquid phase; when s is 0, the entire PCM is in solid phase. In this simulated day, the PCM begins in a liquid phase with LVF equal to 1. At the end of the charging process, LVF drops to below 0.1, which means that more than 90% of the PCM latent storage capacity is used. In the discharging process, the high SAT initiates melting of the PCM with LVF gradually increasing to 1 by the end of the discharging process.



a) b)



c)

Figure **7:** PCM dynamics for each floor during a hot and humid day (Miami) a) Post-PCM air temperature b) Air-to-PCM charge/discharge rate, and c) PCM liquid volume fraction.

Figure 8 to Figure 17 present the simulated diurnal variations of key operational variables of the baseline and PCM-equipped cases for the representative hot-dry and hot-humid days. The total on-peak cooling loads and HVAC electric energy consumption for these two days are displayed in

Table *3*. The PCM case led to the shifting of almost a third of the total HVAC energy consumption from the on-peak to off-peak periods for both representative days.

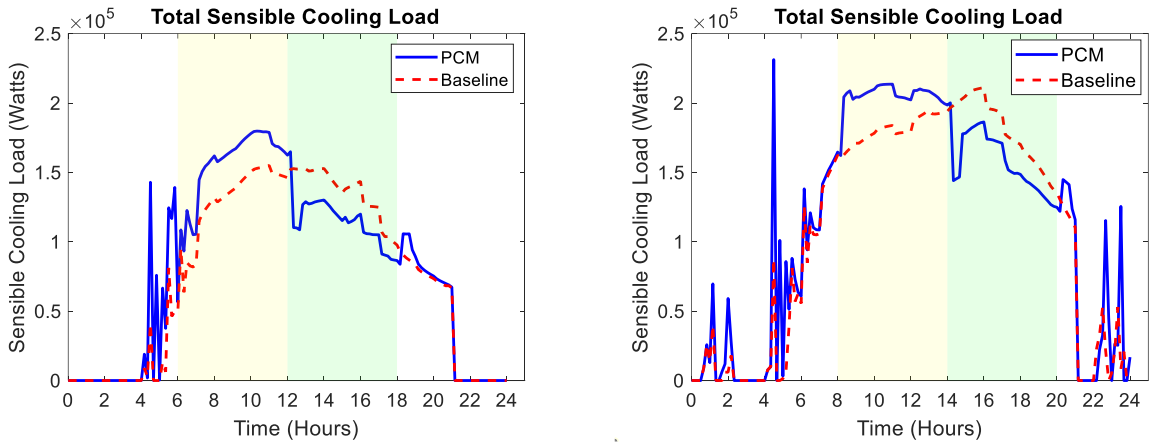
Figure 8 compares the total HVAC sensible cooling load profiles of the baseline and PCM-equipped cases on hot-dry and hot-humid days. The addition of the PCM results in an increase in the HVAC sensible load during the charging period, due to the extra cooling capacity needed to charge the PCM, and a decrease during the discharging period. The PCM charging and discharging occur at different times for the two locations because the TOU electricity rate schedules have different on-peak periods (detailed rate schedules are discussed in Section 2.6.3). The PCM storage leads to daily on-peak sensible load reductions of 13.1% and 16.5% for the hot-dry and hot-humid days, respectively.

Figure 9 shows the HVAC latent cooling load profiles. It can be observed that the latent load is higher during the charging period in the PCM-equipped case because the SAT is lower, which leads to a lower evaporating temperature and more removal of water vapor from the air. Conversely, the SAT is higher in the discharging period, which results in less dehumidification because of the higher evaporating temperature. This latent load shifting effect is not attributed to the presence of the PCM, but the variation of the SAT during the charging and discharging periods. The altered latent load profiles also result in different humidity levels in the indoor spaces. Figure 10 displays a core zone relative humidity profile for the baseline and PCM-equipped cases. During the PCM charging period, the indoor relative humidity is lower for the PCM-equipped case because of the deep dehumidification of the circulating air. During the PCM discharging period, the indoor relative humidity of the PCM-equipped case ramps up fast and surpasses the baseline humidity for a majority of the discharge period. For all the simulated cases, the indoor humidity is maintained below the comfort upper limit of 65% recommended by ASHRAE 55 [60]. For the

hot-humid day (location), the latent cooling load and the indoor humidity are much higher than the hot-dry day due to the higher moisture content of the outdoor air. The overall on-peak latent load reduction produced by the PCM storage is 70% for the hot-dry day and 25.5% for the hot-humid day. Note that the proposed PCM storage is mainly designed for sensible cooling load shifting, while the shifting of dehumidification load is a byproduct of the specific control strategy utilized. Figure 11 displays the total HVAC cooling load profile for the two cases. The amount of total cooling load shifted is 20.2% for the hot-humid day and 18.7% for the hot-dry day.

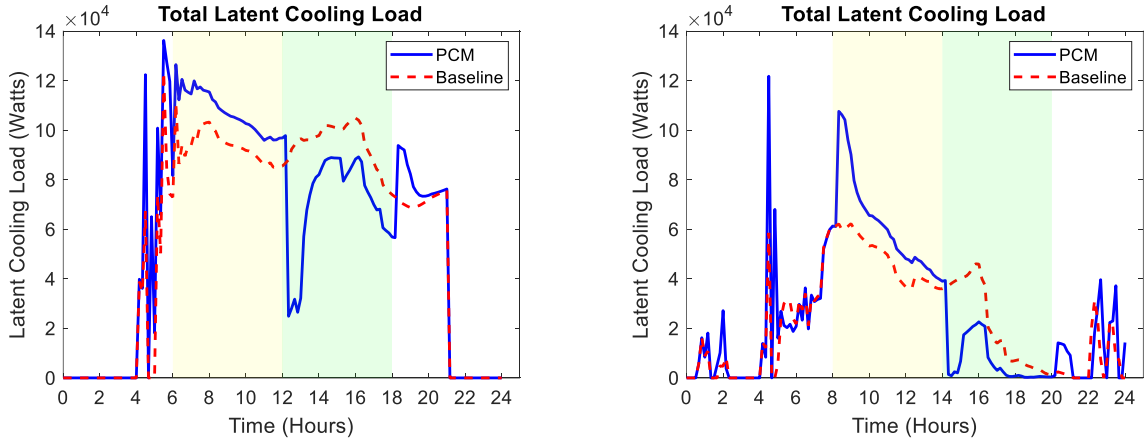
Table 3: Summary of on-peak thermal loads and electric energy consumption for the representative days

	Hot dry day and location			Hot humid day and location		
	Baseline	PCM	Changes	Baseline	PCM	Changes
Sensible Cooling Load (MJ)	3847	3343	504 (↓13.1 %)	2903	2424	479 (↓16.5%)
Latent Cooling Load (MJ)	424	128	296 (↓69.8 %)	2027	1510	517 (↓25.5%)
Total Cooling Load (MJ)	4271	3471	800 (↓18.7 %)	4930	3934	996 (↓20.2%)
Compressor and Condenser Fan Electric Energy (kWh)	419.2	277.1	142.1 (↓33.9 %)	292.6	194.0	98.6 (↓33.7 %)
Supply Fan Electric Energy (kWh)	16.3	19.2	-2.9 (↑17.8 %)	14.3	16.9	-2.6 (↑18.2 %)
Total HVAC Electric Energy (kWh)	435.5	296.3	139.2 (↓32.0 %)	306.9	210.9	96.0 (↓31.3 %)



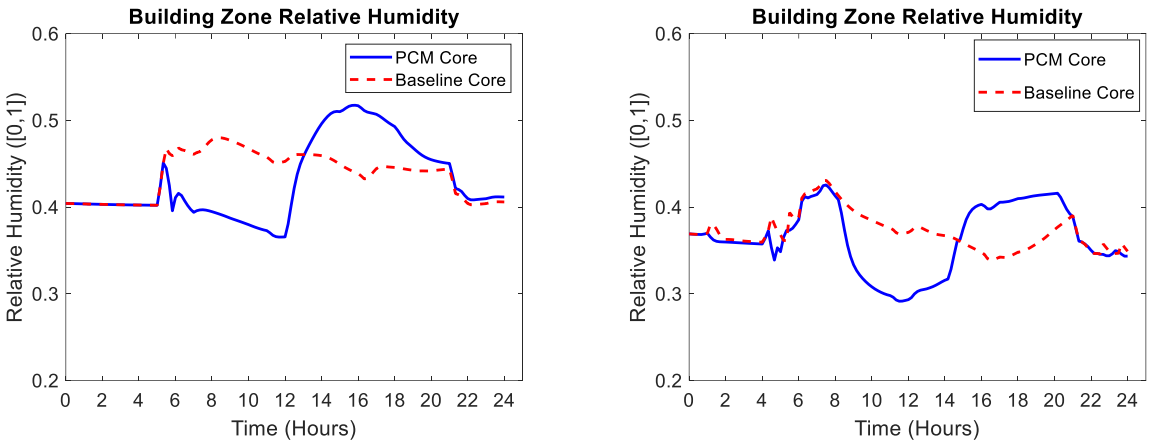
a) b)

Figure 8**:** Total HVAC sensible cooling load profile for a a) hot-humid day (Miami) and b) hot-dry day (Phoenix)



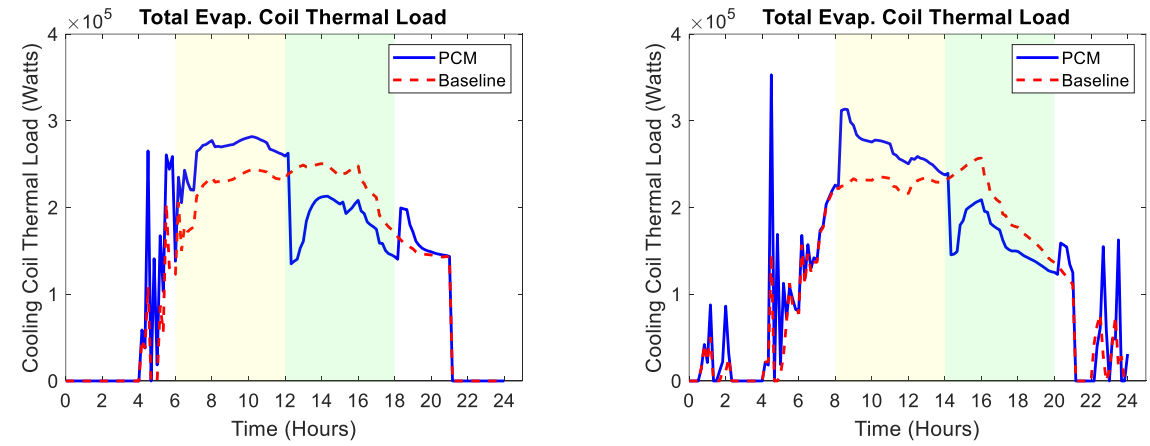
a) b)

Figure 9: Total HVAC latent load profile for a a) hot-humid day (Miami) and b) hot-dry day (Phoenix)



a) b)

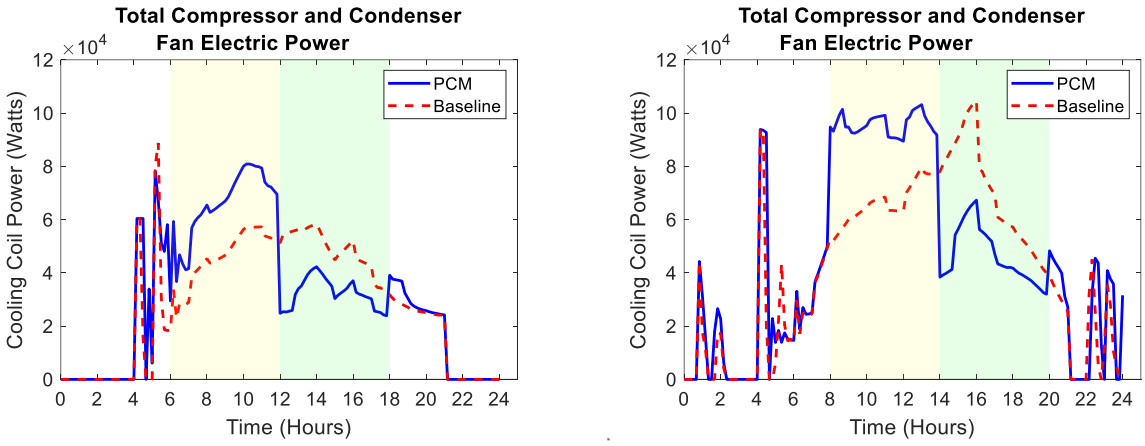
Figure 10: Zone relative humidity profile for a a) hot-humid day (Miami) and b) hot-dry day (Phoenix)



a) b)

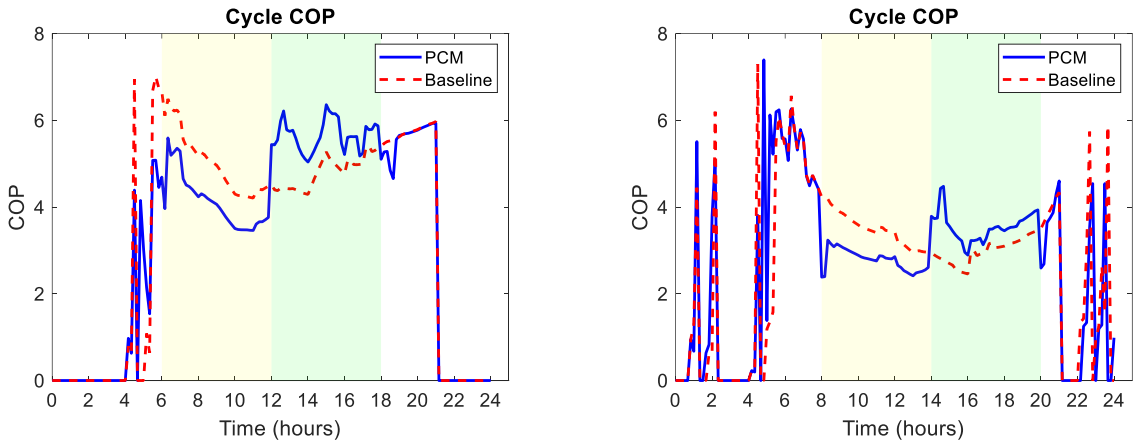
Figure 11: Total HVAC load profile for a a) hot-humid day (Miami) and b) hot-dry day (Phoenix)

Figure 12 displays the total cooling electric power consumption (sum of compressor and condenser fan power) profiles. The amount of the compressor power usage shifted from the on-peak to the off-peak hours on the hot-dry day is close to 33.9 % and a very similar level of electrical power reduction (33.7 %) is achieved for the hot-humid day. It should be noted that the percentage cooling power reduction is much higher than the corresponding thermal load reduction, which is less than 20%. This is mainly due to the higher cycle COP during the on-peak hours, which is defined as the ratio between the total cooling load and the cooling electric power (excluding supply fan power). Figure 13 compares the cycle COP profiles, which clearly shows that the cycle COP is much higher for the PCM-equipped case during the PCM discharging period. This is because a higher SAT would increase the saturated evaporating temperature and reduce the pressure lift across the compressor, resulting in a higher cycle COP.



a) b)

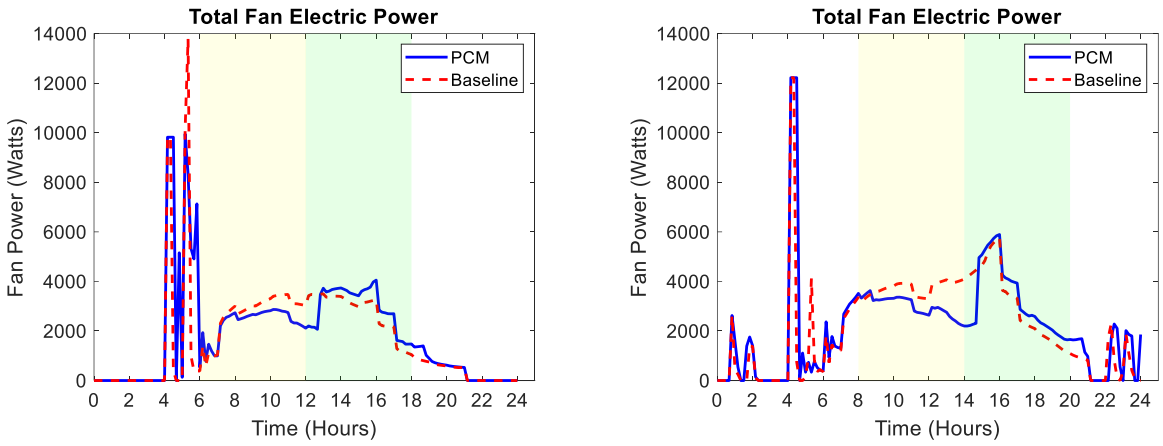
Figure 12**:** Total compressor and condenser fan electric power profile for a a) hot-humid day (Miami) and b) hot-dry day (Phoenix)



a) b)

Figure 13: Cycle COP profile for a a) hot-humid day (Miami) and b) hot-dry day (Phoenix)

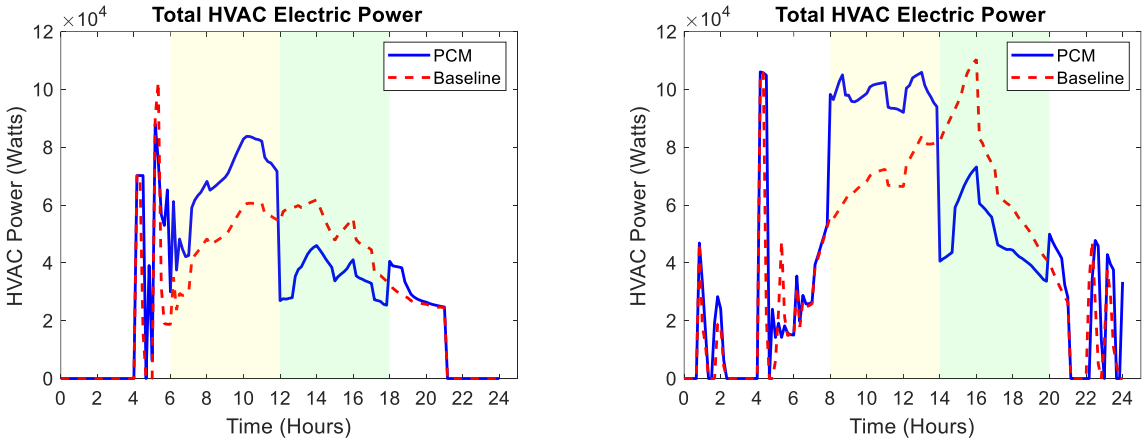
Figure 14 shows the total fan electric power consumption profiles for the baseline and PCM-equipped cases on the hot-dry and hot-humid days. The on-peak fan power usage is higher for the PCM-equipped case on both days, because during the discharging period, the higher SAT requires more airflow to provide the same cooling capacity. However, the fan power represents a small fraction of the total HVAC power usage and the increase of the on-peak fan power can be well compensated for by the compressor power reduction.



a) b)

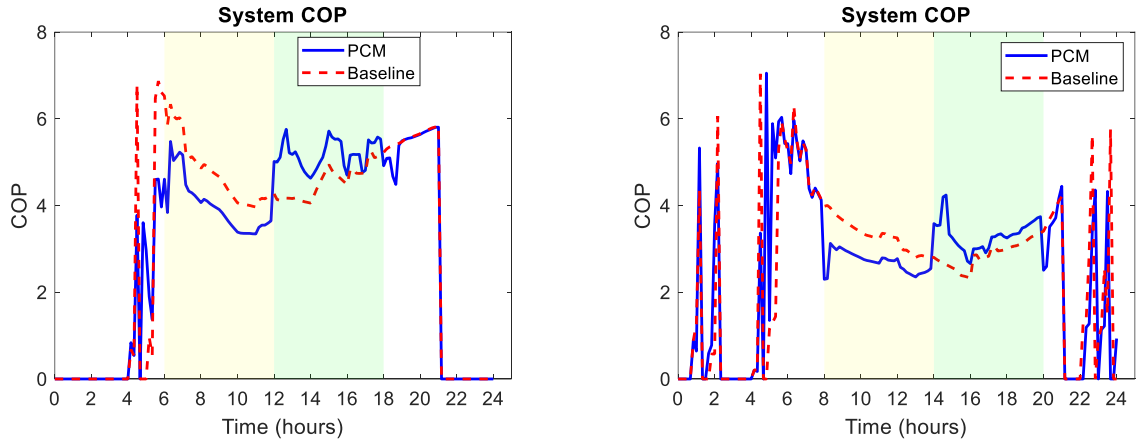
Figure 14**:**Total fan electric power profile for a a) hot-humid day (Miami) and b) hot-dry day (Phoenix)

Figure 15 displays the total HVAC power consumption profiles. Although more fan power is consumed during the on-peak hours for the PCM-equipped case, the compressor power reduction is dominant leading to much reduced on-peak HVAC electricity usage. With the PCM storage, the on-peak HVAC electricity consumption is reduced by 32.0% for the hot-dry day and 31.3% for the hot-humid day. In addition, the (on-peak) peak demand of the HVAC electric power on the hot-dry day is reduced by 37.2 kW, which equates to a reduction of 33.7 % while for the hot-humid day, a peak demand reduction of 25.5 % is achieved. Figure 16 displays the system COP for the baseline and PCM-equipped cases on hot-dry and hot-humid days, which is defined as the ratio between the total cooling load and the total HVAC electric power (including supply fan power). For both days, the system COP is higher during the PCM discharging period for the PCM equipped case, which means that less work input is required to provide the same amount of cooling. The efficiency enhancement in conjunction with the thermal load reduction results in electrical power reduction during the on-peak hours.



a) b)

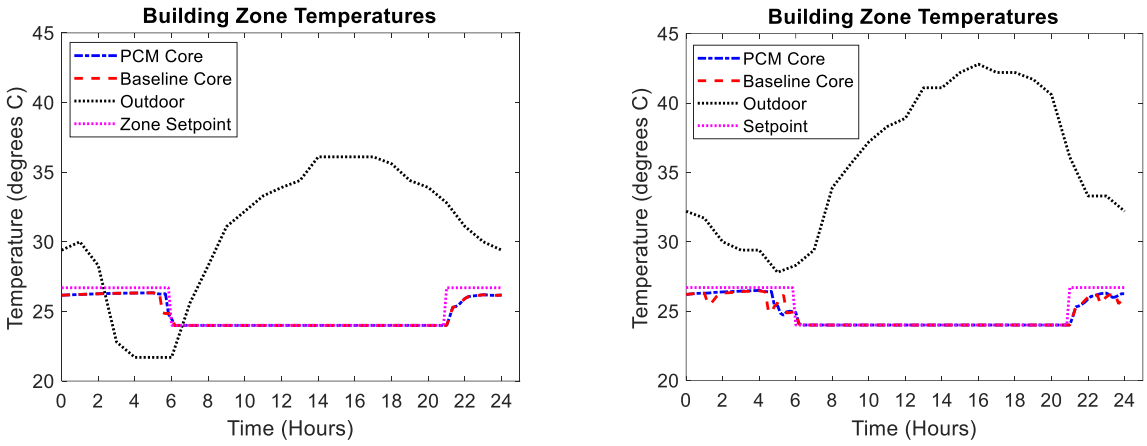
Figure 15: Total HVAC electric power profile for a a) hot-humid day (Miami) and b) hot-dry day (Phoenix)



a) b)

Figure 16: System COP profile for a a) hot-humid day (Miami) and b) hot-dry day (Phoenix)

Figure 17 depicts the variations of the dry-bulb air temperature in a core zone and the ambient temperature for the baseline and PCM-equipped cases. The zone temperature is well maintained at the setpoint of 24 °C during the occupied hours (6 AM to 9 PM), for both the baseline and PCM-equipped cases. To quantify the zone temperature regulation performance, the cumulative zone temperature excursion (the area of the zone temperature variation curve beyond the cooling setpoint) was calculated for both baseline and PCM-equipped cases in Phoenix during occupied hours of the whole simulation period. The cumulative errors for the baseline and PCM-equipped cases over the whole cooling season were 0.8°C-h and 1.4°C-h (average errors of 0.001°C and 0.0015°C), respectively, which are negligible and likely attributed to numerical errors of the EnergyPlus solver. This proves the addition of the PCM storage does not impact indoor temperature control. Figure 10 displays the variation of the relative humidity of the same core zone for the different cases. In both days, the zone relative humidity is maintained in the comfort zone of 0.25 to 0.65, according to ASHRAE 55-2020 and 62.1-2019 [60] [61], during the occupied hours. Therefore, the deployment of the PCM storage does not cause any negative impact on indoor comfort.



a) b)

Figure 17: Zone temperature profile for a a) hot-humid day (Miami) and b) hot-dry day (Phoenix)

2.6.2 Seasonal HVAC Energy Consumption and Cost

The total HVAC energy cost was calculated for each simulated case using representative summer TOU electricity rates offered by electric utility providers serving the five locations. Table 4 presents a breakdown of the utility tariffs used in the simulations. Some tariffs comprise of two charges: the energy charge and the demand charge. The energy charge is the cost of the electrical energy ($/kWh) and is calculated at each timestep according to the specific rate at that time. The demand charge is calculated based on the highest electrical demand, in kW, evaluated over all 30-minute time intervals of an entire month. The energy charge is incurred continuously while the demand charge is a one-time cost for a whole month. The identified tariffs for Miami, Phoenix and El Paso have on-peak and off-peak energy charges and demand charges, whereas, those of New York and Buffalo have on-peak, mid-peak and off-peak energy charges but no demand charge. El Paso has the highest on-to-off peak energy charge ratio of 24, which incentivizes load shifting, and

has the highest demand charge that is assessed at any time of the day, which may cause financial penalties of high off-peak demand caused by load shifting measures. Miami and Phoenix have an on-to-off peak energy charge ratio of 2 and a lower demand charge that is assessed during the on-peak period only. The energy charge in Phoenix is 2.5 times higher than Miami while the demand charge is slightly lower. The cheap electricity in Miami is unfavorable for the proposed demand response measure with long payback periods. New York and Buffalo assume the same electricity tariff which has on-to-off peak and mid-to-off peak energy charge ratios of 16 and 6, respectively. This tariff incentivizes shifting the electric consumption from the on- and mid-peak periods to the off-peak periods.

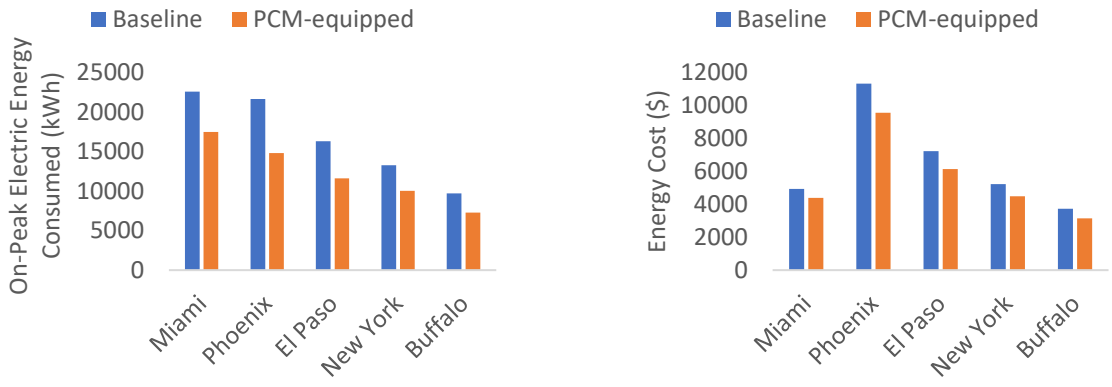
The on-peak HVAC electricity consumption and total HVAC electricity cost are displayed in Figure 18 for the baseline and PCM-equipped cases and for the different locations over the entire 3-month cooling season. The total on-peak electricity consumption is reduced by 22.5% (5095 kWh) in Miami, 31.5% (6838 kWh) in Phoenix, 28.8% (4701 kWh) in El Paso, 24.5% (3258 kWh) in New York and 25.1% (2451 kWh) in Buffalo. Phoenix has the highest on-peak electricity consumption reduction while Miami has the lowest percentage reduction, which can be attributed to several factors. Phoenix is located in a hot and dry climate zone and involves the highest sensible heat ratio (SHR), while for Miami, the latent load contributes a significant portion of the total cooling load. Since the proposed PCM storage is mainly designed for sensible load shifting and is sized according to the peak sensible load, the overall load shifting capability relative to the total load is smaller for hot-humid locations such as Miami. In addition, the discharging period is perfectly aligned with the on-peak period of the electricity tariff for Phoenix, while the Miami tariff involves an on-peak period spanning over nine hours but PCM discharging still terminates at the end of the sixth hour to be consistent across locations. This time misalignment results in

lower percentage reduction of on-peak electricity usage for Miami. Although Miami has the lowest relative reduction in on-peak electricity usage, the absolute reduction ranks second among the five locations.

The total HVAC electricity cost is reduced by $539.00 (10.9%) in Miami, $1767.00 (15.6%) in Phoenix, $1076.00 (14.9%) in El Paso, $726.00 (13.9%) in New York and $591.00 (16.0%) in Buffalo. Despite having the second highest absolute decrease in on-peak electricity consumption, Miami has the lowest absolute electricity cost savings. The ratio between the on-peak and off-peak energy rate and the demand charge are similar for Miami and Phoenix. However, Miami has a significantly lower absolute cost reduction because the on-peak electricity consumption reduction is lower, and the energy rates are 60% lower than Phoenix. For the other four locations than Miami, the relative electricity cost savings is similar and close to 15%.

Table 4: Summer energy and demand rates for the five locations

City	Rate name	Energy rate ($/kWh)			Demand Charge ($/kW)	
		On-Peak	Mid-peak	Off-peak	On-peak	Anytime
Miami	Florida Power & Light Company General Service Demand-TOU (GSDT-1) [62]	0.07078 (12-9PM)	—	0.03272 (12AM-12PM and 9PM-12AM)	9.98	—
Phoenix	Tucson Electric Power Medium General Service Time-of-Use [63]	0.17506 (2-8PM)	—	0.083474 (12AM-2PM and 8PM-12AM)	9.11	—
El Paso	EL PASO ELECTRIC COMPANY SCHEDULE NO. 24 [64]	0.11861 (12-6PM)	—	0.00502 (12AM-12PM and 6PM-12AM)	—	24.50
New York	Orange and Rockland Utilities Time of Use [65]	0.32012 (12-7PM)	0.1145 (10AM-12PM and 7-9PM)	0.02061 (12AM-10AM and 9PM-12AM)	—	—
Buffalo	Orange and Rockland Utilities Time of Use [65]	0.32012 (12-7PM)	0.1145 (10AM-12PM and 7-9PM)	0.02061 (12AM-10AM and 9PM-12AM)	—	—



a) b)

Figure 18**:** Seasonal a) on-peak electricity consumed by HVAC system and b) energy cost for the baseline and PCM-equipped cases in various cities

Table 5 presents the aggregated performance over the whole simulation period for all considered locations. Miami has the highest total cooling load due to high sensible and latent loads, which is typical for the hot-humid climate. For all cities, the total HVAC cooling load is increased when the PCM storage is deployed. This can be attributed to the increase in the supply airflow rate during the discharging period, which coincides with the hottest hours of summer days. As the supply airflow rate increases, more hot outside air is introduced because of the fixed outdoor air fraction assumed in the simulation study, which results in a higher ventilation load. Another key observation is that the average system COP is slightly lower in the PCM-equipped case than the baseline case for all locations except for Phoenix. This is because (1) the decrease in the COP during the PCM charging period outweighs the COP increase during the PCM discharging period and (2) the total load during the PCM charging period is higher due to the load shifting effect. The increased total cooling load and reduced system COP together lead to a high total HVAC electricity usage after the deployment of the PCM storage, for all locations. This represents a round-trip

efficiency loss associated with the proposed PCM storage solution. Despite using more electrical energy overall, the PCM storage reduces the electricity cost for all cities because the consumption is shifted from the high-price hours to the off-peak hours with lower electricity prices. The seasonal electricity cost savings ranges from 11% (Miami) to 15.8% (Buffalo).

Table 5: Cooling season total energy consumption and electricity cost

	Miami		**Phoenix**		**El Paso**		**New York**		**Buffalo**	
	Base	**PCM**	**Base**	**PCM**	**Base**	**PCM**	**Base**	**PCM**	**Base**	**PCM**
HVAC Total Load (GJ)	880	938	799	859	607	654	629	678	455	486
Total Electric Energy (MWh)	54.3	60.1	64.9	70.1	38.7	42.2	33.3	38.1	21.6	23.9
System COP	4.5	4.3	3.4	3.4	4.4	4.3	5.2	4.9	5.9	5.6
Total PCM (kg)	—	2418	—	2210	—	1926	—	2017	—	2057
Total Electricity Cost ($)	4940	4401	11337	9570	7227	6151	5224	4498	3736	3145
On-Peak Electric Energy (MWh)	22.6	17.5	21.7	14.9	16.3	11.6	13.3	10.0	9.7	7.3

2.6.3 Economic Analysis

To evaluate the financial feasibility of the PCM storage solution, simple payback period, loan repayment period and net present value (*NPV*) analyses were performed based on estimated costs of the PCM TES and the predicted electricity cost savings. The payback period was calculated as follows:

$$Payback\ period\ = \frac{Cost\ of\ PCM}{Annual\ Cooling\ Season\ Electricity\ Cost\ Reduction} \tag{23}$$

The loan repayment period was calculated as follows:

$$Repayment\ period\ = -\log_{[1+r]}\left[1-\frac{r(PV)}{P}\right] \tag{24}$$

where r is the interest rate, PV is the loan amount (PCM cost), and P is payment amount (cooling season savings). The repayment period was calculated assuming an annual interest rate of 10%. The *NPV* was calculated as follows:

$$NPV = \sum_{i=0}^{y} \frac{CF}{(1+x)^i} \tag{25}$$

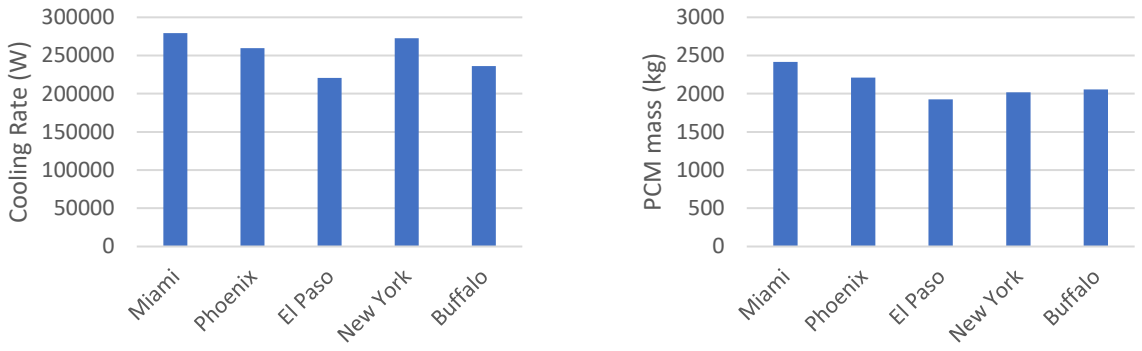
where CF is the net cash flow at year i, y is the investment period in years, and x is the discount rate, which is assumed to be equal to the assumed annual interest rate of 10%. A 15-year investment period was considered, which coincides with the expected lifespan of an HVAC system. At year 0, CF is the initial investment (PCM cost), which is considered negative cash flow, and in subsequent years, CF is the cooling season electricity cost savings. A positive *NPV* suggests that the investment is worthwhile because the present value of the future cash flows within the

investment period is greater than the initial investment. The cost of the storage unit was assumed to be $2 per kg of PCM [66], which includes the casing material cost and the labor cost. The investment feasibility metrics for each location are displayed in Table 6. Phoenix is the most financially viable location to implement the PCM TES solution with the lowest payback and loan repayment periods (7.5 cooling months and 2.6 cooling seasons, respectively) and highest *NPV* ($9020) among all five locations. This is due to the high (absolute) energy cost savings in Phoenix compared to the other cities. Miami has the longest payback and loan repayment periods (26.9 cooling months and 10.3 cooling seasons, respectively) and lowest *NPV* ($-736) because it has significantly lower energy cost savings and the highest PCM cost. Despite having the second highest (absolute) on-peak energy reduction, Miami has a small peak-to-off-peak rate ratio and much lower electricity price overall, which results in the lowest cost savings potential. Buffalo has a larger PCM size and cost, but longer payback period than New York. This suggests that the PCM storage is slightly undersized for New York. Figure 19 displays the nominal cooling capacity of the HVAC system in each location determined by EnergyPlus and the PCM mass for each location determined using Equation (21). The overall trends of the HVAC and PCM sizes match across the locations except for New York, which has the second largest HVAC size but the fourth largest PCM size. The outlier can be due to the different sizing strategies for the HVAC equipment and PCM storage: EnergyPlus uses the 0.4 percentile of the annual weather data (the hottest 35 hours of the whole year) to size the HVAC system, while the PCM storage is sized to reduce the on-peak electricity usage of the hottest day. The current PCM sizing strategy was derived based on trial simulation tests and could be very sub-optimal. Also, it may be noted that the loan repayment period is expressed in cooling months, because it is very common to have mechanical cooling all year round for commercial buildings. In winter or colder months, air-side economizing can be used

to significantly reduce the mechanical cooling demand and deployment of the proposed PCM energy storage could provide even greater performance gains by mitigating the misalignment between the cooling load (daytime) and availability of "free" cooling resource (nighttime). However, this would require more sophisticated control strategies. That is why only the cooling season is considered for the payback analysis.

Table 6: Economic analysis results for the proposed PCM solution in the candidate cities

City	PCM Cost ($)	Payback period (Cooling months)	Loan Repayment Period (Cooling months)	NPV after 15 years ($)
Miami	4836	26.9	30.9	-736
Phoenix	4420	7.5	7.8	9020
El Paso	3852	10.7	11.4	4332
New York	4034	16.7	18.3	1488
Buffalo	4114	20.9	23.1	381



a) b)

Figure 19: a) Nominal cooling capacity determined by EnergyPlus and b) total PCM mass in various cities

2.7 Concluding Remarks

This chapter presents a PCM-based energy storage solution designed for installations in supply-air ducts to enhance building power flexibility and a comprehensive assessment of the proposed solution in terms of energy consumption, energy cost savings, load shifting capability, and peak electric demand reduction potential. A numerical model for the in-duct PCM storage was formulated and calibrated using experimental data collected from a PCM panel prototype. The model was linked with the EnergyPlus medium office prototypical building models through FMU and with a calibrated variable-speed cooling system model, to establish a simulation test bed that allows whole-building simulation-based assessment of the proposed PCM storage. A simple rule-based control strategy was proposed and tested, which enables the PCM charging by applying a lower SAT setpoint prior to the on-peak hours and activates the PCM discharging process by raising the SAT during the on-peak period to reduce the peak electrical demand. Parametric simulations were carried out covering five different climate locations over a 3-month cooling

season. Simulation test results showed that the proposed in-duct PCM storage solution is effective in shifting both the sensible and latent cooling loads from on-peak to off-peak hours, resulting in on-peak HVAC electricity consumption reductions of up to 31.5%. Load shifting through the PCM storage is achieved at the cost of increased total HVAC electricity usage, by up to 14.4%, partially attributed to the high ventilation load during the discharging period. However, under TOU rate schedules, load shifting enabled by the PCM storage can provide economic benefits with seasonal electricity cost savings from 11% to 16%. The peak demand reduction and electricity cost savings potentials are highest for Phoenix, due to the high SHR and perfect alignment of the PCM discharging and the on-peak periods. An economic analysis has shown that the simple payback periods of the proposed PCM storage solution range from 7.5 to 26.9 cooling months. Miami has the longest loan repayment period and is the only location involving a negative *NPV* because of the cheap electricity and the large amount of PCM used.

The results presented in this chapter provide conservative estimates of the potentials of the proposed in-duct PCM storage solution in peak demand and electricity cost reductions. This study considered a simple rule-based control strategy for charging/discharging the PCM storage, which can be sub-optimal. Control optimization along with optimal sizing of the PCM storage and coordination with the air-side economizer operations can significantly enhance the overall system performance. In addition, the PCM charging/discharging control can be combined with optimized zone temperature scheduling to fully utilize the energy storage capacity in buildings and to unlock the “free cooling” potential.

3. Full Scale PCM TES Prototype Development

The previous chapter presented co-simulation results for PCM that is encapsulated in an aluminum box and mounted on the interior surface of the supply duct wall. While the proposed PCM TES solution demonstrated the potential to perform load shifting and peak electric demand reduction, it still does not present a feasible retrofit solution due to the length of the duct required and the PCM panel mounting strategy. This chapter will present an alternative PCM TES module design and prototype that aims to improve the retrofit capabilities of the in-duct PCM TES.

3.1 In-Duct PCM Storage Module Prototype

Figure 20 displays the fabricated prototype of the in-duct PCM TES module. The prototype consists of PCM Panels and a rack to hold the panels vertically and parallel to the air flow direction. The PCM Panels were fabricated by attaching two PCM bags on either side of an aluminum sheet and securing them along the edges using acrylic strips and aluminum rivets. The PCM bag consists of 8 rows of PCM pouches, which prevent excessive sagging due to the accumulation of liquid PCM at the bottom and helps to maintain a consistent bag thickness. The PCM pouches were made using a vacuum sealer and 15” store-bought food saver bags. First, the liquid PCM was measured using a measuring cylinder, and then poured into a 3-D printed mold, which was placed in a freezer to solidify. Once solidified, the PCM was encapsulated in the food saver bags using a vacuum sealer to minimize the amount of air in the PCM bag. Each bag contains approximately 800 ml of liquid PCM. A total of 20 bags were used in the presented prototype, which amounted to 13.76 kg of PCM. The PCM module rack was fabricated by connecting a base consisting of aluminum square tubes and a top made from aluminum U-channels using threaded rods. Slots were carved into the PCM frame to allow the PCM panels to slide in and out of the rack. The PCM used in the

experiment was PureTemp 15, which is a biobased PCM with a nominal melting point of 15˚C [58].



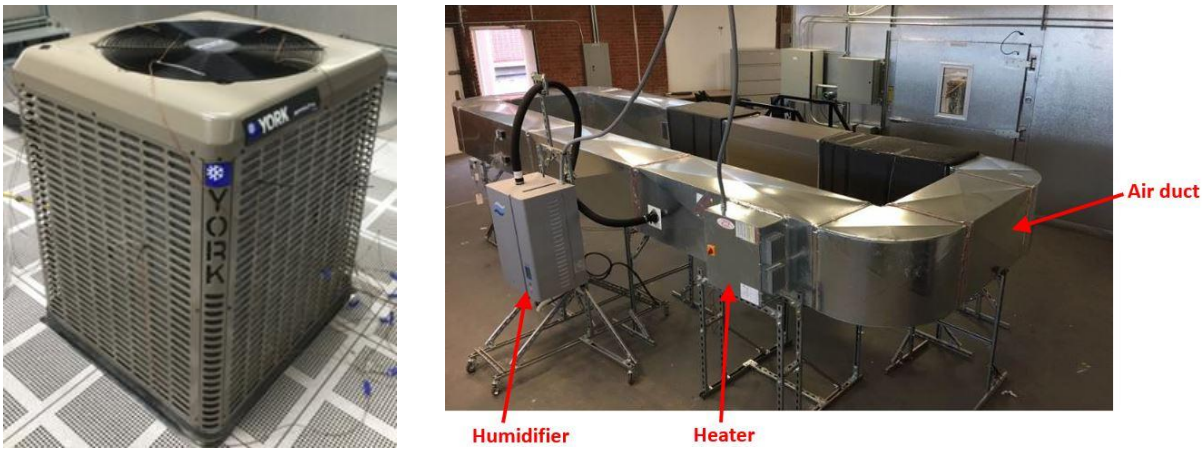
Figure 20: PCM TES prototype

3.2 Experimental Evaluation

3.2.1 Experimental Methodology

To evaluate the thermal performance of the PCM TES Module prototype, it was subjected to a freezing and melting cycle. Figure 21 shows the experimental test rig, which consists of a 3-ton R410A variable speed split direct expansion system. The indoor unit contains an A-shaped evaporator coil, an electronically commutated motor-driven supply fan and an EEV for AC operation. The indoor unit is housed in an indoor environment test loop that comprises supply and return air temperature grids, an electric resistive heater to replicate building internal heat gains and a thermal dispersion airflow transducer. The PCM TES module was placed downstream of the supply air temperature grid, and a post-PCM temperature grid was installed. Each temperature grid

consists of 5 T-Type thermocouples and an air relative humidity sensor. The duct section housing the PCM was externally insulated using 2” thick AP/ArmaFlex R8 insulation. The outdoor unit comprises a variable-speed compressor, a condenser coil, a condenser fan, a reversing valve, a suction accumulator, a charge compensator and an EEV for HP operation. The outdoor unit is housed in a psychrometric chamber which is used to reproduce desired outdoor dry-bulb temperature conditions.



a) b)

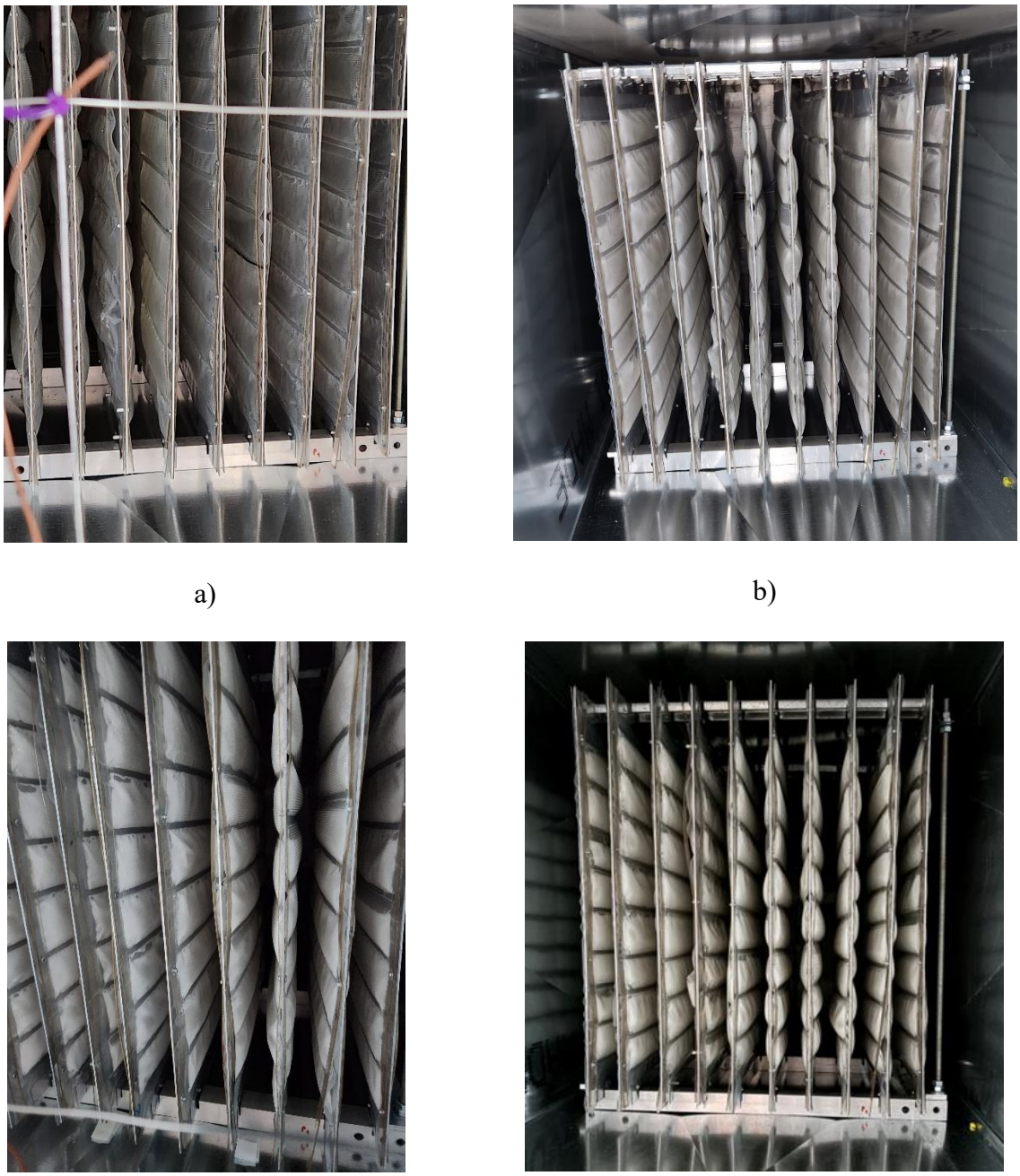
Figure 21: Experimental test rig consisting of a) outdoor unit in a psychrometric chamber and b) indoor environment test loop

The experiment was conducted in two stages: the first stage consisted of solidifying the PCM that was initially in the liquid phase, and the second stage consisted of melting the PCM directly after the first stage. During the first stage, the target supply-air temperature was set at 8 °C, and the airflow rate was set to 1000 CFM. During the second stage, the supply-air temperature was set to 18 °C, and the airflow rate was set to 1200 CFM, which is the nominal airflow rate, to increase cooling rate to a comparable value as the first stage

A second test was performed to evaluate the static pressure difference across the PCM TES module at varying airflow rates. The supply airflow rate was varied between 400-1200 CFM and the static pressure difference was measured using a TSI 9565-P VelociCalc Ventilation Meter.

3.2.2 Results and Discussion

Figure 22 displays the PCM TES module inside the duct during the experimental test. At the beginning of the freezing period (see Figure 22a), the PCM is in liquid phase and has a clear color. Once the freezing process begins, the PCM became opaque as the solid fraction of the PCM began forming at the PCM-bag material boundary. Between Figure 22b and Figure 22c, the PCM color remained opaque, but was increasingly whiter and firmer, which indicated that more of the liquid PCM was freezing. The freezing period was terminated once the PCM was a white color and firm to the touch (see Figure 22d). Once the freezing process was complete, the melting period was initiated. Figure 23 displays the progression of the melting process, which was easier to observe due to the contrast between the clear liquid PCM and white solid PCM chunks. As the melting period advanced, the solid chunks became smaller until the pouches only consisted of clear liquid, at which point the melting process was complete.



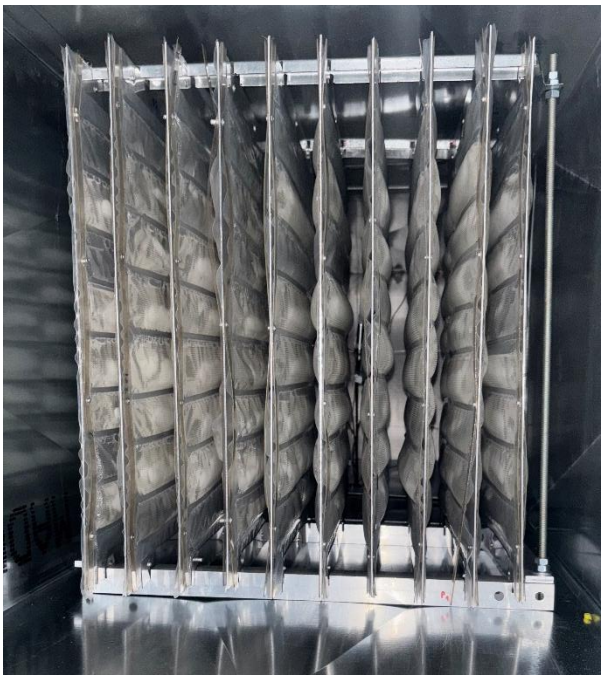
a) b)

c) d)

Figure 22: Progression of PCM freezing at various stage - a) initial state, b) ~1 hour, c) ~2.5 hours and d) end of freeze period (~3 hours)



22300 ~ 1 hour



23900 ~2 hours



c) ~2.5 hours



d) ~3 hours

Figure 23: Progression of PCM melting at various stages - a) ~1 hour, b) ~2 hours, c) ~2.5 hours and d) end of melt period (~3 hours)

Table 7 displays the static pressure rise across the PCM TES at different airflow rates. The increase in static pressure across the PCM TES module is expected because it acts as a partial blockage in the supply air duct and increases the air resistance that the supply fan must overcome. This will lead to an increase in the fan power consumption because it has to perform more work to maintain the desired supply airflow rate. Consequently, the system COP will decrease because the total HVAC electric power consumption will increase.

Table 7: Static pressure rise across the PCM TES at different airflow rates

Supply Airflow Rate (CFM)	**Static Pressure Rise (in. H_20)**
400	0.009
600	0.012
800	0.013
900	0.015
1000	0.018
1200	0.022

3.3 Comparison of Wall Mounted and PCM in Rack TES solutions

The PCM TES sizing strategy employed in Chapter 2.5 resulted in a square duct size of 34”×34” and PCM duct section length of approximately 29.6 m to mount 2210 kg of PCM for the Phoenix location. This may prove to be challenging to implement because of the space limitations in buildings. The PCM in rack prototype presented in this chapter was designed to fit in a 20”×20” square duct and occupied a duct length of 0.381 m (15”), which results PCM capacity of 36.1 kg/m of duct length. When scaled to fit the cross-sectional area of the 34”×34” duct, the PCM capacity

becomes 104.3 kg/m. Therefore, the duct section needed to house 2210 kg of PCM is approximately 21.2 m, which is an improvement of 8.4 m. The rack mounted design also allows for easier PCM TES deployment, customization and decommissioning. The rack can be mounted onto wheels to allow for ease of installation and removal from an open section of ductwork. Whereas the wall mounted design would require the removal of the whole duct section.

3.4 Concluding Remarks

This chapter presented a PCM TES solution consisting of PCM plastic bags attached to an aluminum sheet and mounted in a rack parallel to the airflow direction. The module was subject to a freezing and melting cycle, which were both completed within 3 hours. The rack-mounted PCM TES improved on the wall-mounted design by decreasing the length of duct required for the sizing strategy presented in Chapter 2.5. However, it led to an increase in static pressure, which will increase the fan power consumption and lead to a lower system COP.

4. Model-Based Predictive Control of Multi-Stage Air-Source Heat Pumps Integrated with Phase Change Material-Embedded Ceilings[2]

The previous chapters presented the potential benefits of active PCM TES when deployed in the supply-air duct and charged/discharged using the SAT in coordination with TOU electric rate schedules to shift the cooling load and peak demand power from on peak to off peak hours. However, a rule-based control strategy was employed, which may lead to suboptimal system coordination. This chapter presents a model-based predictive control (MPC) strategy to optimize the operations of phase change material (PCM) ceiling panels coupled with a multi-stage air-source heat pump. Despite the different applications of active PCM TES in HVAC systems, this study provides valuable insight into the potential of such systems.

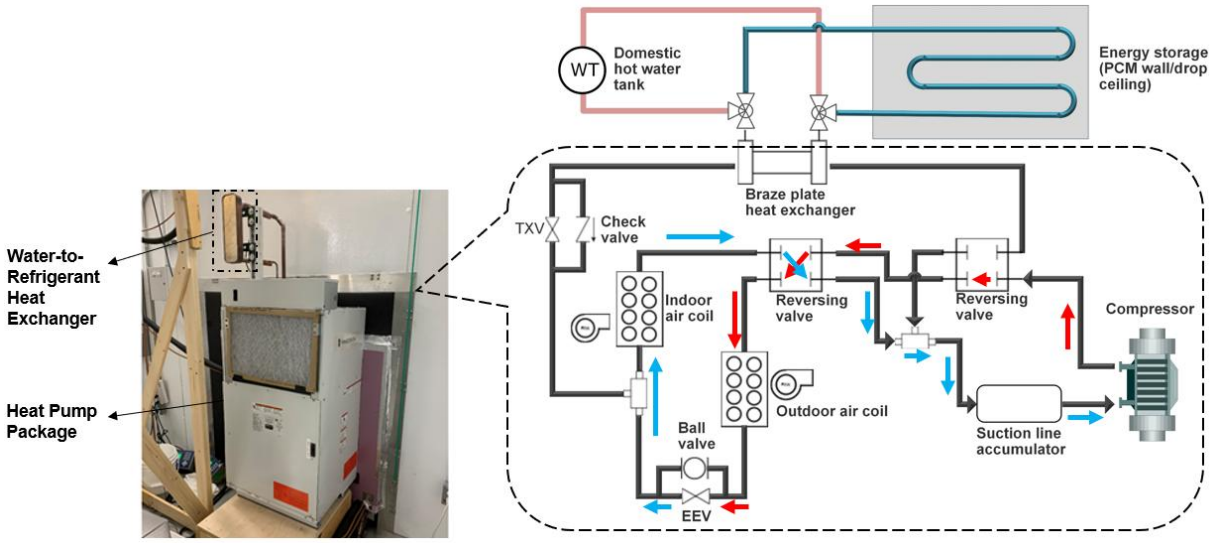
4.1 Integrated Air-Source Heat Pump System Description

Figure 24 (right hand side) shows a schematic diagram of the ASIHP system under study, which is comprised of a reversible air-source heat pump, a PCM charging loop and PCM ceiling panels. The system offers four operation modes, i.e., space cooling (SC), space heating (SH), PCM heat charging and PCM cold charging. Multiple reversing and three-way valves work together to achieve mode switching. During the SC mode, the heat pump operates as an air conditioner, pumping heat from the indoor space to the ambient environment. During the SH mode, the heat pump operates with a reversed refrigerant circuit that extracts heat from the ambient environment and dumps it to the indoor space. Under the PCM cold charging mode, the refrigerant bypasses the indoor coil and instead is routed to a plate heat exchanger (evaporator) where the process water is cooled down; the chilled water runs to the PCM ceiling panels to charge the “cold” energy by solidifying the PCM through a plastic heat exchanger. The refrigerant flow for the SC and PCM

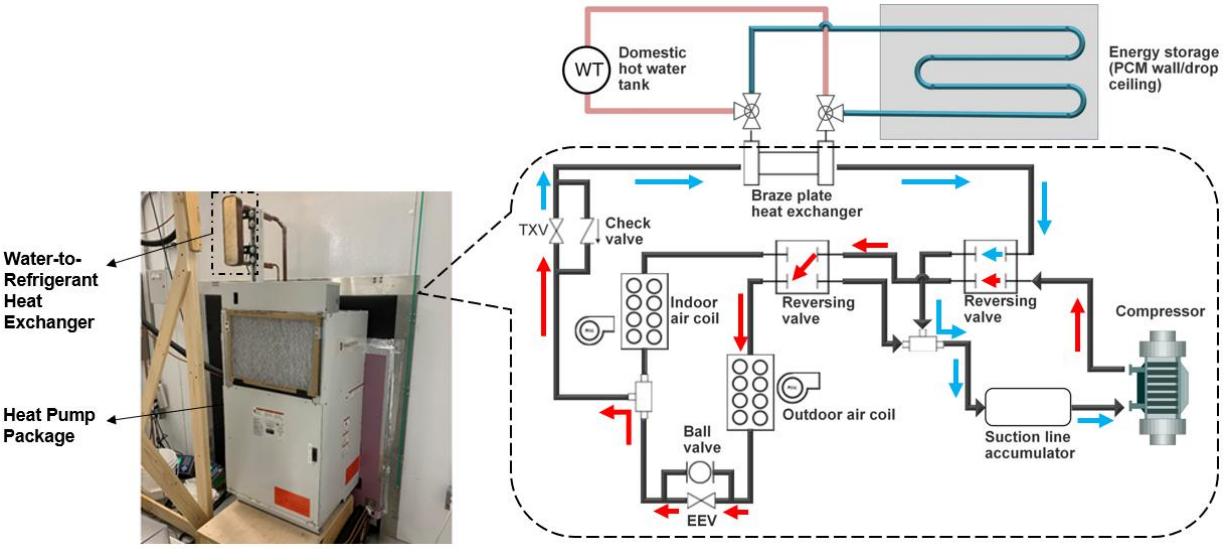
[2] The contents of this chapter have been previously published in Hlanze *et al.* [79]

cold charging modes are shown in Figure 24, where the red and blue arrows signify the high and low refrigerant pressure, respectively. In the PCM heat charging mode, the plate heat exchanger becomes a condenser which generates heat delivered to the PCM. Heat is transferred between the PCM and indoor air driven by the temperature difference. During the SC and SH modes, the PCM process water loop is off. The ASIHP also includes a water heating functionality where domestic hot water is heated using the heat pumped from the indoor space during a combined space cooling and water heating mode or pumped from the ambient during a dedicated heat pump water heating mode. However, the domestic water heating capability of the ASIHP system is not studied here as the case study building involves relatively low water heating energy usage.

The left-hand side of Figure 24 displays the laboratory prototype of the ASIHP, which was located in the Oakridge National Laboratory testing facilities. The compressor in the prototype was a 2-ton scroll compressor with three stages: low, medium and high. For the SC mode, only the low and medium stages are allowed while the high stage is reserved for the PCM charging mode. The SH mode can run at all three stages. The indoor blower has a brushless direct current motor and back-curved impeller. The outdoor fan is a single-speed fan having axial flow.



a)



b)

Figure 24: ASIHP schematic diagram and the prototype unit in the laboratory—a) SC mode and b) PCM charging mode

4.2 Simulation Test Bed

To facilitate performance assessment, a simulation test bed was constructed based on the co-simulation of (i) a numerical model of the PCM-embedded ceiling, (ii) the ASIHP system model, and (iii) the U.S. Department of Energy (DOE) prototypical single family detached house building model for Atlanta, GA [67]. The ASIHP model incorporates performance curves derived from the high-fidelity Heat Pump Design Model developed by Oak Ridge National Laboratory [68] and is publicly available through EnergyPlus component library. The performance curves used in the ASIHP model have been calibrated using performance data collected in the laboratory (see Section 4.2.4 for the calibration results). The MPC module, which makes use of the PCM model, a resistance-capacitance (RC) thermal network model for the building envelope and an ASIHP control model, is implemented in Python, while the high-fidelity DOE prototypical model and the nonlinear ASIHP model run in EnergyPlus, which serves as a simulation test bed. Note that the same PCM model is used for the controller and the simulation test bed, while different control and plant models are utilized for the building envelope and ASIHP system. Due to model mismatch, the initial states of the RC network model need to be estimated at each MPC decision step using state observing techniques. The overall simulation test bed packages the disparate component models, and co-simulation is achieved through FMI [51].

4.2.1 Co-Simulation Platform with EnergyPlus and Python

The whole building energy simulation test bed incorporates a co-simulation platform of EnergyPlus and Python based on the FMI standard [51] An EnergyPlus Functional Mock-up Unit (FMU) has been created for the DOE prototypical single family detached house building model. The space heating and cooling equipment models in the original DOE prototypical model were replaced with the ASIHP model in the EnergyPlus FMU, which is linked to the PCM model with

the interfacing variables shown in Figure 25. The PCM model accepts the zone air temperature (ZAT) generated by the EnergyPlus FMU and uses it as a boundary condition to calculate the PCM-to-room heat transfer rate. The resulting heat transfer rate is accepted by the EnergyPlus FMU and this thermal interaction is modeled using two "Other Equipment" objects—the first object outputs a negative heat transfer rate to simulate the PCM cooling effect, and the second object outputs a positive heat transfer rate to simulate PCM heating the room. The ZAT simulated by the EnergyPlus FMU is fed to a Kalman filter-based state observer which outputs the estimated states (nodal temperatures) of the RC thermal network at the current time step; the latter are used by the MPC module to predict the thermal dynamic response of the building in the next 24 hours, using the forecasted weather and electricity price signals. Perfect forecasts are assumed, so the performance reported in this study represents the theoretical upper bound and the actual performance in real-world implementations may be slightly worse due to weather prediction uncertainties. The building load prediction is achieved by integrating all the component-level control models together, and optimal control schedules for the ZAT and PCM charging rate that minimize the predicted electricity cost in the look-ahead time horizon are identified. Only the control actions of the first time step are applied and when the next decision time arrives, the control decision making process is repeated in a receding horizon scheme. An FMI master program was implemented in Python, which manages the progression of simulation time and communications between the PCM model, the MPC module and EnergyPlus. In the co-simulation, the interface variables are updated at each time step (1 hour) in a ping-pong scheme.

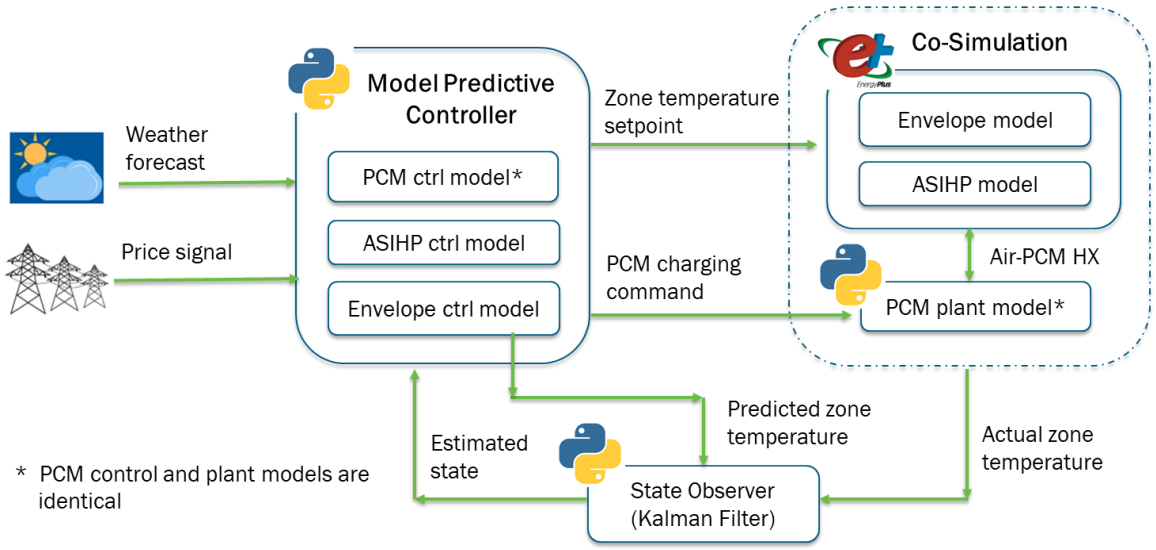


Figure 25: Schematic diagram of the EnergyPlus-Python co-simulation platform

4.2.2 PCM Model

The PCM model is adapted from Chapter 2.3.1. The thermal conductivity of the solid and liquid phases is assumed to be equal ($k_s = k_l = k$) for simplicity. Thus, Equation (4) becomes

$$h_j^{t+1} = \frac{\Delta t \cdot k \cdot \left(T_{j+1}^{t+1} - 2T_j^{t+1} + T_{j-1}^{t+1}\right)}{\rho(\Delta x)^2} + h_j^t \tag{26}$$

The PCM is installed in the drop ceiling and has two boundary thermal interactions—PCM-to-chilled water and PCM-to-air heat transfers. Once the enthalpy at each control volume is determined, the temperature can be found using

$$T_j^{t+1} = \begin{cases} (T_m - 0.1) + \dfrac{h_j^{t+1}}{c_p}, & h_j^{t+1} \le 0 \\ (T_m - 0.1) + \dfrac{0.2}{h_{sl}} \cdot h_j^{t+1}, & 0 \le h_j^{t+1} \le h_{sl} \\ (T_m - 0.1) + \dfrac{h_j^{t+1} - h_{sl}}{c_p}, & h_j^{t+1} \ge h_{sl} \end{cases} \tag{27}$$

where T_m is the PCM melting temperature, and c_p is the specific heat of the PCM (assumed to be identical for liquid and solid phases). To ensure a one-to-one mapping of the temperature-enthalpy relationship, a small temperature band (0.2°C) is introduced for the phase change process.

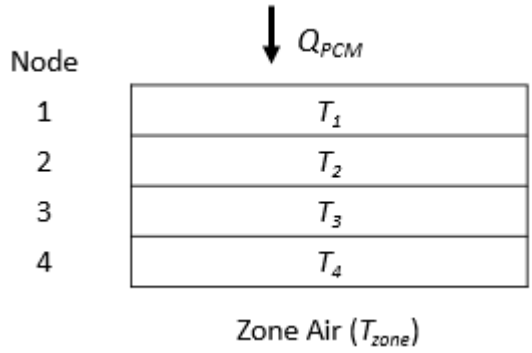


Figure 26: PCM finite control volume schematic

The outermost control volume interacts with the chilled water. An implicit formulation of the dynamics of the first nodal temperature is

$$h_1^{t+1} = \frac{\Delta t}{m_{PCM}}\left(Q_{PCM}^{t+1} - \frac{k(T_1^{t+1} - T_2^{t+1})}{\Delta x}\right) + h_1^t \tag{28}$$

where m_{PCM} is the PCM mass of the specific control volume and Q_{PCM} is the PCM charging rate provided by the chilled water circuit. The innermost control volume interacts with the zone air, and its dynamics are governed by

$$h_4^{t+1} = \frac{\Delta t}{m_{PCM}}\left(\frac{k(T_3^{t+1} - T_4^{t+1})}{\Delta x} - Q_{SC,PCM}\right) + h_4^t \tag{29}$$

where $Q_{SC,PCM}$ is the PCM-to-room air heat transfer. The PCM-to-room air heat transfer is a natural convection interaction characterized by

$$Q_{SC,PCM} = \frac{T_4^{t+1} - T_{zone}^{t+1}}{\frac{1}{UA} + \frac{\Delta x/2}{kA}} \quad (30)$$

where T_{zone} is the ZAT, A is the PCM surface area, and U is the convective heat transfer coefficient between the PCM and zone air. The calculation of U is performed as follows:

$$U = 2.42 \frac{\left|T_{4,nom} - T_{zone,nom}\right|^{0.31}}{D_e^{0.08}} \quad (31)$$

where D_e is the equivalent diameter of the PCM panel (4 × area/perimeter) [69], $T_{4,nom}$ and $T_{zone,nom}$ are the nominal temperatures of the innermost node and indoor space, assuming 19.7°C and 23°C, respectively. The nominal temperatures are used in the calculation of the convention heat transfer coefficient to reduce chattering across consecutive simulation time steps; when smaller time steps are used, the actual nodal and zone temperatures can be employed. In the case study, the PCM was assigned a melting temperature of 19.7°C and a thickness of 5 mm. The PCM ceiling was assumed to cover 75% of the floor area of the prototypical residential home (167.25 m^2) with a total latent heat capacity of 131 MJ (36.4 kWh).

4.2.3 Building Envelope Thermal Network Model

To facilitate prediction of the building load variation, an RC thermal network model was developed that captures the major dynamics of the DOE prototypical single family detached house. Figure 27 presents the structure of the RC thermal network adopted in this study, which is a two-zone model predicting the variations of the living space and attic temperatures for given boundary conditions. Two wall branches are included, one for the external wall and the other for the roof, to capture the slow heat conduction between the ambient and indoor spaces, while a single-resistance branch is

used to model fast thermal couplings, such as heat loss through windows and infiltration. An internal wall branch is present that characterizes additional thermal mass associated with internal walls and furniture. Applying energy balances to the temperature nodes and after time discretization, the following linear time-invariant state-space formulation can be obtained

$$\boldsymbol{x}^{t+1} = \boldsymbol{A}\boldsymbol{x}^{t} + \boldsymbol{B}_{w}\boldsymbol{w}^{t} + \boldsymbol{B}_{u}Q_{z}^{t} \tag{32}$$

$$T_{zone}^{t+1} = \boldsymbol{C}\boldsymbol{x}^{t+1} \tag{33}$$

where $\boldsymbol{x}$ is the state vector containing all nodal temperatures of the thermal network, and $\boldsymbol{w}^{t}$ is the disturbance vector comprised of outdoor temperature, internal loads and solar radiation effect. The state-space matrices $\boldsymbol{A}, \boldsymbol{B}_{w}, \boldsymbol{B}_{u}$ and $\boldsymbol{C}$ are dependent on the thermal resistances and capacitances of the thermal network. The model input is the average zone cooling rate (Q_{z}^{t}) within each step, which is a sum of the cooling effects associated with the DX space cooling and PCM cooling:

$$Q_{z}^{t} = SHR_{SC} \cdot Q_{SC}^{t} + Q_{SC,PCM}^{t} \tag{34}$$

where SHR_{SC} and Q_{SC} are the sensible heat ratio and zone cooling rate associated with the space cooling (SC) mode. The model was trained offline using EnergyPlus simulation results over a summer month. The training data was collected by imposing a pseudo-random binary sequence for the indoor temperature setpoint to ensure persistent excitation of the system. A robust model identification algorithm developed by the Cai and Braun [70] was used in estimating the thermal parameters. Figure 28 shows the predicted cooling load profiles with the identified thermal network model in comparison with the EnergyPlus simulation results. The surrogate RC network

model agrees well with the high-fidelity EnergyPlus model. Note that the RC network model is only used for control decision making while the simulation test bed still relies on EnergyPlus.

To ensure indoor comfort, the zone cooling rate that is provided to the indoor space is needed to keep the indoor temperature within a comfortable range, i.e.

$$T_{lower}^{t} \leq T_{zone}^{t} \leq T_{upper}^{t} \tag{35}$$

where T_{lower}^{t} and T_{upper}^{t} denote the lower and upper temperature bounds.

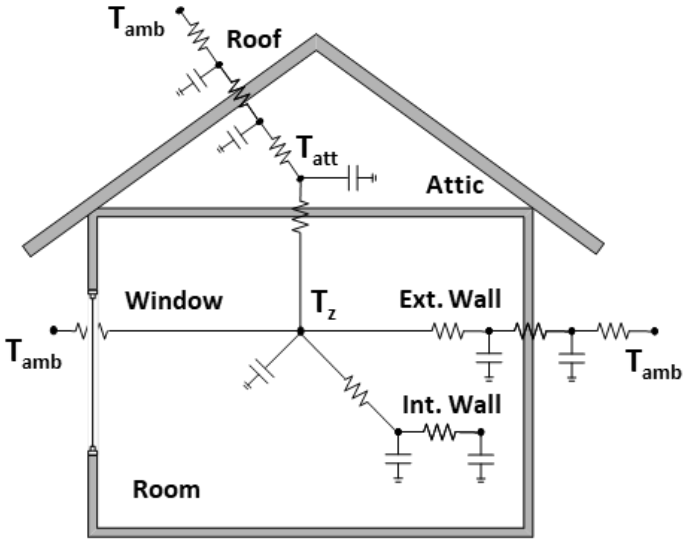


Figure 27: Building RC thermal network diagram

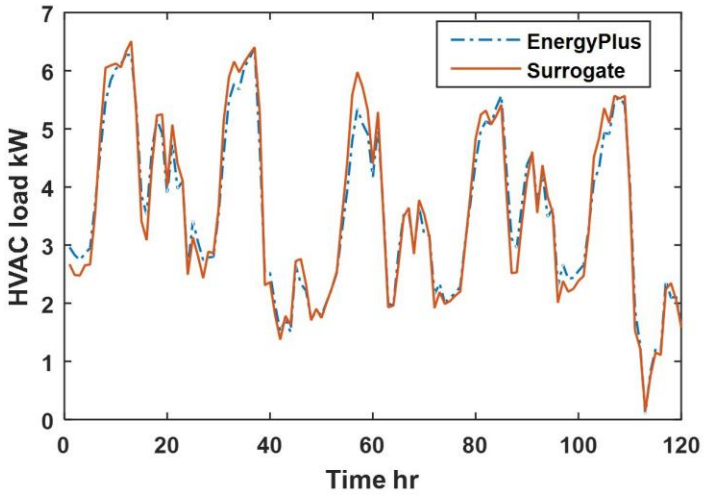


Figure 28: Thermal network model validation results for cooling load prediction

4.2.4 ASIHP Model

DX SC mode

The DX space cooling mode is simulated using the ASIHP model in EnergyPlus [71]. In this study, the water heating function in ASIHP was disabled. The performance curves for the space cooling mode were modified based on the performance data collected from the prototype unit at Oakridge National Laboratories. Within the ASIHP model, the space cooling function is modeled as a variable-speed air-source heat pump. Performance curves for two speeds were implemented in the model, capturing the low- and medium-stage cooling characteristics. For each stage, the cooling capacity ($Q_{cap,SC}$) is calculated using a quadratic correlation with respect to the evaporator inlet air wet-bulb temperature ($T_{RA,wb}$) and the outdoor air temperature (T_{OA}) in the following form:

$$Q^{t}_{cap,SC,S_i} = Q_{cap,rated,SC,S_i} \cdot \text{QCurve}_{cap,SC,S_i}\left(T^{t}_{OA}, T^{t}_{RA,wb}\right) \tag{36}$$

where S_i indicates the compressor stage (1 for the low stage and 2 for medium stage), $Q_{cap,rated,SC}$ is the rated cooling capacity, and QCurve is the quadratic correlation for the correction factor in the form

$$\begin{aligned}\mathrm{QCurve}_{cap,SC,S_i}\left(T_{OA}^{t}, T_{RA,wb}^{t}\right) &= E_1 + E_2 T_{RA,wb}^{t} + E_3\left(T_{RA,wb}^{t}\right)^2 + E_4 T_{OA}^{t} + E_5 (T_{OA}^{t})^2 \\ &+ E_6 T_{OA}^{t} T_{RA,wb}^{t}\end{aligned} \quad (37)$$

The QCurve coefficients are displayed in Table 8. The energy input ratio (EIR) for each stage is calculated using the same mathematical form but with different correlation coefficients. From the estimated cooling capacity and EIR, the compressor power can be obtained. The sensible heat ratio (SHR) is calculated using the bypass factor method, the default model in EnergyPlus [72]. When the cooling load is lower than the low-stage capacity, the compressor cycles between the "off" and low stages and the cyclic efficiency degradation is captured by the part load fraction correlation. When the compressor cycles between the low and medium stages, the compressor power is obtained through interpolation based on the ratio of the load to the respective capacities, which assumes no efficiency degradation caused by the cyclic operation.

Table 8: QCurve coefficients for compressor stage 1 and 2

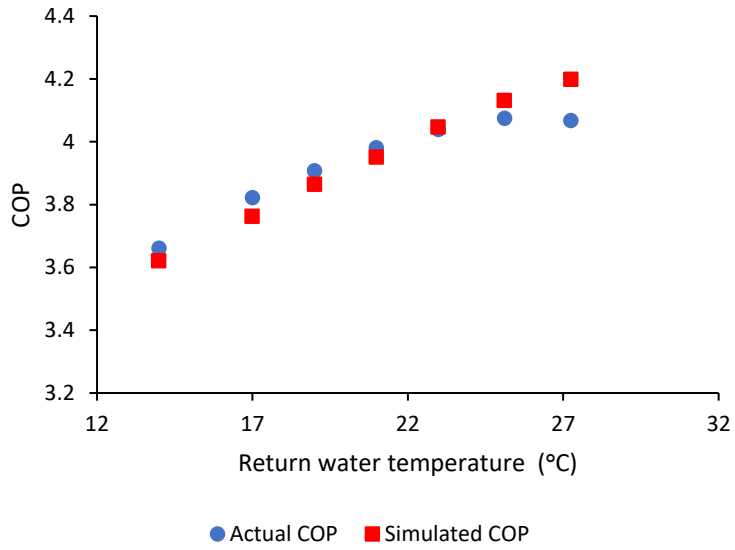
QCurve coefficient	Compressor Stage 1	Compressor Stage 2
E_1	0.6342361663	0.6344320109
E_2	0.0282779325	0.0287830331
E_3	0.0003814091	0.000343747
E_4	-0.0024160678	-0.0019846664
E_5	-0.0000359165	-0.0000468194
E_6	-0.0002894469	-0.0002859058

PCM charging mode

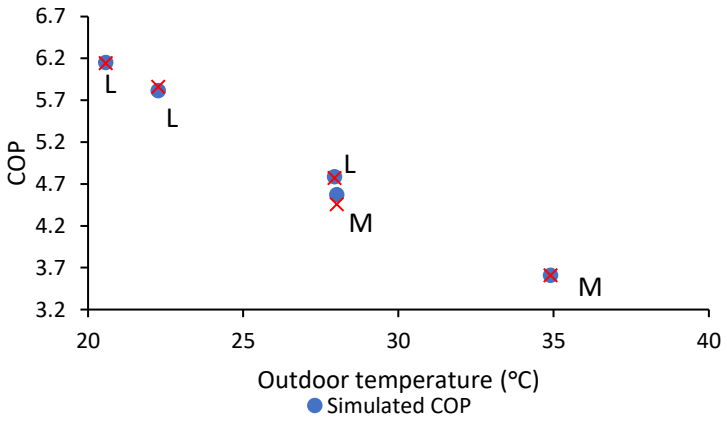
The high compressor stage is dedicated to the PCM charging mode, which is modeled as an air-cooled chiller. Since the ASIHP model in EnergyPlus does not support this operation mode yet, the PCM charging model is implemented in Python but follows the same model structure as shown in Equation(36). The major differences are: (1) the evaporator air inlet wet-bulb temperature is replaced by the return chilled water temperature from the water-to-PCM heat exchanger and (2) SHR is not relevant and thus not calculated. The water-to-PCM heat exchanger is assumed to have an effectiveness of unity and thus, the return water temperature is set to follow the PCM temperature of the node closest to the chilled water flow (node 1 shown in Figure 26). This is a reasonable assumption considering the large PCM ceiling area.

Figure 29 shows the ASIHP model validation results against the experimental data collected in the laboratory. The experimental test rig comprised of a three-stage scroll compressor with a rated capacity of 2-ton (7 kW) and three capacity levels (i.e., 100%, 67% and 45%). The indoor blower has a brushless direct current motor and back-curved impeller. An ASHRAE standard (ASHRAE Standard 37, 2019) code tester was used to measure the indoor air flow rate and air side capacity. The water side capacity was determined by measuring the inlet and outlet water temperature of the brazed plate heat exchanger and the water circulation flow rate. The indoor blower, outdoor fan and compressor power were each measured using power transducers. Power consumption of the water circulation pump was not considered. The PCM charging performance data was collected at a constant outdoor temperature of 23.5˚C while the return water temperature was gradually adjusted. During the tests, load was imposed using a resistive heater. The space cooling tests were

conducted with a return air dry-bulb of 26.7˚C and relative humidity of 50%. The calibrated model agrees well with the actual system performance and was used in all the simulation tests.



a)



b)

Figure 29: ASIHP model validation results for the PCM charging (top) and space cooling (bottom) modes

4.3 Control Strategies

This section describes the proposed MPC strategy for the PCM-integrated air-source heat pump system (referred to as MPC-PCM case). To evaluate performance gains that can be brought by the proposed control solution and the PCM TES integration, three benchmarking scenarios are considered and simulated, namely a baseline control strategy without PCM storage (BC), a rule-based controller for the PCM-integrated heat pump system (RBC), and a model predictive control strategy without PCM TES (MPC). The various strategies are discussed in the following subsections.

4.3.1 BC strategy

The BC case represents a scenario without the PCM ceiling where space cooling is purely reliant on the dual-stage air-source heat pump. The BC logic is simulated in EnergyPlus assuming perfect indoor temperature control, i.e., the compressor is staged to provide the exact cooling rate required to maintain the space temperature setpoint. A constant zone temperature setpoint of 23˚C is assumed throughout the whole day. Note that the BC case assumes the same heat pump characteristics but with the PCM charging mode disabled.

4.3.2 RBC strategy

In the RBC case, the PCM ceiling is present but the charging of it follows a fixed schedule, which is displayed in Table 9. This strategy was designed based on simple heuristics: the total PCM storage capacity (only accounting for the latent heat) was first calculated and then charging rates were estimated assuming a five-hour charging period. The schedule of charging rate shown in Table 9 was obtained through offline parametric analysis, which achieves the most significant cost reduction while satisfying all operation constraints. In the RBC strategy, the PCM charging is

enabled during the morning hours (7 AM to 12 PM) and the ASIHP is operated at a partial runtime that decreases over time to prevent the combined ASIHP runtime fraction surpassing 1, as the PCM charging mode is simulated outside EnergyPlus with the SC runtime fraction determined independently of the PCM charging schedule. The charging period is designed to end (12PM) two hours ahead of the on-peak period (2PM to 7PM) also to avoid simultaneous PCM charging and DX space cooling (see results in Section 4.4.2, the DX cooling is almost running full time 12PM to 2PM). In the RBC strategy, the same constant zone temperature setpoint of 23˚C is assumed. This RBC scenario captures the potential of the PCM TES integration through heuristically determined operation schedules.

Table 9: PCM charging runtime fraction schedule

Time	**PCM charging runtime fraction**
7AM-8AM	0.6
8AM-9AM	0.6
9AM-10AM	0.5
10AM-11AM	0.4
11AM-12PM	0.4

4.3.3 MPC-PCM strategy

The MPC-PCM strategy performs optimal scheduling of the ZAT and the PCM charging/discharging to achieve the maximum cost reduction by leveraging both the passive (building construction) and active (PCM) storage capacities of a building. The identified schedule tends to shape the PCM charge/discharge and space cooling load profiles in an optimal manner

based on the predicted load and operating conditions. At each decision step, the controller takes the predicted load and weather conditions (perfect prediction assumed) and identifies the optimal operation schedules for the look-ahead time horizon, e.g., 24 hours in the case study. Only the decisions of the first time step are applied and the control decision making process is repeated for the next decision time step in a receding horizon scheme. In the case study, the decision and simulation time steps are both assumed to be 1 hour. The objective functions, constraints and numerical solver of the MPC-PCM strategy are described in the following subsections.

Objective function

The control objective function is simply the total electricity cost that would be incurred by the control actions within the look-ahead time horizon:

$$min \sum_{t=t_0}^{t_f} r^t \cdot (P_{SC}^t + P_{PCM}^t) \tag{38}$$

where P_{SC}^t , P_{PCM}^t represent the compressor electric power consumption in the SC and PCM charging modes, respectively, r^t is the time-varying retail energy rate, t_0 is the current time step, and t_f is the final time step in the prediction horizon ($t_f = t_o + 24$). The set of time slots in the look-ahead horizon is defined as $\Gamma = \{t_o, \dots, t_f\}$. Note that this cost formulation only considers possible power uses during cooling seasons. A complete formulation considering all seasonal operations can be obtained by including a space heating mode. We consider a time-of-use (TOU) rate schedule in this study (Georgia Power TOU-REO-13 tariff schedule [73]). However, the strategy is flexible to accommodate other types of TOU rate schedules, e.g., tariffs with demand charges and tiered energy rates.

Multiple operation constraints need to be satisfied during control decision making, which are introduced and discussed next.

ASIHP system constraints

We introduce the runtime fraction to represent the runtime of different modes in each decision time step (1 hour), and the corresponding compressor power and cooling rate can be calculated as:

$$P_{SC}^{t} = R_{SC,S_1}^{t} P_{cap,SC,S_1}^{t} + R_{SC,S_2}^{t} P_{cap,SC,S_2}^{t} \tag{39}$$

$$Q_{SC}^{t} = R_{SC,S_1}^{t} Q_{cap,SC,S_1}^{t} + R_{SC,S_2}^{t} Q_{cap,SC,S_2}^{t} \tag{40}$$

$$P_{PCM}^{t} = R_{PCM}^{t} P_{cap,MPC}^{t} \tag{41}$$

$$Q_{PCM}^{t} = R_{PCM}^{t} Q_{cap,MPC}^{t} \tag{42}$$

$$0 \le R_{SC,S_1}^{t} + R_{SC,S_2}^{t} + R_{PCM}^{t} \le 1 \tag{43}$$

$$R_{SC,S_1}^{t}, R_{SC,S_2}^{t}, R_{PCM}^{t} \in [0,1] \tag{44}$$

where R_{SC,S_n}^{t}, $n \in \{1,2\}$ is the runtime fraction of the SC mode at compressor stage level n (stage 1 is the low stage and stage 2 is the medium stage), and R_{PCM}^{t} is the runtime fraction of the PCM charging mode. The total space cooling effect associated with the SC mode is the sum of cooling rates delivered during the low- and medium-stage operations. Note that in this control formulation, the part load efficiency degradation associated with cyclic operations between the "off" and low stages is neglected, i.e., the runtime fraction is equal to the part load ratio. This simplification does not cause much inaccuracy but can preserve linearity of the control model.

PCM thermal dynamic constraints

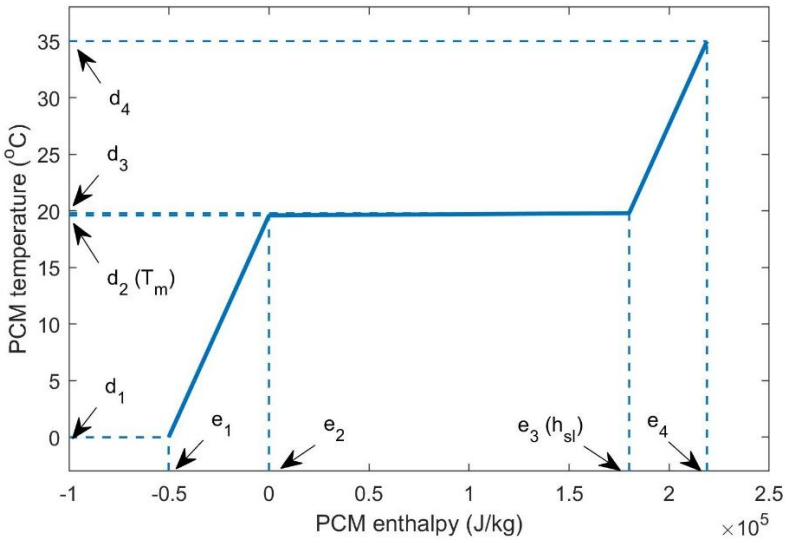


Figure 30: PCM temperature-enthalpy curve

The implicit finite control volume formulation of the PCM enthalpy dynamics given in Equation (26) is present in the control constraints for $j \in \{2, \ldots, N-1\}$ and $t \in \Gamma$. Additional PCM constraints include Equation (27) to characterize the algebraic relationship between the PCM enthalpy and temperature, which is piece-wise linear with three segments. A mixed-integer formulation of the enthalpy-temperature relationship is established by introducing two sets of auxiliary variables $\boldsymbol{\gamma} \in \mathbb{B}^3$ and $\boldsymbol{\lambda} \in \mathbb{R}_+^4$:

$$d_1\lambda_{j,1}^t + d_2\lambda_{j,2}^t + d_3\lambda_{j,3}^t + d_4\lambda_{j,4}^t = T_j^t \tag{45}$$

$$e_1\lambda_{j,1}^t + e_2\lambda_{j,2}^t + e_3\lambda_{j,3}^t + e_4\lambda_{j,4}^t = H_j^t \tag{46}$$

$$\lambda_{j,1}^t + \lambda_{j,2}^t + \lambda_{j,3}^t + \lambda_{j,4}^t = 1 \tag{47}$$

$$\lambda_{j,1}^t \leq \gamma_{j,1}^t \tag{48}$$

$$\lambda_{j,2}^t \leq \gamma_{j,2}^t + \gamma_{j,1}^t \tag{49}$$

$$\lambda_{j,3}^t \leq \gamma_{j,3}^t + \gamma_{j,2}^t \tag{50}$$

$$\lambda_{j,4}^t \leq \gamma_{j,3}^t \tag{51}$$

$$\gamma_{j,1}^{t} + \gamma_{j,2}^{t} + \gamma_{j,3}^{t} = 1 \tag{52}$$

$$\gamma_{j,i}^{t} \in \mathbb{B}, \forall i \in \{1,2,3\} \tag{53}$$

$$\lambda_{j,g}^{t} \geq 0, \forall g \in \{1, \dots, 4\} \tag{54}$$

where $\mathbf{d} = [d_1, d_2, d_3, d_4]^\top$ are the temperatures and $\mathbf{e} = [e_1, e_2, e_3, e_4]^\top$ indicate the enthalpies of the four endpoints of the enthalpy-temperature curve shown in Figure 30. If the enthalpy falls on the i-th segment, the corresponding entry of $\boldsymbol{\gamma}$ (i.e., $\gamma_{j,i}^{t}$) is 1; otherwise, $\gamma_{j,i}^{t}$ is equal to 0. Any given enthalpy/temperature in the considered range can be represented as a linear combination of the four endpoints where the coefficients are $\lambda_{j,g}^{t}$. To ensure a unique representation, only the coefficients corresponding to the two endpoints of the active segment are non-zero; this is enforced by Equations (47) to (52).

Control formulation

Integrating the control objective function and constraints introduced above results in the following control formulation for the MPC-PCM strategy

$$min \sum_{t=t_0}^{t_f} r^t \cdot (P_{SC}^{t} + P_{PCM}^{t}) \tag{55}$$

subject to

$$\begin{cases} \text{Building thermal dynamic constraints: } (32) - (34) \\ \text{Building indoor temperature constraints: } (35) \\ \text{ASIHP operation constraints: } (39) - (44) \\ \text{PCM thermal dynamic constraints: } (26), (45) - (54) \\ \text{PCM boundary constaints: } (28) - (31) \end{cases}$$

Prediction of the building thermal dynamics in Equations (32) to (34) requires the initial state values, i.e., the nodal temperatures of the thermal network at the current time step. Only the zone air temperature is available from EnergyPlus and the other state variables are estimated using a Kalman filter-based state observer [74]. Note that the control problem above is nonlinear, non-convex and involves integer variables. The nonlinearity mainly stems from the ASIHP operation constraints given in Equations(36) and (39) to (42). To eliminate the nonlinearity and improve numerical feasibility, the following assumptions are made to pre-condition the optimization problem:

- The return wet-bulb temperature to the evaporator is fixed at 18°C;
- The return water temperature for the PCM charging mode is fixed at 19.7°C;
- The SHR during the SC mode assumes a constant value of 0.7

After the simplification, the control problem becomes a mixed-integer linear program and can be solved using mature commercial packages. This study uses the Gurobi solver [75] in the CVXPY Python suite [76] [77]. Note that the above assumptions are only applied in the control model while the simulation test bed still uses the nonlinear envelope and ASIHP models in EnergyPlus. The control model simplification may cause minor performance degradation but is critical for numerical feasibility.

It may be noted that the proposed control strategy assumes identical thermal properties for the solid and liquid phases of the PCM. However, it can also handle phase-dependent PCM thermal properties with very minor changes. Taking into consideration the different thermal properties of the PCM in different phases, Equation (26) should be revised as

$$h_j^{t+1} = \frac{\Delta t \cdot k_j^{t+1} \cdot \left(T_{j+1}^{t+1} - 2T_j^{t+1} + T_{j-1}^{t+1}\right)}{\rho_j^{t+1}(\Delta x)^2} + h_j^t, \forall j \in N, \forall t \in \Gamma \tag{56}$$

where

$$k_j^{t+1} = \begin{cases} k_l & h_j^{t+1} \geq h_{sl} \\ k_m = \dfrac{k_l + k_m}{2} & 0 \leq h_j^{t+1} \leq h_{sl} \\ k_s & h_j^{t+1} \leq 0 \end{cases} \quad \forall j \in N, \forall t \in \Gamma \tag{57}$$

$$\rho_j^{t+1} = \begin{cases} \rho_l & h_j^{t+1} \geq h_{sl} \\ \rho_m = \dfrac{\rho_l + \rho_m}{2} & 0 \leq h_j^{t+1} \leq h_{sl} \\ \rho_s & h_j^{t+1} \leq 0 \end{cases} \quad \forall j \in N, \forall t \in \Gamma \tag{58}$$

k_l and k_s represent the PCM thermal conductivity in liquid and solid phases, respectively, and ρ_l and ρ_s are the density of PCM in liquid and solid phases, respectively. When the PCM is in the state of melting/solidifying, its thermal properties are assumed to be the average of its liquid and solid properties. The above PCM thermal dynamic formulation has the thermal parameters following piecewise relationships with the enthalpy. To eliminate the nonlinearities in the optimization problem, the phase-dependent PCM thermal dynamic model can be reformulated into the following mixed integer form with the classic "big M" method:

$$\begin{aligned} -M \cdot \left(1 - \gamma_{j,i}^{t+1}\right) \leq h_j^{t+1} - \frac{\Delta t \cdot k_i \cdot \left(T_{j+1}^{t+1} - 2T_j^{t+1} + T_{j-1}^{t+1}\right)}{\rho_i(\Delta x)^2} - h_j^t \\ \leq M \cdot \left(1 - \gamma_{j,i}^{t+1}\right), \end{aligned} \tag{59}$$

where k_i and ρ_i are the ith element of the vector $\boldsymbol{k} = [k_s, k_m, k_l]^{\mathbf{T}}$ and $\boldsymbol{\rho} = [\rho_s, \rho_m, \rho_l]^{\mathbf{T}}$. The new control formulation would just need to replace the original PCM dynamic constraints in Equation (26) with the above equation.

MPC case without PCM TES

To separate the cost reduction potentials of the MPC control strategy and the PCM TES integration, a fourth case is considered where the MPC strategy is applied to manipulate the building sensible load profile through the passive storage only while the PCM TES is assumed to be absent. In this case, the MPC identifies the optimal ZAT trajectory that minimizes the total electricity cost, with the following control formulation:

$$min \sum_{t=t_0}^{t_f} r^t \cdot (P_{SC}^t) \tag{60}$$

subject to

$$\begin{cases} \text{Building thermal dynamic constraints: } (32) - (34) \\ \text{Building indoor temperature constraints: } (35) \\ \text{ASIHP operation constraints: } (39) - (44) \end{cases}$$

The same control simplifications discussed in Section 4.3.3 are applied to ensure numerical tractability. The obtained formulation is a linear program, the solution of which is much easier and can be handled by Gurobi. The difference in the cost savings between the MPC and MPC-PCM cases represents savings potential associated with the PCM TES integration.

4.4 Case Study Results

Simulation tests were performed for a 3-day period in July using the aforementioned control strategies, i.e., BC, RBC, MPC and MPC-PCM. A 1-hour time step was used for all simulation cases, and the MPC was implemented using a 24-hour look-ahead time horizon and a 1-hour decision time step. The cooling season ZAT upper and lower bounds assumed 23°C and 20°C, respectively, throughout the day for all cases. Table 10 displays the TOU electricity rates used in the simulation, based on the Georgia Power TOU-REO-13 tariff schedule [73]. The rate structure

is comprised of two pricing periods—on-peak and off-peak. The on-peak period is from 2 PM to 7 PM, and the rest of the day is considered off-peak. The on-peak electricity price is approximately 4 times the off-peak price, which coincides with the high electric demand on the grid and incentivizes load shifting from on-peak to off-peak periods. It may be noted that this tariff does not include a demand charge, so there is no penalty for increases in the peak electricity demand.

Table 10: Summer TOU electricity rates

Rate Periods	**Hours**	**Price (¢ per kWh)**
On-peak	2 PM to 7 PM	20.3217
Off-peak	12 AM to 2 PM and 7 PM to 12 AM	5.1638

Overlay plots of the simulated diurnal variations of key operational variables for all four strategies are shown in Figure 31 to Figure 46. The on-peak period is marked using the pink shaded area in all plots. A summary of the energy consumption and costs is displayed in Table 11. Figure 31 displays the variation of the ZAT and outdoor temperature (OAT) for all cases. For the RBC, MPC and MPC-PCM cases, the ZAT is maintained within the comfort band of 20°C-23°C. For the BC case, the ZAT is maintained at 23°C for most of the simulation period except for hours 17 and 41 (both 5 PM) where the ZAT occasionally rises to 23.3°C. The slight ZAT excursion is caused by the EnergyPlus sizing strategy, which auto-sizes the ASIHP system such that the cooling load will be sufficiently met for 99.6% of the time while the simulated days are the hottest of the year. Such temperature excursions are absent in the other strategies, showing the benefit of the PCM storage and advanced controls in comfort improvement.

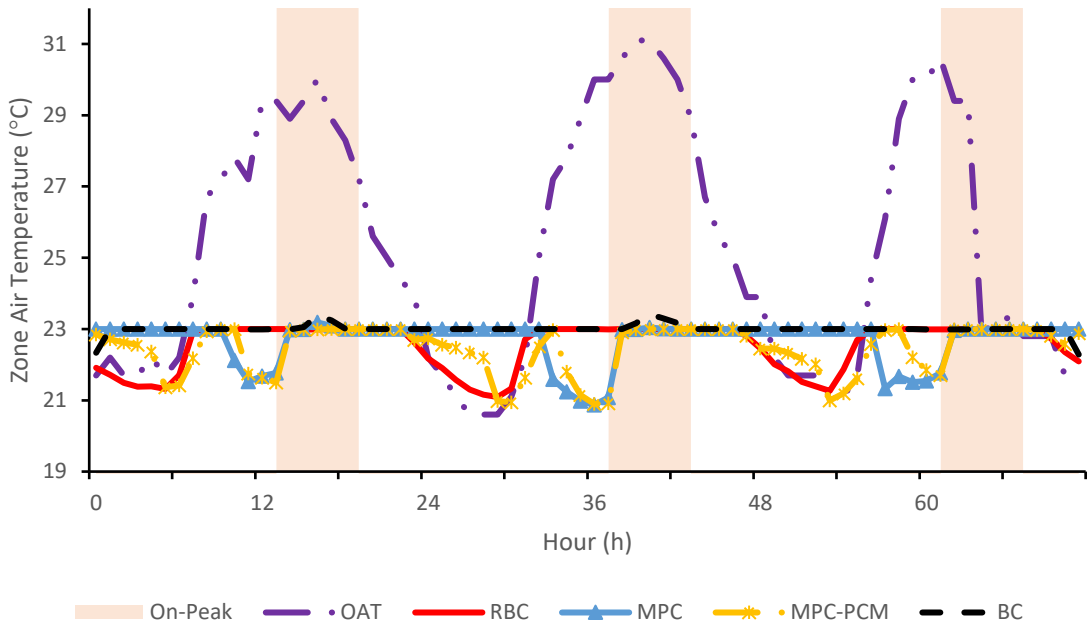


Figure 31: OAT and ZAT profile for the 3-day simulation of BC, RBC, MPC and MPC-PCM cases

4.4.1 BC results

The BC case is representative of the normal operation of an AC system without any PCM TES or advanced controls. Figure 32 and Figure 33 display the sensible and total cooling rates, respectively, delivered by the ASIHP unit in the SC mode. The peak cooling load coincides with the on-peak period when the outdoor temperature is at its highest resulting in significant heat gains from the ambient. The HVAC power (displayed in Figure 34) is also the highest during the on-peak period as the compressor runs at the medium stage and with longer duty cycles to provide sufficient cooling. Figure 35 displays the compressor speed level; the controller operates the compressor at the highest SC stage continuously during the high load periods of the first two simulation days (coinciding with ZAT excursions). When the compressor cycles between two adjacent stages, the average speed level weighted by the respective runtime fractions is plotted.

Approximately 37% of the total HVAC electric energy is consumed during the on-peak period, which is only 20.8% of the overall simulation period. This indicates a good peak load shifting potential through control optimization.

4.4.2 RBC results

For the RBC case, the ZAT setpoint is maintained constant, while the actual ZAT drops below its setpoint resulting in a zero mechanical cooling load during the early morning periods (around midnight to 8AM). This early pre-cooling action is not triggered by the RBC strategy as it involves a constant ZAT setpoint. Overcooling of the indoor space is caused by the self-discharge of the PCM, which generates a space cooling effect greater than the baseline sensible cooling load during the early mornings (see Figure 32). This is also evident from the liquid volume fraction (LVF) plot displayed in Figure 46, which is determined by averaging the ratio of the PCM enthalpy to h_{sl} across all control volumes—the LVF is 1 when the enthalpy is greater than h_{sl} (fully melted) and 0 when the enthalpy is less than 0 (fully solidified). In the RBC case, the PCM is still melting during the early morning periods (LVF is ascending) resulting in a self-discharge of the "cooling" energy. This overcooling of the space takes place before the onset of the PCM charging period and helps charge "cooling" energy into the building thermal mass; however, the stored cooling energy is fully released before the on-peak hours as shown by the gap between the baseline curve and the red area in Figure 32. Therefore, the coincidental pre-cooling action does not contribute any load shifting. In the first simulation day, there is some residual charge in the PCM from the previous day (warm-up period).

The RBC strategy reduces the total ASIHP cooling load (total DX coil load plus the cumulative PCM charge) by 7.8%, as shown in Table 11 and also evident by Figure 33. The PCM is never fully charged so the temperature of the PCM surface exposed to the room air is always higher than

the melting point, which is chosen to be high enough (19.7˚C in this study) to prevent formation of condensate on the ceiling surface, i.e., the PCM ceiling is designed not to handle any latent load. Since the DX coil sensible load is significantly offset by the PCM cooling effect (the PCM cooling accounts for 59.7% of the total space sensible cooling requirement), the DX SC runtime is much lower leading to reduced cumulative latent cooling effect and moisture removal. As a result, the average zone relative humidity increases from 57.9% for the BC case to 70.6% for the RBC case. Despite delivering lower total DX cooling energy, the RBC strategy delivers more sensible cooling to the indoor space (PCM charging and SC mode combined)—an increase of 3.9% compared to the BC case. The increase in sensible cooling delivery is due to the space overcooling in the early mornings and the residual thermal energy stored in the PCM at the end of the third day, which can be clearly seen from Figure 46. This represents a minor disadvantage of the RBC strategy as it cannot foresee the operation requirement of the following day and thereby is not able to guarantee PCM charge/discharge neutrality in a day. The unused thermal energy in the PCM can still help offset the cooling load of the next day, but in a non-coordinative manner. Because of the positive net "cooling" energy stored in the PCM, the cost calculation is unfavored as we only look at the 3-day results. However, the residual energy is only 1.6% of the cumulative PCM charge so its impact on the estimated cost savings potential is small.

Figure 36 compares the operational COP of the different cases. The RBC strategy results in a slightly lower average system COP (4.2) than the BC case (4.4). It should be noted that the average space cooling COP is actually increased with the RBC strategy because (1) the higher indoor humidity level contributes to efficiency improvement with elevated evaporator air inlet enthalpy and evaporation temperatures; and (2) with a fraction of the load handled by the PCM, the DX system runs predominantly on the low stage during the peak hours which involves a much higher

efficiency compared to the medium stage (see Figure 35 and Figure 36). However, the PCM charging COP is approximately 20% lower than the space cooling COP and since the PCM handles more than half of the sensible cooling load, the overall system COP is dominated by the PCM charging COP and thereby, is lower in the RBC case. The RBC operates the ASIHP to charge the PCM in the morning hours at a higher efficiency, leading to reduced operations of the system in the afternoon when the COP is lower. With the total load reduction outweighing the system efficiency degradation, the RBC results in a 3.2% reduction in the total HVAC electrical energy use.

The implementation of the RBC reduces the total electricity cost by 20.4% over the BC case. In addition to reduction of the ASIHP energy consumption, the cost reduction is also attributed to shifting of a portion of the cooling load from on-peak to off-peak periods, which is illustrated in Figure 34. The RBC case achieves the electric load shifting by running the chilled water to the PCM ceiling during the off-peak period to store “cooling energy” in the PCM which is then released to the indoor space during the on-peak period. During the discharge process, the cold PCM absorbs heat from the room through radiant and convective heat transfer, which offsets the indoor cooling load and reduces the cooling power use. The discharge process occurs naturally with the discharge rate dependent on the temperature difference between the ceiling surface and the indoor space. Due to the lack of active control, the cooling discharge extends beyond the on-peak period and lasts throughout the rest of the day.

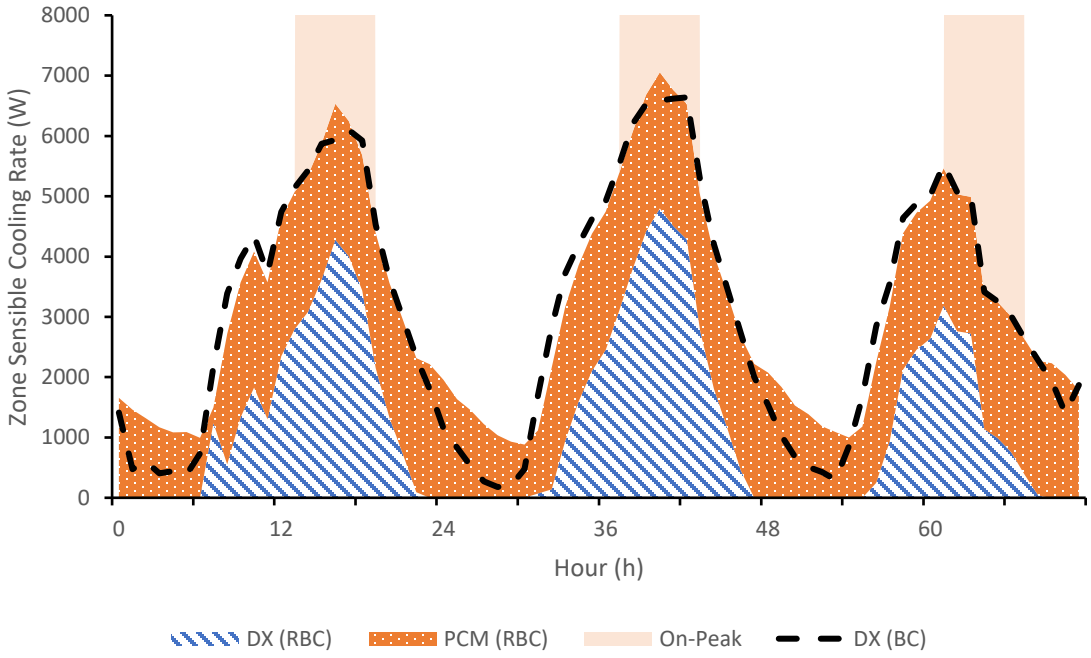


Figure 32: Zone sensible cooling rate profile for the 3-day simulation of BC and RBC cases

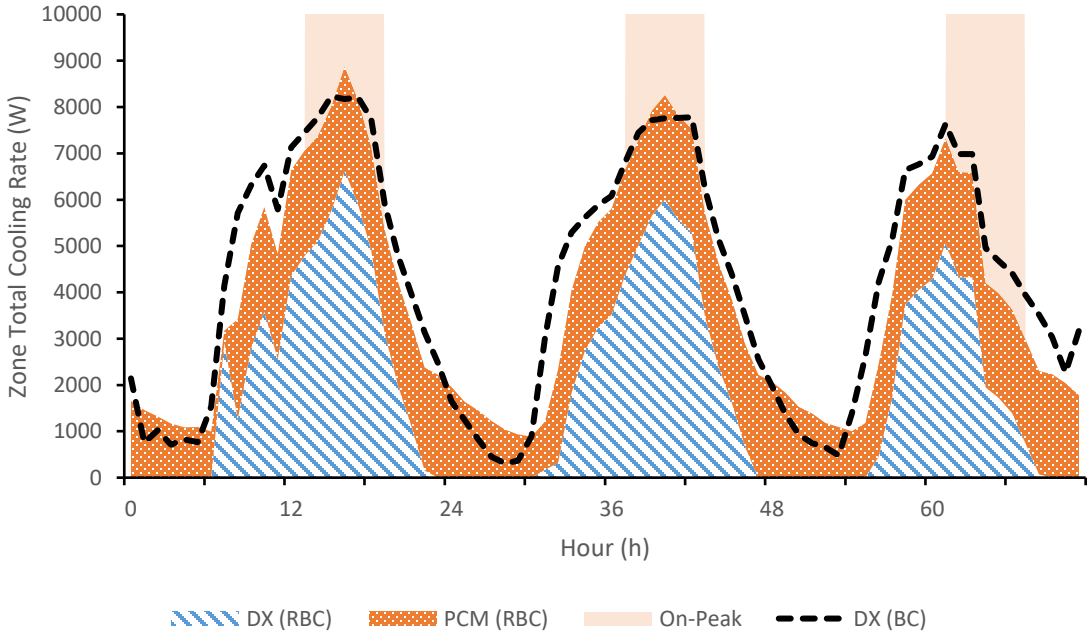


Figure 33: Zone total cooling rate profile for the 3-day simulation of BC and RBC cases

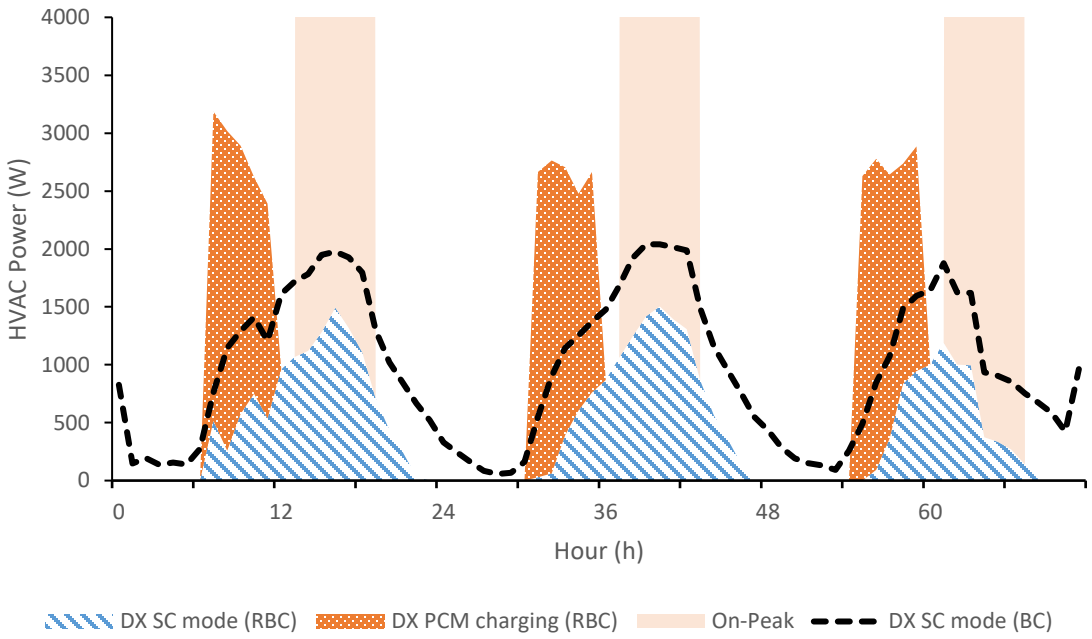


Figure 34: Total HVAC power profile for the 3-day simulation of BC and RBC cases

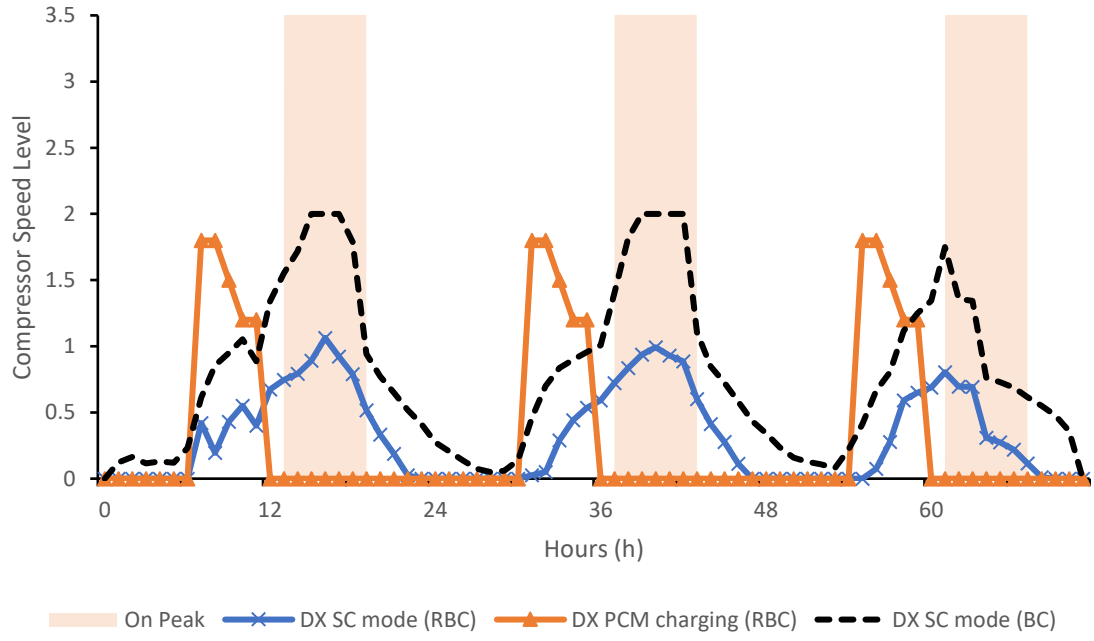


Figure 35: Compressor speed level profile for the 3-day simulation of BC and RBC cases

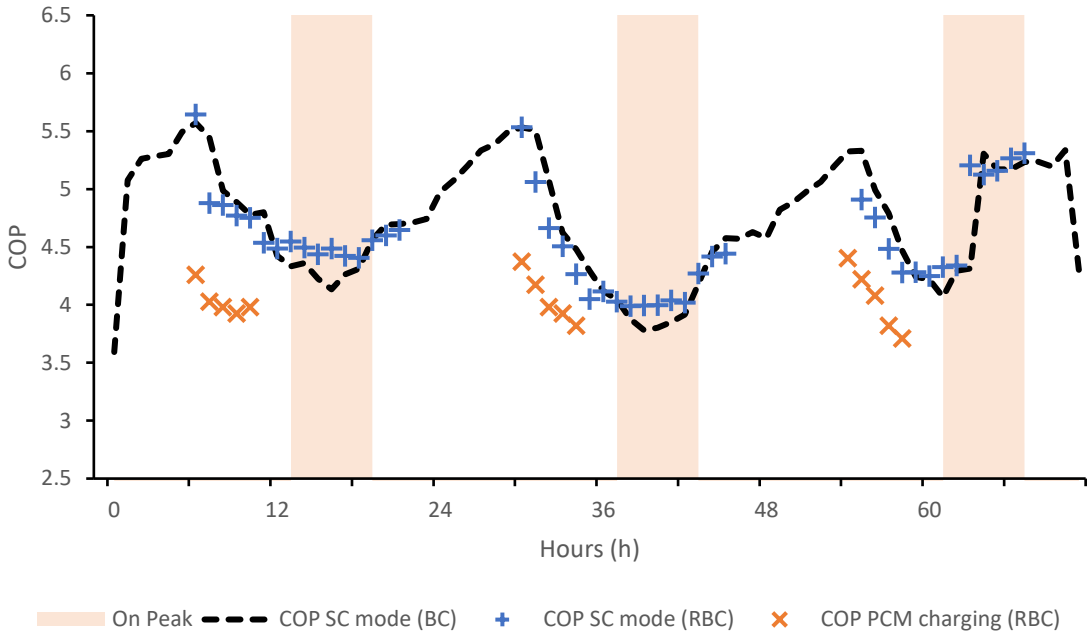


Figure 36: COP profile for the 3-day simulation of BC and RBC cases

4.4.3 MPC results

For the MPC case, a pre-cooling action is also undertaken, which results in a decrease of the ZAT and pre-cools the indoor space right before the on-peak period to charge "cooling" energy into the passive thermal mass, associated with the construction materials and indoor furniture. During the on-peak hours, the ZAT is adjusted upwards allowing release of the stored "cooling" energy to offset the indoor cooling requirement. Figure 37 illustrates this effect: there is an increase in the DX SC mode sensible cooling rate in the hours preceding the on-peak period, which is followed by a sharp decrease in the sensible cooling rate at the onset of the on-peak period. The MPC strategy increases the total DX cooling energy by 3.2% compared to the BC case because more cooling is required during the pre-cooling period to compensate for the greater heat gains from the ambient due to the increase in the temperature difference between the indoor and outdoor spaces.

However, the implementation of the MPC strategy reduces the total electricity cost by 3.9% over the BC case, mainly through the shifting of the ASIHP electric consumption from the on-peak to off-peak periods, which is illustrated in Figure 39. Compared to the MPC-PCM case (to be discussed in the next section), the MPC strategy undertakes more aggressive pre-cooling actions with lower pre-cooling temperatures to enable deeper utilization of the passive building thermal mass, in the absence of the PCM storage. The precooling time is chosen to be right before the on-peak period, instead of the early morning high-efficiency hours, because the increase of heat gains for earlier pre-cooling significantly outweighs the COP enhancement benefit. As a consequence, the average COP in the MPC case is almost identical to that of the BC case.

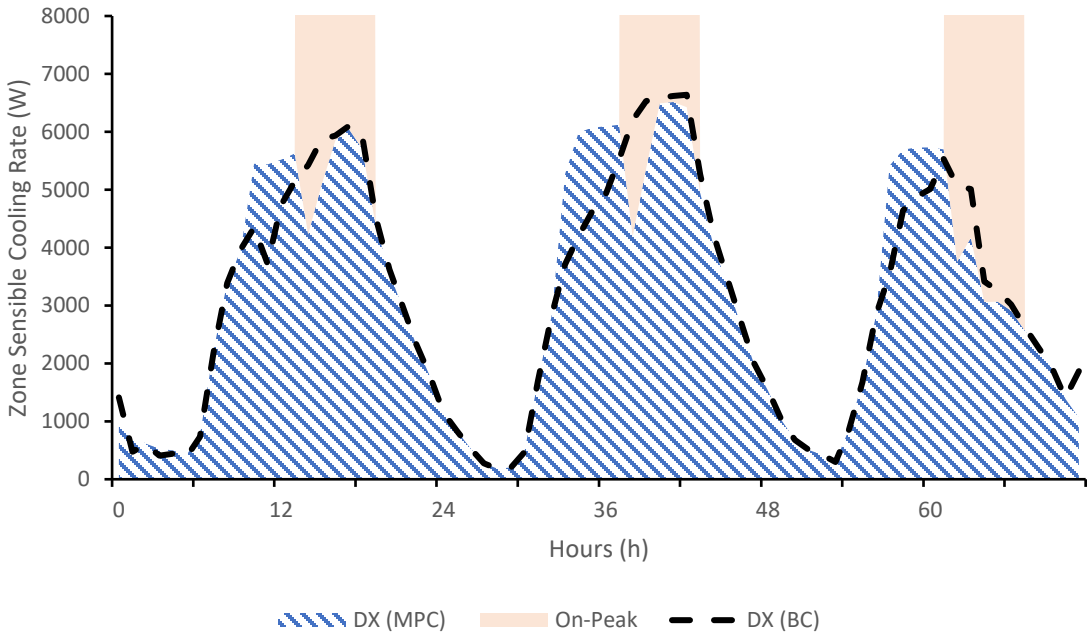


Figure 37: Zone sensible cooling rate profile for the 3-day simulation of BC and MPC cases

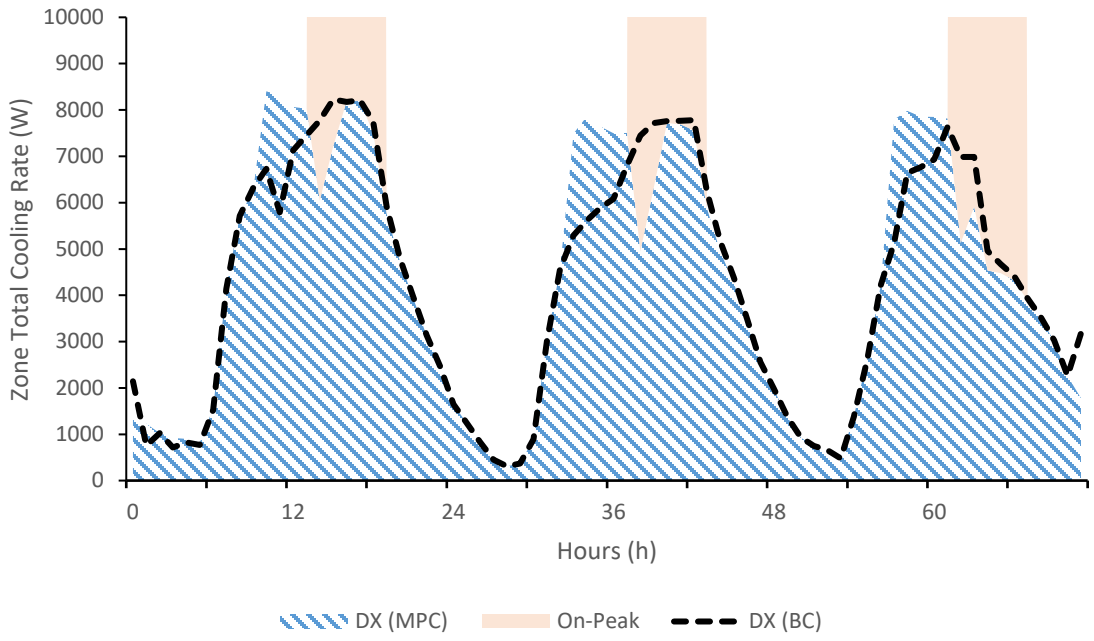


Figure 38: Zone total cooling rate profile for the 3-day simulation of BC and MPC cases

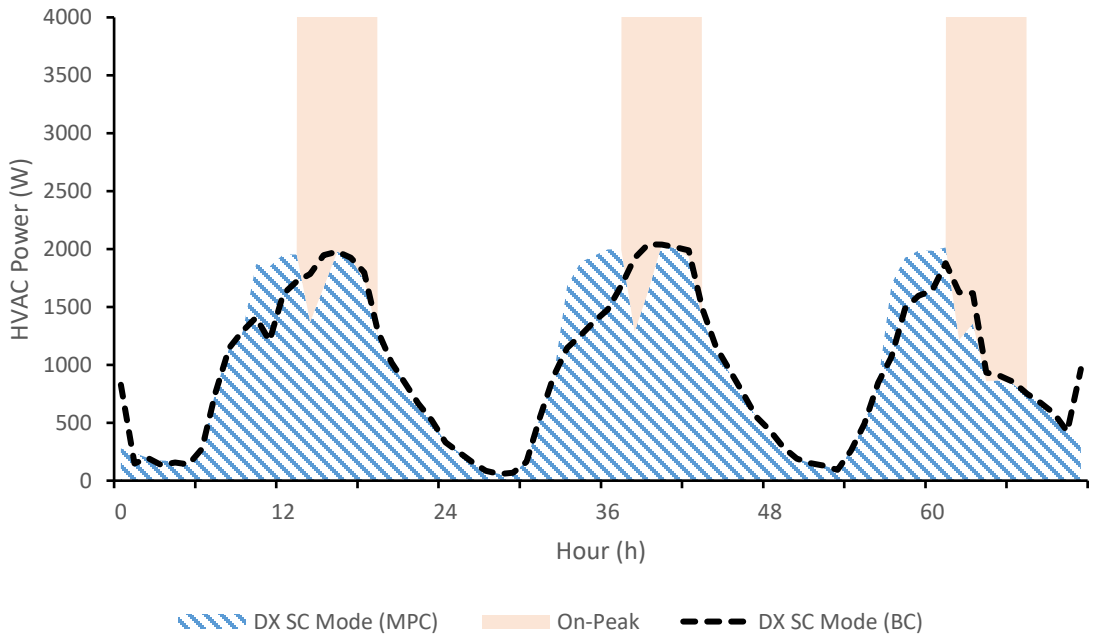


Figure 39: Total HVAC power profile for the 3-day simulation of BC and MPC cases

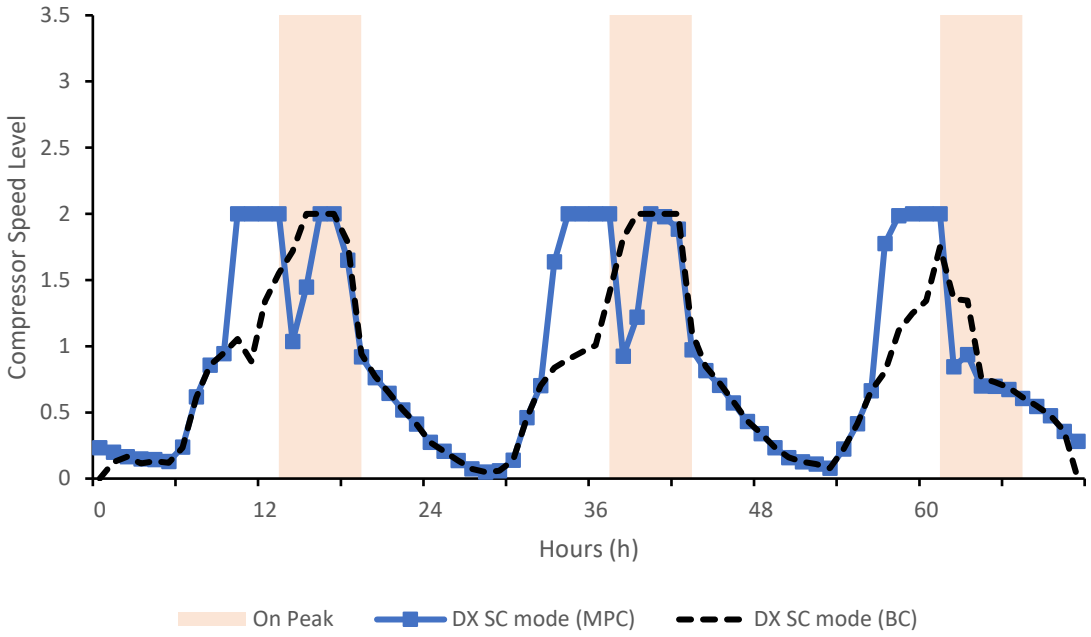


Figure 40: Compressor speed level profile for the 3-day simulation of BC and MPC cases

4.4.4 MPC-PCM results

The MPC-PCM strategy undertakes two pre-cooling actions each day, one during the PCM charging hours and one right before the on-peak hours. The early-morning pre-cooling is a consequence of the PCM charging actions where the PCM surface temperature is reduced and the PCM cooling effect is greater than the zone cooling load. Figure 31 shows that the ZAT is slightly below 23°C in the early morning hours and then decreases sharply when aggressive PCM charging is enabled (shown in Figure 43). As the PCM charging rate ramps up, the "cold" energy propagates through the PCM ceiling, causing gradual solidification of the PCM and reduction of its temperature (see Figure 46). The temperature decrease results in a PCM space cooling rate higher than the sensible cooling load and overcooling of the indoor space during the early mornings. The second pre-cooling action is undertaken by the air system as a means to further shift the sensible

zone cooling load; this pre-cooling is called for right before the on-peak hours and only lasts for a few hours to minimize the load increment during the pre-cooling period while still taking advantage of the cheaper off-peak electricity.

The MPC-PCM case decreases the total delivered ASIHP cooling energy by 7.6% compared to the BC case because of the reduced latent load, and involves a higher sensible cooling load (PCM charging and SC mode combined)—an increase of 4.0%—due to the high ambient-driven heat gains during the pre-cooling periods. These behaviors are similar to those associated with the RBC case. The major differentiating feature lies in that the MPC-PCM strategy combines the electric load shifting capabilities of the passive (building construction materials) and active (PCM ceiling) storage and uses the weather and load forecasts in determining the optimal system operations at each time step. The superiority of the MPC-PCM over the RBC strategy is reflected by two major distinct behaviors: (1) the PCM is charged at a much higher rate but for a much shorter duration, which maximizes the efficiency benefit by operating the chilled water circuit during the coolest hours of the day; and (2) utilization of the passive building thermal mass through precooling of the indoor space prior to on-peak hours. Because of (1), the MPC-PCM strategy achieves a higher average system efficiency compared to the RBC case (still lower than the BC case). Figure 45 compares the operational COP for the various cases. An additional 6.7% electricity cost savings is enabled by the MPC-PCM strategy beyond the 20.4% savings achieved in the RBC case, resulting in a total electricity cost reduction by 27.1%. By combining both the passive and active energy storage capacities, the MPC-PCM case achieves the lowest electricity cost out of the four simulation cases. Unlike the RBC case, the MPC-PCM case can predict a day ahead and ensure the energy stored in the PCM is fully utilized by the end of the day as shown in Figure 46. This

maximizes the load shifting capabilities despite the PCM zone cooling energy accounting for less (53.3%) of the total zone sensible cooling energy in the MPC-PCM case.

To further evaluate the electricity cost savings potential of the proposed PCM TES solution, a month-long simulation study for July was conducted as an extension of the 3-day simulation. The month-long electricity cost for the BC, RBC and MPC-PCM cases were \$82.22, \$73.43(↓ 10.7%) and \$62.87(↓ 23.5%), respectively. The monthly percentage savings of the proposed MPC strategy relative to the baseline case were comparable to the 3-day simulation results, while much lower monthly cost savings were achieved for the RBC case. The poor performance of the RBC case was expected as the control settings were carefully fine-tuned to maximize the performance during the 3 simulated days which may be sub-optimal in other days. The results clearly demonstrate the superior performance of the MPC strategy which could provide consistent savings requiring no engineering inputs in the execution phase.

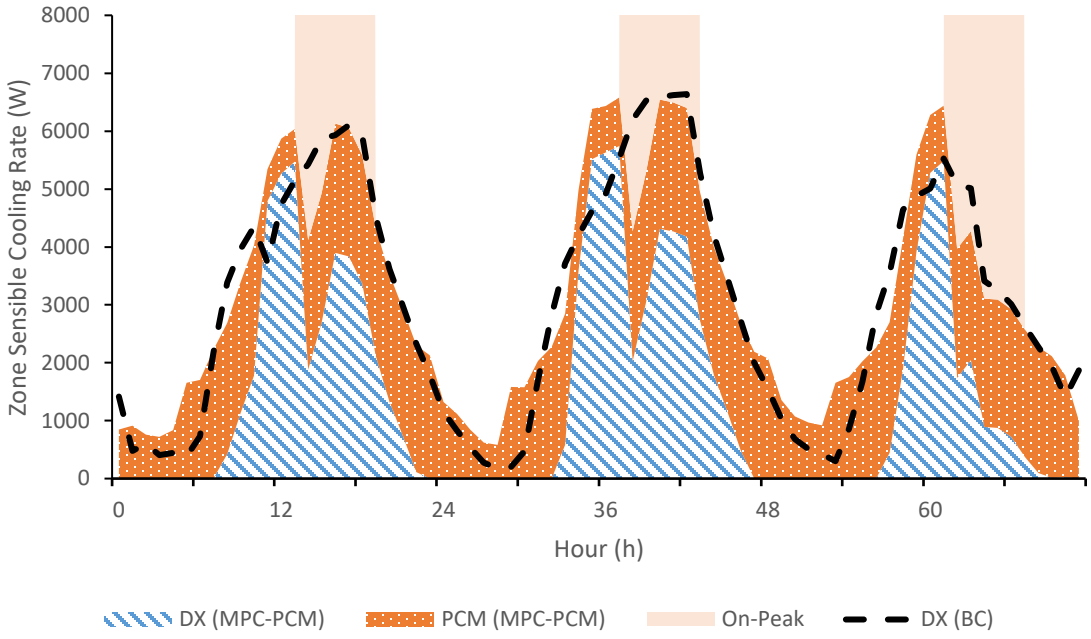


Figure 41: Zone sensible cooling rate profile for the 3-day simulation of BC and MPC-PCM cases

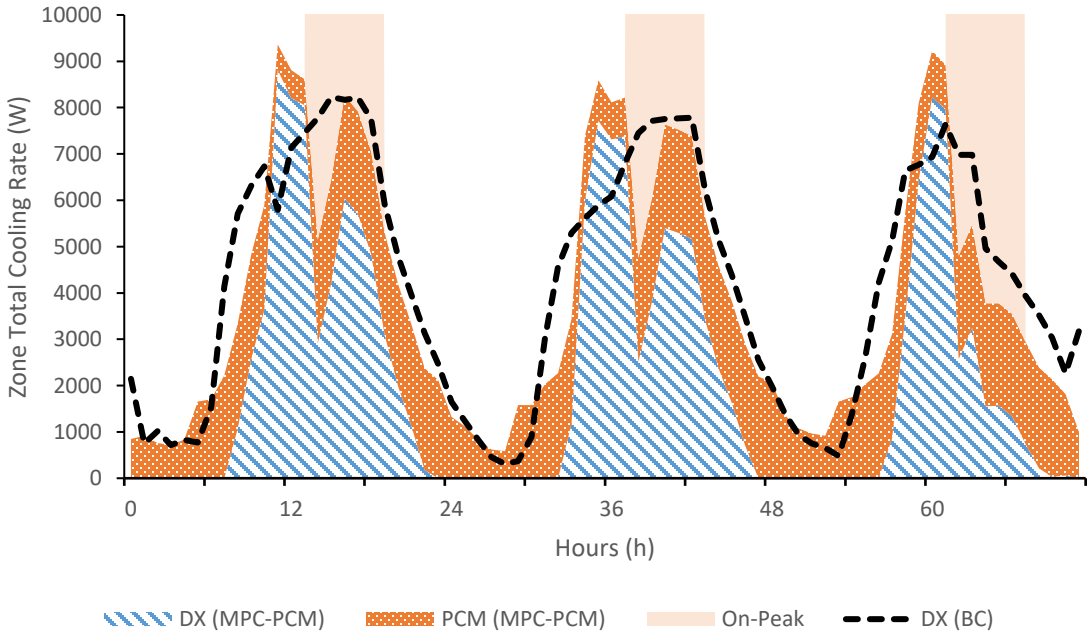


Figure 42: Zone total cooling rate profile for the 3-day simulation of BC and MPC-PCM cases

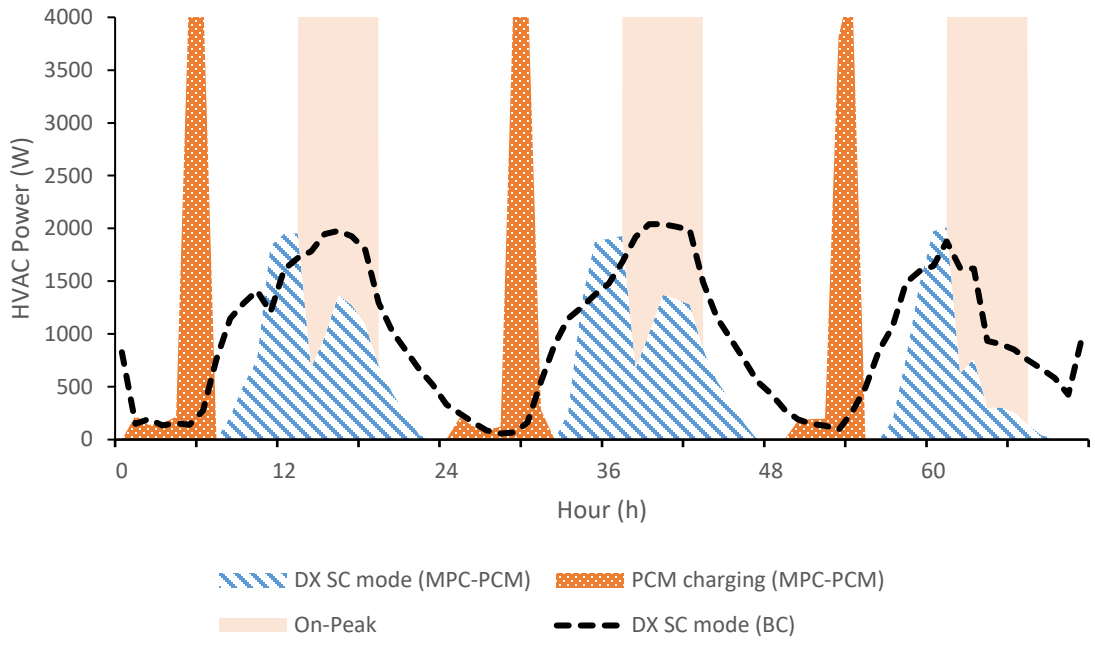


Figure 43: Total HVAC power profile for the 3-day simulation of BC and MPC-PCM cases

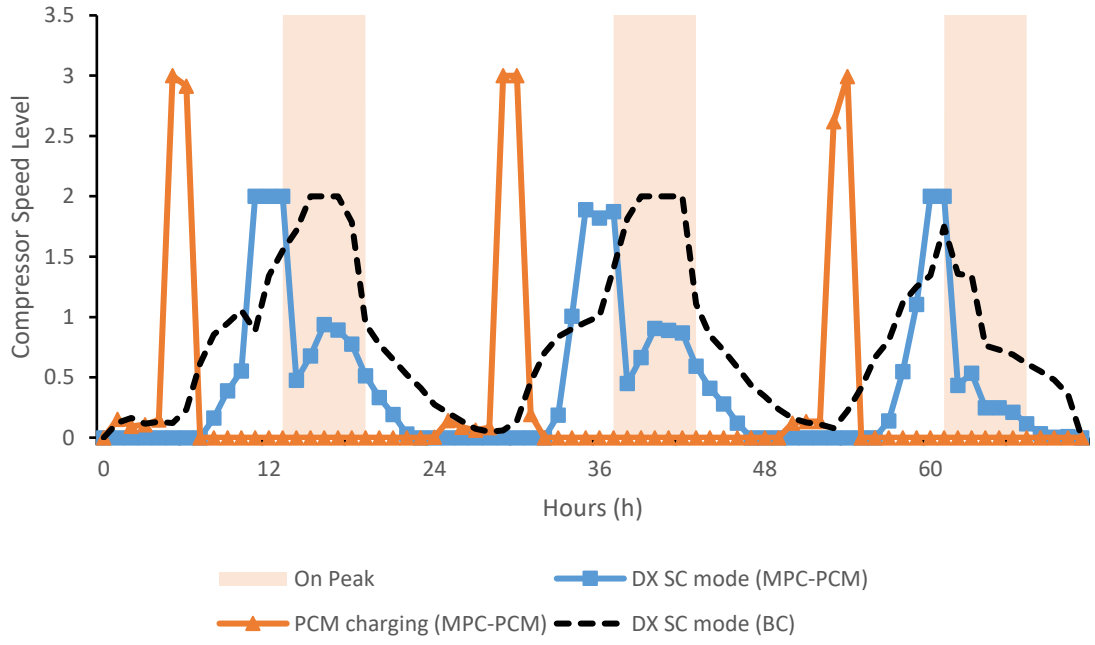


Figure 44: Compressor speed level profile for the 3-day simulation of BC and MPC-PCM cases

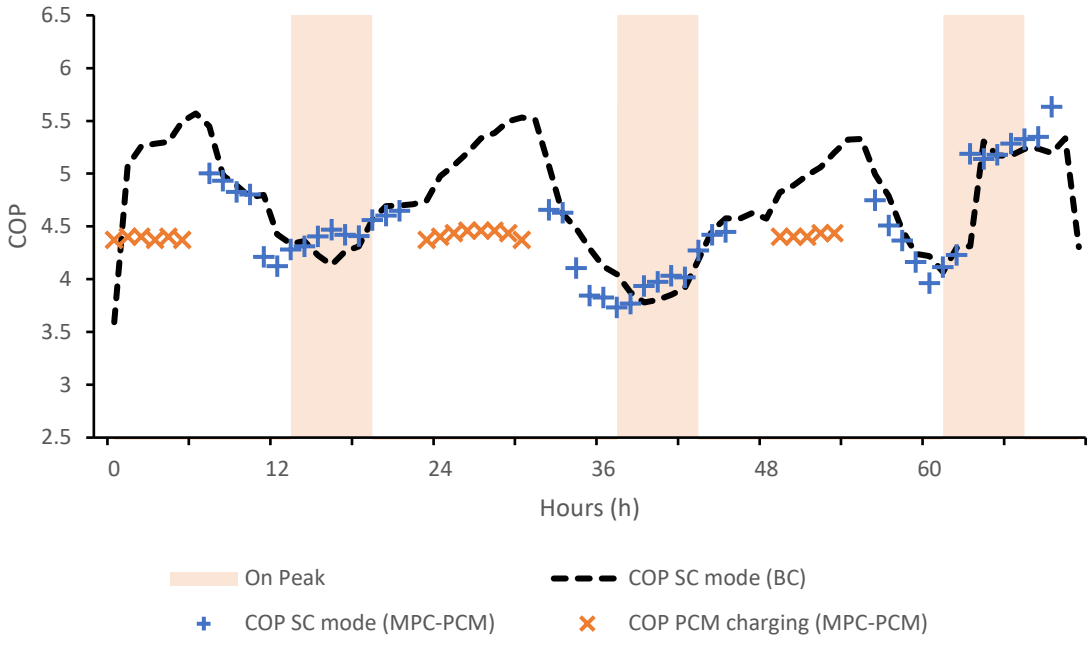


Figure 45: COP profile for the 3-day simulation of BC and MPC-PCM cases

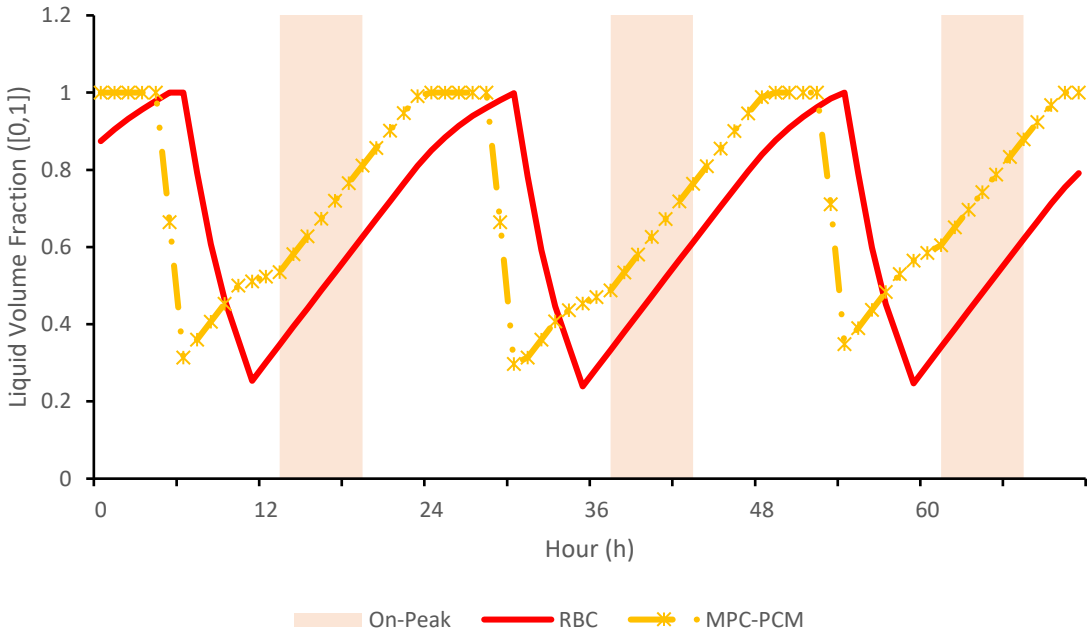


Figure 46: LVF profile for the 3-day simulation of RBC and MPC-PCM cases

Table 11: Summary of 3-day simulation results for four control cases

	BC	**RBC**	**MPC**	**MPC-PCM**
COP	4.4	4.2	4.4	4.3
Average Relative Humidity (%)	57.9	70.6	58.2	70.1
PCM Space Cooling Energy (kWh)	—	137.4	—	123.1
DX SC mode Sensible Cooling Energy (kWh)	221.2	92.8	225.9	107.7
DX SC mode Latent Cooling Energy (kWh)	85.0	49.7	87.1	52.9
DX SC mode Total Cooling Energy (kWh)	306.2	142.5	313.0	160.6
PCM Charging Energy (kWh)	—	139.7	—	122.4
Total ASIHP Cooling Energy (kWh)	306.2	282.2 (↓7.8 %)	313.0 (↑2.2 %)	283.0 (↓7.6 %)
On-Peak HVAC Electric Energy (kWh)	25.4	16.2 (↓36.2 %)	22.7 (↓10.6 %)	13.3 (↓47.3 %)
Off-Peak HVAC Electric Energy (kWh)	43.7	50.7 (↑16.0 %)	48.6 (↑11.2 %)	52.1 (↑19.2 %)
Total HVAC Electric Energy (kWh)	69.1	66.9 (↓3.2 %)	71.3 (↑3.2 %)	65.4 (↓5.4 %)
Total Electricity Cost ($)	7.41	5.90 (↓20.4 %)	7.12 (↓3.9 %)	5.40 (↓27.1 %)

4.5 Concluding Remarks

This chapter presented a model-based predictive control strategy for PCM-embedded ceiling energy storage deployed with an ASIHP. The inherent nonlinearity in the PCM heat transfer process and ASIHP component model make the control problem difficult to solve directly. Conventional gradient-based algorithms are not suitable because of the non-differentiability of the piecewise linear PCM temperature-enthalpy relationship. To address this numerical issue, the PCM thermal dynamics were characterized using a mixed-integer linear formulation. In addition, the ASIHP model used in the controller was simplified by assuming a fixed return air wet-bulb temperature to the evaporator and a fixed return water temperature to eliminate the nonlinear couplings between the ASIHP and envelope models and improve numerical feasibility. With these reformulations, the final control problem was converted to a mixed-integer linear program which can be handled using mature solvers.

Three baseline control strategies were considered and simulated to evaluate the benefits of the proposed predictive control strategy using a simulation case study involving a residential building and a TOU electricity rate schedule. The predictive strategy achieved the highest electricity cost savings (27.1%) while a rule-based strategy employing a pre-determined PCM charge/discharge schedule resulted in noticeably lower cost savings (20.4%). The proposed predictive control strategy made effective use of both the passive building thermal mass and the PCM storage to achieve deep load shifting: activation of the building thermal mass was accomplished through pre-cooling the zone right before the on-peak period, while the PCM was charged by turning on the chilled water circuit in the very early morning when the refrigeration efficiency was the highest.

It was found in the case study that the use of the PCM TES could cause potential humidity control issues. This is because the cooling delivery through the PCM ceiling offsets more than half of the DX coil sensible load, which reduces the DX coil run time and its dehumidification capability. This finding indicates a potential improvement in the current ASIHP design to enhance the moisture removal capacity of the DX coil. In this study, the size of the ASIHP was assumed identical across all the simulated scenarios. A more practical design of the ASIHP should size the different components according to the specific configuration. For systems integrated with PCM TES, a smaller DX coil can be employed due to the reduced DX load. Further, the results show the potential of the predictive control strategy and the PCM TES to manipulate a building's diurnal load profile through zone temperature and PCM charge/discharge controls. This load shifting ability can be leveraged to reduce the capacity requirement and downsize the mechanical equipment, which can help offset the cost of the PCM TES and improve the economics of this solution package.

5. Summary and Future Work

5.1 Summary

This dissertation investigated PCM-based latent TES integrated with building HVAC systems to improve demand flexibility, reduce on-peak electricity use, and lower cooling-season energy cost. Two system concepts were developed, modeled, and evaluated at building scale using respective Energyplus co-simulation platforms: (i) in-duct PCM panels charged/discharged by rule-based dynamic SAT reset, and (ii) PCM-embedded ceiling panels charged by a chilled-water loop and coordinated with a multi-stage air-source integrated heat pump (ASIHP) under model predictive control (MPC). Key technical and practical outcomes are:

1. *Peak demand and cost reductions:* In-duct PCM TES with a simple rule-based SAT schedule effectively shifted substantial on-peak sensible load to off-peak hours and reduced on-peak HVAC electricity use by up to 31.5% and seasonal cooling electricity cost by 11–16% across five climate locations. PCM-embedded ceilings under MPC achieved up to 27.1% electricity cost savings in the residential case study while outperforming fine-tuned rule-based alternatives.
2. *Efficiency and equipment effects:* Both solutions increased system cycle COP during PCM discharge by enabling higher evaporating temperatures (higher SAT or more favorable evaporator conditions). However, total seasonal electricity sometimes increased (round-trip storage loss) because of extra off-peak charging energy and increased ventilation/fan work during discharge; cost savings nevertheless resulted under TOU tariffs
3. *MPC vs rule-based control*: The MPC strategy that jointly scheduled PCM charging and zone temperature trajectories substantially outperformed fixed rule-based schedules. The

MPC strategy combined active PCM charging with passive building thermal mass activation (pre-cooling) to maximize cost savings while ensuring comfort.

4. *Economic performance:* Simple payback estimates for the in-duct concept ranged from under one cooling season (favorable climates/tariffs) to multiple seasons depending on local tariffs and sizing; economic performance improves when PCM use is coupled with optimized control and tariff structures that reward load shifting.
5. *In-duct PCM considerations:* The PCM TES rack prototype demonstrated the benefit of more dense energy storage to reduce the duct length requirement and improved installation, customization and decommissioning; however, this comes at a tradeoff with the increased fan power consumption due to increased cross-sectional air blockage.

5.2 Future Work

The work presented in this dissertation can be extended in several directions:

1. Control and optimization enhancements
    - Develop stochastic MPC (or robust MPC) that explicitly accounts for forecast uncertainty in weather, occupancy, and electricity price to preserve cost savings under realistic operating conditions.
    - Integrate explicit humidity constraints and formulate humidity-aware MPC to avoid dehumidification shortfalls when PCM supplies large fractions of sensible load.
2. System integration and operation studies
    - Extend simulations to include coordinated air-side economizer control, variable outdoor-air fraction, and demand-charge-aware objectives so the controller can prevent off-peak load spikes that raise demand charges.

- Evaluate co-optimization of PCM operation with on-site distributed energy resources (PV, battery storage, EV charging) and participation in wholesale/ancillary markets to quantify stacked value streams.

3. Experimental pilots and field validation
    - Deploy controlled field pilots: (i) an in-duct PCM TES retrofit in a medium office AHU, and (ii) a PCM-embedded ceiling paired with a multi-stage ASIHP in a detached house or test house. Collect seasonal operation data to validate modeled savings, humidity impacts, and maintenance/operational issues.
    - Implement the MPC algorithms in building automation controllers (or edge devices) and test closed-loop robustness, communication latency effects in live systems.
4. PCM TES lifecycle assessment
    - Conduct a thorough life-cycle cost analysis including installation labor, encapsulation, maintenance, PCM degradation, recycling/disposal, and interactions with equipment sizing (downsizing DX coils or fans).
    - Assess long-term PCM cyclic stability, subcooling, phase segregation, and real-world performance degradation.

References

[1] B. Jones-Albertus, "Confronting the Duck Curve: How to Address Over-Generation of Sola Energy," Office of Energy Efficiency and Renewable Energy, 12 October 2017. [Online] Available: https://www.energy.gov/eere/articles/confronting-duck-curve-how-address-over generation-solar-energy. [Accessed 28 November 2020].

[2] Energy Information Administration, "Electric Power Annual 2019," 2021.

[3] Energy Information Administration, "Use of electricity," 7 April 2021. [Online]. Available: https://www.eia.gov/energyexplained/electricity/use-of-electricity.php. [Accessed 29 April 2021].

[4] US Department of Energy, "Energy Efficiency Trends in Residential and Commercial Buildings," 2010.

[5] M. Iten, S. Liu and A. Shukla, "A review on the air-PCM-TES application for free cooling and heating in the buildings," *Renewable and Sustainable Energy Reviews,* vol. 61, pp. 175-186, 2016.

[6] N. J. Hewitt, "Heat pumps and energy storage – The challenges of implementation," *Applied Energy,* vol. 89, no. 1, pp. 37-44, 2012.

[7] K. Hedegaard, Mathiesen, B. V, H. Lund and P. Heiselberg, "Wind power integration using individual heat pumps – Analysis of different heat storage options," *Energy,* vol. 47, no. 1, pp. 284-293, 2012.

[8] J. Le Dréau and P. Heiselberg, "Energy flexibility of residential buildings using short term heat storage in the thermal mass," *Energy,* vol. 111, pp. 991-1002, 2016.

[9] Z. Rahimpour, A. Faccani, D. Azuatalam, A. Chapman and G. Verbič, "Using Thermal Inertia of Buildings with Phase Change Material for Demand Response," *Energy Procedia,* vol. 121, pp. 102-109, 2017.

[10] M. Saffari, A. de Gracia, S. Ushak and L. Cabeza, "Economic impact of integrating PCM as passive system in buildings using Fanger comfort model," *Energy and Buildings,* vol. 112, pp. 159-172, 2016.

[11] D. Neeper, "Thermal dynamics of wallboard with latent heat storage," *Solar Energy,* vol. 68, no. 5, pp. 393-403, 2000.

[12] A. K. Sleiti and E. J. Naimaster, "Application of Fatty Acid Based Phase-Change Material to Reduce Energy Consumption From Roofs of Buildings," *Journal of Solar Energy Engineering,* vol. 138, no. 5, p. 051003, 2016.

[13] A. Athienitis, C. Liu, D. Hawes, D. Banu and D. Feldman, "Investigation of the thermal performance of a passive solar test-room with wall latent heat storage," *Building and Environment,* vol. 32, no. 5, pp. 405-410, 1997.

[14] K. Lin, Y. Zhang, H. Di and R. Yang, "Study of an electrical heating system with ductless air supply and shape-stabilized PCM for thermal storage," *Energy Conversion and Management,* vol. 48, no. 7, pp. 2016-2024, 2007.

[15] S. Li, G. Sun, K. Zou and X. Zhang, "Experimental research on the dynamic thermal performance of a novel triple-pane building window filled with PCM," *Sustainable Cities and Society,* vol. 27, pp. 15-22, 2016.

[16] T. Silva, R. Vicente, C. Amaral and A. Figueiredo, "Thermal performance of a window shutter containing PCM: Numerical validation and experimental analysis," *Applied Energy,* vol. 179, pp. 64-84, 2016.

[17] F. Souafayne, F. Fardoun and P.-H. Biwole, "Phase change materials (PCM) for cooling applications in buildings: A review," *Energy and Buildings,* vol. 129, pp. 396-431, 2016.

[18] B. Zalba, J. M. Marin, L. F. Cabeza and H. Mehling, "Free-cooling of buildings with phase change materials," *International Journal of Refrigeration,* vol. 27, no. 8, pp. 839-849, 2004.

[19] A. Mosaffa, C. Infante Ferreira, F. Talati and M. Rosen, "Thermal performance of a multiple PCM thermal storage unit for free cooling," *Energy Conversion and Management,* vol. 67, pp. 1-7, 2013.

[20] M. Anisur, M. Kibria, M. Mahfuz, R. Saidur and I. Metselaar, "Cooling of air using heptadecane phase change material in shell and tube arrangement: Analytical and experimental study," *Energy and Buildings,* vol. 85, pp. 98-106, 2014.

[21] E. Osterman, V. Butala and U. Stritih, "PCM thermal storage system for 'free' heating and cooling of buildings," *Energy and Buildings,* vol. 106, pp. 125-133, 2015.

[22] S. Takeda, K. Nagano, T. Mochida and K. Shimakura, "Development of a ventilation systemfor granules containing phase change material," *Solar Energy,* vol. 77, pp. 329-338, 2004.

[23] K. Yanbing, J. Yi and Z. Yinping, "Modeling and experimental study on an innovative passive cooling system—NVP system," *Energy and Buildings,* vol. 35, no. 4, pp. 417-425, 2003.

[24] T. Hong, S. Wang, F. Wang and X. Wang, "Experimental study on the demand shifting effects of PCM integrated air-conditioning duct," in *IOP Conference Series: Earth and Environmental Science*, 2019.

[25] T. Hong, S. Wang, F. Wang and X. Wang, "Study on the optimization of PCM integrated air-conditioning duct for the demand shifting," in *IOP Conference Series: Earth and Environmental Science*, 2019.

[26] M. Helm, C. Keil, S. Hiebler, H. Mehling and C. Schwiegler, "Solar heating and cooling system with absorption chiller and low temperature latent heat storage: Energetic performance and operational experience," *International Journal of Refrigeration,* vol. 32, no. 4, pp. 596-606, 2009.

[27] M. Helm, K. Hagel, W. Pfeffer, S. Hiebler and C. Schweigler, "Solar Heating and Cooling System with Absorption Chiller and Latent Heat Storage – A Research Project Summary," *Energy Procedia,* vol. 48, pp. 837-849, 2014.

[28] J. Belmonte, M. Izquierdo-Barrientos, P. Eguia, A. Molina and J. Almendros-Ibanez, "PCM in the heat rejection loops of absorption chillers. A feasibility study for the residential sector in Spain," *Energy and Buildings,* vol. 80, pp. 331-351, 2014.

[29] R. Tackett, "Case study: office building uses ice storage, heat recovery, and cold air distribution," *ASHRAE Transactions,* vol. 95, no. 1, pp. 1113-1121, 1989.

[30] C. Sohn, "Field performance of an ice harvester storage cooling system," *ASHRAE Transactions,* vol. 97, no. 2, pp. 1187-1193, 1991.

[31] E. Oro, A. de Garcia, A. Castell, M. Farid and L. Cabeza, "Review on phase change materials (PCMs) for cold thermal energy storage applications," *Applied Energy,* vol. 99, pp. 513-533, 2012.

[32] Y. Yau and S. Lee, "Feasibility study of an ice slurry-cooling coil for HVAC and R systems in a tropical building," *Applied Energy,* vol. 87, no. 8, pp. 2699-2711, 2010.

[33] S. Morgan and M. Krarti, "Field testing of optimal controls of passive and active thermal storage," *ASHRAE Transactions,* vol. 116, no. 1, pp. 134-146, 2010.

[34] D.-I. Bogatu, O. B. Kazanci and B. W. Olesen, "An experimental study of the active cooling performance of a novel radiant ceiling panel containing phase change material (PCM)," *Energy and Buildings,* vol. 243, p. 110981, 2021.

[35] J. Skovajsa, P. Drabek, S. Sehnalek and M. Zalesak, "Design and experimental evaluation of phase change material based cooling ceiling system," *Applied Thermal Engineering,* vol. 205, p. 118011, 2022.

[36] H. Weinläder, F. Klinker and M. Yasin, "PCM cooling ceilings in the Energy Efficiency Center—passive cooling potential of two different system designs," *Energy and Buildings,* vol. 119, pp. 93-100, 2016.

[37] S. Mousavi, B. Rismanchi, S. Brey and L. Aye, "PCM embedded radiant chilled ceiling: A state-of-the-art review," *Renewable and Sustainable Energy Reviews,* vol. 151, p. 111601, 2021.

[38] A. de Gracia, C. Fernández, A. Castell, C. Mateu and L. F. Cabeza, "Control of a PCM ventilated facade using reinforcement learning techniques," *Energy and Buildings,* vol. 106, pp. 234-242, 2015.

[39] M. Fiorentini, J. Wall, Z. Ma, J. H. Braslavsky and P. Cooper, "Hybrid model predictive control of a residential HVAC system with on-site thermal energy generation and storage," *Applied Energy,* vol. 187, pp. 465-479, 2017.

[40] G. Serale, M. Fiorentini, A. Capozzoli, P. Cooper and M. Perino, "Formulation of a model predictive control algorithm to enhance the performance of a latent heat solar thermal system," *Energy Conversion and Management,* Vols. 438-449, p. 173, 2018.

[41] G. Gholamibozanjani, J. Tarragona, A. de Gracia, C. Fernández, L. F. Cabeza and M. M. Farid, "Model predictive control strategy applied to different types of building for space heating," *Applied Energy,* vol. 231, pp. 959-971, 2018.

[42] C. R. Touretzky and M. Baldea, "A hierarchical scheduling and control strategy for thermal energy storage systems," *Energy and Buildings,* vol. 110, pp. 94-107, 2016.

[43] C. Dullinger, W. Struckl and M. Kozek, "A general approach for mixed-integer predictive control of HVAC systems using MILP," *Applied Thermal Engineering,* vol. 128, pp. 1646-1659, 2018.

[44] J. Sanchez, Z. Jiang and J. Cai, "Modelling and mitigating lifetime impact of building demand responsive control of heating, ventilation and air-conditioning systems," *Journal of Building Performance Simulation,* vol. 15, no. 6, pp. 771-787, 2022.

[45] J. Cai, H. Zhang and X. Jin, "Aging-aware predictive control of PV-battery assets in buildings.," *Applied Energy,* vol. 236, pp. 478-488, 2019.

[46] Z. Jiang, P. Hlanze and J. Cai, "Optimal predictive control of phase change material-based energy storage in buildings via mixed-integer convex programming," *Applied Thermal Engineering,* vol. 215, p. 118821, 2022.

[47] Y. Lu, S. Wang, Y. Sun and C. Yan, "Optimal scheduling of buildings with energy generation and thermal energy storage under dynamic electricity pricing using mixed-integer nonlinear programming," *Applied Energy,* vol. 147, pp. 49-58, 2015.

[48] J. Cai and J. E. Braun, "Laboratory-based assessment of HVAC equipment for power grid frequency regulation: Methods, regulation performance, economics, indoor comfort and energy efficiency," *Energy and Buildings,* vol. 185, pp. 148-161, 2019.

[49] J. Cai and J. E. Braun, "Assessments of variable-speed equipment for packaged rooftop units (RTUs) in the United States," *Energy and Buildings,* vol. 164, pp. 203-218, 2018.

[50] M. Deru, K. Field, D. Studer, K. Benne, B. Griffith, Torcellini, B. Liu, M. Halverson, D. Winiarski, M. Rosenberg, M. Yazdanian, J. Huang and D. Crawley, "U.S. Department of Energy Commercial Reference Building Models of the National Building Stock," National Renewable Energy Laboratory, Golden, 2011.

[51] [Online]. Available: https://fmi-standard.org/.

[52] B. Liu, B. A. Thornton, M. I. Rosenberg, E. E. Richman, W. Wang, Y. Xie, J. Zhang, H. Cho, V. V. Mendon and R. A. Athalye, "Achieving the 30% Goal: Energy and Cost Savings Analysis of ASHRAE Standard 90.1-2010," Pacific Northwest National Laboratory, Richland, 2011.

[53] A. Faghri and Y. Zhang, Transport Phenomena in Multiphase Systems, Amsterdam: Elsevier, 2006.

[54] T. L. Bergman, A. S. Lavine, F. P. Incropera and D. P. Dewitt, Fundamentals of Heat and Mass Transfer, 7th ed., Hoboken: Wiley, 2011.

[55] S. Churchill and H. Chu, "Correlating equations for laminar and turbulent free convection from a vertical plate," *International Journal of Heat and Mass Transfer,* vol. 18, no. 11, pp. 1323-1329, 1975.

[56] R. Birkebak and A. Abdulkadir, "Heat transfer by natural convection from the lower side of a finite horizontal heated surface," in *4th International Heat Transfer Conference*, Paris, 1970.

[57] J. R. Lloyd and W. R. Moran, "Natural convection adjacent to horizontal surface of various planforms," *Journal of Heat Transfer,* vol. 96, no. 4, pp. 443-447, 1974.

[58] PureTemp, "PureTemp 15 Technical Data Sheet," 2020. [Online]. Available: http://www.puretemp.com/stories/puretemp-15-tds. [Accessed 1 December 2020].

[59] The Mathworks Inc., "nlinfit," 2025. [Online]. Available: https://www.mathworks.com/help/stats/nlinfit.html.

[60] ASHRAE, "ANSI/ASHRAE Standard 55-2020, Thermal Environmental Conditions for Human Occupancy," American Society of Heating, Refrigerating, and Air-Conditioning Engineers, Inc., Peachtree Corners, 2021.

[61] ASHRAE, "ANSI/ASHRAE Standard 62.1-2019, Ventilation for Acceptable Indoor Air Quality," American Society of Heating, Refrigerating, and Air-Conditioning Engineers, Inc., Atlanta, 2019.

[62] Florida Power & Light Company, "Business rates and clauses," June 2020. [Online]. Available: https://www.fpl.com/content/dam/fpl/us/en/rates/pdf/Business%20(Effective%20June%202020).pdf. [Accessed 30 November 2020].

[63] Tucson Electric Power Company, "Medium General Service Time-of-Use," 1 January 2021. [Online]. Available: https://www.tep.com/wp-content/uploads/211-TGMGST.pdf. [Accessed 5 April 2021].

[64] El Paso Electric Company, "Schedule No. 24 General Service Rate," 18 July 2017. [Online]. Available: https://www.epelectric.com/files/html/Rates_and_Regulatory/13_-_Rate_24_General_Service_Rate.pdf. [Accessed 30 November 2020].

[65] Orange and Rockland Utilities Inc, "Time-of-Use Rates," 2020. [Online]. Available: https://www.oru.com/en/save-money/energy-saving-programs/time-of-use. [Accessed 30 November 2020].

[66] J. Kosny, N. Shukla and A. Fallahi, "Cost Analysis of Simple Phase Change Material-Enhanced Building Envelopes in Southern U.S. Climates," US Department of Energy, 2013.

[67] U.S. Department of Energy, "Prototype Building Models," [Online]. Available: https://www.energycodes.gov/prototype-building-models. [Accessed 14 February 2022].

[68] B. Shen and C. K. Rice, "DOE/ORNL Heat Pump Design Model," 30 September 2019. [Online]. Available: https://hpdmflex.ornl.gov/. [Accessed 14 February 2022].

[69] American Society of Heating, Refrigerating and Air-Conditioning Engineers, Inc., 2020 ASHRAE Handbook - HVAC Systems and Equipment (SI Edition), ASHRAE, 2020.

[70] J. Cai and J. Braun, "An inverse hygrothermal model for multi-zone buildings," *Journal of Building Performance Simulation,* vol. 9, no. 5, pp. 510-528, 2016.

[71] B. Shen, J. New and V. Baxter, "Air source integrated heat pump simulation model for EnergyPlus," *Energy and Buildings,* vol. 156, pp. 197-206, 2017.

[72] U.S. Department of Energy, EnergyPlus™ Version 9.4.0 Documentation - Engineering Reference, 2020.

[73] Georgia Power, "Nights & Weekends," 2022. [Online]. Available: https://www.georgiapower.com/residential/billing-and-rate-plans/pricing-and-rate-plans/nights-weekends.html. [Accessed 6 February 2022].

[74] G. Welch and G. Bishop, "An Introduction to the Kalman Filter," University of North Carolina at Chapel Hill, Chapel Hill, NC, 1995.

[75] Gurobi Optimization, LLC, Gurobi Optimizer Reference Manual, 2022.

[76] S. Diamond and S. Boyd, "CVXPY: A Python-Embedded Modeling Language for Convex Optimization," *Journal of Machine Learning Research,* vol. 17, no. 83, pp. 1-5, 2016.

[77] A. Agrawal, R. Verschueren, S. Diamond and S. Boyd, "A rewriting system for convex optimization problems," *Journal of Control and Decision,* vol. 5, no. 1, pp. 42-60, 2018.

[78] D. Pernsteiner, S. Alexander, L. Kasper, R. Hofmann and S. Jakubek, "State estimation concept for a nonlinear melting/solidification problem of a latent heat thermal energy storage," *Computers and Chemical Engineering,* vol. 153, p. 107444, 2021.

[79] P. Hlanze, Z. Jiang, J. Cai and B. Shen, "Model-based predictive control of multi-stage air-source heat pumps integrated with phase change material-embedded ceilings," *Applied Energy,* vol. 336, p. 120796, 2023.

[80] P. Hlanze, A. Elhefny, Z. Jiang, J. Cai and H. Shabgard, "In-duct phase change material-based energy storage to enhance building demand flexibility," *Applied Energy,* vol. 310, p. 118520, 2022.